Missouri S&T Library and Learning Resources

Scholars' Mine

Doctoral Dissertations | Student Theses and Dissertations

Summer 2021

GIS and remote sensing groundwater potentiality investigation of Gulu District, Uganda using synthetic aperture radar and magnetic geophysics

Rachel Ann Jones

Follow this and additional works at: https://scholarsmine.mst.edu/doctoral_dissertations

 Part of the Geological Engineering Commons, and the Remote Sensing Commons

Department: Geosciences and Geological and Petroleum Engineering

Recommended Citation

Jones, Rachel Ann, "GIS and remote sensing groundwater potentiality investigation of Gulu District, Uganda using synthetic aperture radar and magnetic geophysics" (2021). *Doctoral Dissertations*. 3005.
https://scholarsmine.mst.edu/doctoral_dissertations/3005

This thesis is brought to you by Scholars' Mine, a service of the Missouri S&T Library and Learning Resources. This work is protected by U. S. Copyright Law. Unauthorized use including reproduction for redistribution requires the permission of the copyright holder. For more information, please contact scholarsmine@mst.edu.

GIS AND REMOTE SENSING GROUNDWATER POTENTIALITY INVESTIGATION OF GULU DISTRICT, UGANDA USING SYNTHETIC APERTURE RADAR AND MAGNETIC GEOPHYSICS

by

RACHEL ANN JONES

A DISSERTATION

Presented to the Graduate Faculty of the

MISSOURI UNIVERSITY OF SCIENCE AND TECHNOLOGY

In Partial Fulfillment of the Requirements for the Degree

DOCTOR OF PHILOSOPHY

in

GEOLOGICAL ENGINEERING

2021

Approved by:
J. David Rogers, Advisor
Joel Burken
Ryan Smith
Anthony Nguy-Robertson
Jeremy Maurer

© 2021

Rachel Ann Jones

All Rights Reserved

PUBLICATION DISSERTATION OPTION

This dissertation consists of the following three articles, formatted in the style used by the Missouri University of Science and Technology:

Paper I: Pages 11-33 abstract has been submitted to *Geomatics* and the abstract has been published in the proceedings of United States Geospatial Intelligence Foundation (USGIF) GEOINTegration Summit, September 2019.

Paper II: Pages 34-67 is intended for submission in *Remote Sensing* and the abstract has been published in the proceedings of Intelligence Community Academic Research Symposium (ICARS), online, in September 2020.

Paper III: Pages 68-103 is intended for submission to the *Journal of Hydrology* and the abstract has been published in the proceedings of Intelligence Community Academic Research Symposium (ICARS), online, in September 2020.

ABSTRACT

Developing countries have few resources for ground-based hydrological investigations to determine optimal placement of boreholes for community water access. Remote sensing data are available at a variety of resolutions and sense different parameters, and are useful inputs for hydrologic models, but these data are rarely obtainable in developing countries with the parameters or resolutions necessary for hydrologic applications. This research seeks to use and improve existing remote sensing and GIS techniques to identify areas of optimal water supply in locations with limited geologic or hydrologic information, such as Gulu District, Uganda. Fusing different remotely sensed data sets can produce higher resolution data sets of some necessary parameters. This research focuses on fusing remotely sensed data sets to aid in the investigation of groundwater resources using a multicriteria decision method. This research was conducted in three phases. The first phase was a proof-of-concept study that fused Sentinel-1 synthetic aperture radar (SAR) data with unmanned aerial vehicle (UAV) acquired photogrammetry using Principal Component Analysis (PCA) to improve the accuracy and resolution of digital elevation models (DEMs) and enhance surface lineaments. This fusion technique was then applied in the second phase to Alos Palsar quad-pol SAR and magnetic data acquired in the Gulu District of Uganda. The final phase of research used the lineament map produced in the second phase as one of the datasets for a final groundwater potentiality model. The data for this particular model can be processed and a groundwater potentiality model developed in a short time span to benefit crisis and disaster affected communities in a more immediate manner.

ACKNOWLEDGMENTS

I would like to thank my committee and colleagues for their guidance throughout this research journey, including J. David Rogers, Joel Burken, Anthony Nguy-Robertson, Ryan Smith, Jeremy Maurer, and Katherine Grote who advised or mentored me in some way to accomplish this research. I am humbled and grateful to have the opportunity to collaborate with such honorable and accomplished colleagues.

I am thankful to Colonel Robert Kirsch (U.S. Army, retired) of the U.S. Army Training and Doctrine Command (TRADOC) Capability Manager (TCM) – Geospatial at Fort Leonard Wood whose mentorship and friendship was invaluable for the duration of this doctoral research.

Finally, I would like to thank Father Abbot Philip Anderson, Father Prior Francis Bethel, Mother Prioress Sister Annunciata, and the late Sister Catherine Coiner of Our Lady of the Annunciation at Clear Creek Abbey and Queen of Angels Priory for providing a home and being my family when there was none.

This research was supported in part by an appointment to the Department of Defense (DOD) Research Participation Program administered by the Oak Ridge Institute for Science and education (ORISE) through an interagency agreement between the U.S. Department of Energy (DOE) and the DOD. ORISE Is managed by ORAU under DOE contract number DE-SC0014664. All opinions expressed in this paper are the author's and do not necessarily reflect the policies and views of DOD, DOE, or ORAU/ORISE. Approved for public release, 21-060.

TABLE OF CONTENTS

Page

PUBLICATION DISSERTATION OPTION iii

ABSTRACT iv

ACKNOWLEDGMENTS v

LIST OF ILLUSTRATIONS x

LIST OF TABLES xii

SECTION

1. INTRODUCTION 1

1.1. BACKGROUND 1

1.2. MISSION OF THIS RESEARCH 3

1.3. PHASE I 5

1.3.1. Objective 5

1.3.2. Concept 5

1.3.3. Summary 6

1.4. PHASE II 7

1.4.1. Objective 7

1.4.2. Concept 7

1.4.3. Summary 8

1.5. PHASE III 9

1.5.1. Objective 9

1.5.2. Concept 9

1.5.3. Summary. 9

PAPER

I. DATA FUSION OF SYNTHETIC APERTURE RADAR (SAR) WITH UNMANNED AERIAL VEHICLE (UAV) PHOTOGRAMMETRY IN THE ARBUCKLE MOUNTAINS, OKLAHOMA USING IMAGE ENHANCEMENT FOR USE IN DIGITAL TERRAIN MODELS (DTMS) AND LINEAMENT ANALYSIS 11

ABSTRACT 11

1. INTRODUCTION 12

1.1. ELEVATION MODEL DEVELOPMENT 12

1.2. DATA FUSION 14

1.3. ENHANCED LINEAMENT DETECTION 16

2. METHODS 17

2.1. STUDY AREA 17

2.2. UAV PHOTOGRAMMETRY DATA ACQUISITION AND PROCESSING 17

2.3. RADAR PROCESSING 19

2.4. DATA FUSION 20

3. RESULTS AND DISCUSSION 21

3.1. DEVELOPMENT OF A DIGITAL TERRAIN MODEL 22

3.2. LINEAMENT DETECTION AND VALIDATION 25

3.3. SAR AND TOPOGRAPHY 26

4. CONCLUSION 28

REFERENCES 30

II. LINEAMENT EXTRACTION FROM SYNTHETIC APERTURE RADAR (SAR) AND MAGNETOMETRY FUSED DATA PRODUCTS FOR GROUNDWATER POTENTIALITY EXPLORATION: A CASE STUDY IN GULU DISTRICT, UGANDA 34

ABSTRACT....34

1. INTRODUCTION....35

2. MATERIALS AND METHODS....41

2.1. STUDY AREA....41

2.2. SAR DATA ACQUISITION AND PROCESSING....42

2.3. MAGNETOMETRY DATA ACQUISITION AND PROCESSING....46

2.4. DATA FUSION....47

3. THEORY....49

3.1. PAULI/RGB....49

3.2. VAN ZYL....50

3.3. CIRCULAR POLARIZATION....51

3.4. DATA FUSION WITH PRINCIPAL COMPONENT SHARPENING....52

3.5. LINEAMENT EXTRACTION....52

4. RESULTS AND DISCUSSION....53

5. CONCLUSIONS....58

REFERENCES....59

III. GROUNDWATER POTENTIALITY MODEL OF GULU DISTRICT, UGANDA USING GIS AND REMOTE SENSING WITH THE ANALYTICAL HIERARCHY PROCESS (AHP) METHOD....68

ABSTRACT....68

1. INTRODUCTION....69

2. MATERIALS AND METHODS....71

2.1. CHARACTERIZATION OF GULU DISTRICT, UGANDA....71

2.2 WORKFLOW FOR MAP DEVELOPMENT....73

2.3. THEMATIC INPUT LAYERS 74

2.4. ANALYTIC HIERARCHY PROCESS (AHP) 78

2.5. GROUNDWATER POTENTIALITY MAP 80

3. RESULTS AND DISCUSSION 82

3.1. CHARACTERIZATION OF THEMATIC INPUT LAYERS 82

3.2. GROUNDWATER POTENTIALITY MAP 84

3.3. VALIDATION 88

3.4. SENSITIVITY ANALYSIS 90

4. CONCLUSION 91

REFERENCES 95

SECTION

2. CONCLUSIONS AND RECOMMENDATIONS 104

2.1. CONCLUSIONS 104

2.2. RECOMMENDATIONS 105

APPENDICES

A. MATRIX DECOMPOSITIONS 107

B. SAR POLARIMETRIC DECOMPOSITIONS 111

C. LINEAMENT EXTRACTION RESULTS 119

D. VARIATIONS OF AHP MODEL 122

BIBLIOGRAPHY 127

VITA 136

LIST OF ILLUSTRATIONS

PAPER I Page

Figure 1. Arbuckle Mountains, Okalahoma aerial view.. 18

Figure 2. Results of UAV data photogrammetric processing over study area..... 19

Figure 3. Sentinel 1A SAR. 21

Figure 4. Comparison of TINs.. 24

Figure 5. Lineaments detection analysis. 27

Figure 6. Scatterplot of SRTM DEM and Sentinel-1 SAR amplitude..... 28

PAPER II

Figure 1. Workflow for radiometric processing of ALOS/PALSAR data..... 44

Figure 2. Alos Palsar decompositions; A: PauliRGB, B: Van Zyl; C: Circular... 45

Figure 3. Airborne magnetic data acquired over Gulu District, Uganda.. 48

Figure 4. SAR data fused with magnetic data using PC Sharpening..... 49

Figure 5. Van Zyl/First Vertical Derivative data fusion and lineament extraction.. 57

PAPER III

Figure 1. Area of interest. 71

Figure 2. Workflow for groundwater potentiality map development. 73

Figure 3. Thematic maps used for groundwater potentiality model.. 74

Figure 4. Lineament density maps used for variations of the Groundwater Potentiality Model.. 78

Figure 5. Groundwater potentiality map of Gulu District, Uganda with validation locations. 84

Figure 6. Groundwater potentiality maps varied according to lineament density maps.....85

Figure 7. Groundwater potentiality maps varied varied according to variations of the top four weighted AHP factors.. 91

LIST OF TABLES

PAPER I Page

Table 1. Statistics of the elevations of the LiDAR-derived DEM, original orthomosaic, SAR, and fused orthomosaic..... 24

Table 2. Input parameters and values for lineament detection. 26

PAPER II

Table 1. Data characteristics of ALOS/PALSAR SAR data acquired over Gulu District, Uganda. 43

Table 2. Lineament extraction inputs for SAR and magnetic datasets. 55

Table 3. Lineament extraction inputs for fused datasets..... 55

Table 4. Lineament orientations, confidence interval, and range of orientations for all datasets..... 56

PAPER III

Table 1. Analytic Hierarchy Process (AHP) pairwise comparison..... 79

Table 2. AHP final weights calculated from the pairwise comparison..... 80

Table 3. AHP final weights by percentage and effectiveness..... 81

Table 4. AHP factors listed by percent area of interest and total area in kilometers..... 83

Table 5. Percent and area of groundwater potentiality ratings according to lineament data product..... 87

1. INTRODUCTION

1.1. BACKGROUND

Uganda's civil war originated in northern Uganda where the infamous Lord's Resistance Army (LRA) recruited, oppressed, and enslaved many tribes, including the Acholi people in Amuria district where the research Area of Interest (AOI) is located. The conflict resulted in two million Internally Displaced People (IDPs), according to the United Nations High Commission for Refugees (UNHCR), food and water shortages, epidemics, and numerous human rights abuses including child soldiers, human trafficking, female genital mutilation (FGM), and mass rape as weapons of war and a means of genocide.

Hostilities ceased in 2006 with the advent of a peace agreement and the LRA migrated north to South Sudan and northwest to the Democratic Republic of Congo (DRC) and the Central African Republic (CAR). In the years following the conflict, various governmental and international non-governmental organizations (iNGOs) participated in humanitarian efforts within the region. UNHCR shifted responsibility for IDP humanitarian/relief and recovery/development efforts to the Uganda Human Rights Commission (UHRC) in 2012 when 247 IDP camps were closed.

As Uganda has progressed in recovery efforts another tragedy appeared on the horizon. In 2011, Uganda's northern neighbor Sudan split after years of conflict and fell into civil war. South Sudan's civil war enjoyed a brief period of peace until hostilities erupted again in December of 2013 when President Salva Kiir's military encountered numerous rebel conflicts and widespread, compulsory missionary evacuations. As a result, South Sudan, the world's youngest nation, has fed a steady supply of refugees to Uganda's

northern border. According to UNHCR, there have been over one million South Sudanese refugees that have flooded the northern border of Uganda alone, not including those that have crossed the border to Kenya and DRC. The influx of refugees has been so devastating to an already impoverished nation that the World Bank's Regional Operation on Development Response to Displacement Impacts Project in the Horn of Africa (DRDIP) has dedicated US$175 million for humanitarian and relief efforts. In light of the emerging crisis, UNHCR has expressed critical concern for food security and water, sanitation and hygiene (WaSH) efforts.

In addition to the South Sudanese civil war, Uganda has experienced the immigration of refugees from the Democratic Republic of Congo (DRC) along its western border. DRC refugees flee civil war, periodic Ebola epidemics, eruptions from the Nyiragongo and Nyamuragira volcanoes, and local militant groups associated with the historical migration of armed groups from neighboring Rwanda and Burundi.

Following the United Nation's Millenium Development Goals (MDGs) set forth in 2000 and ending in 2015, the United Nations published 17 Sustainable Development Goals (SDGs) to "balance the three dimensions of sustainable development: the economic, social and environmental" and to bridge the gap between the end of the MDG initiative and the beginning of SDG activities. Sustainable Development Goal #6 is: "Ensure availability and sustainable management of water and sanitation for all."

Governmental organizations, iNGOs, and research scientists are tasked with the seemingly insurmountable burden of reconciling post-civil war recovery efforts with the current refugee humanitarian crisis and the UN SDGs to be achieved by 2030. The World Health Organization (WHO), the World Bank, the African Development Bank, UNHCR,

and UNICEF have identified WaSH projects as foundational to humanitarian and societal prosperity efforts. As noted by the British Geological Survey (BGS), sub-Saharan Africa (SSA) faces a dire need for sustainable water resources and cost-effective borehole drilling programs. The BGS outlined groundwater resource exploration methods in SSA as a function of hydrogeological domains and correlated the results with the cost of development. Remote sensing methods were identified as the most cost-effective survey method.

1.2. MISSION OF THIS RESEARCH

This research investigates groundwater resources in north central Uganda using remote sensing methods. Magnetometry and various polarizations of satellite-borne Alos Palsar L-Band SAR data has been fused to determine surface expressions of shallow subsurface fracture network geometry, specifically horst and graben structures, for the identification of borehole drilling locations. Terrestrial geomorphologic features, such as fracture networks and paleochannels, have previously been identified using SAR data products. This research supplements previously confirmed, low resolution SAR methods compared with higher resolution magnetometry for the goal of extrapolating local fracture geometry to regional fracture geometry using feature extraction methods.

An initial literature review of current technologies has been conducted to ensure that prevailing methodologies are incorporated into this research structure while minimizing the risk of theoretical claims that may prove to be futile for the ultimate goal of sustainable groundwater resource exploitation. Hypothetical mathematical models that are unproven in field experiments have been excluded from the investigation because

regional borehole drilling programs require the consideration of a wide range of variables that are not solely dependent on the geological circumstances.

The Uganda Ministry of Water and Environment has documented the locations and functionalities of existing water points throughout the country. A successful borehole drilling program must be developed with consideration of the location of former IDP camps and settlements, the distance to a potable water source, potential for E Coli contamination, as well as vandalism by local combatants and cattle raiders (Karamojong). There is no comprehensive and dependable hydrogeological database for Uganda, therefore borehole placement must be based on the highest likelihood of aquifer penetration as well as the results of terrain analysis using remote sensing methods to designate optimal geologic provinces for drilling.

Subsequent to identification of fracture geometry within the AOI, a model has been derived to correlate optimal borehole geologic provinces with thematic maps to characterize responsible placement of future water point access. Temporal dynamics of human migration will be excluded to identify a generalizable method of borehole placement, however the model will be adaptable to future migration activity using verifiable methods, such as situation reports (SitReps), monitoring and evaluation reports as well as rapid assessments which are conducted by in-country humanitarian organizations during times of crisis.

1.3. PHASE I

The first phase of this research demonstrates the effectiveness of data fusion to facilitate more accurate elevation models and establish that it is beneficial for using machine learning algorithms in lineament extraction.

1.3.1. Objective. The primary objective of Phase I was to demonstrate the effectiveness of pixel level data fusion methods to enhance elevation profiles of surface lineaments. This objective was accomplished with a proof-of-concept study fusing Sentinel-1 SAR and unmanned aerial vehicle (UAV) photogrammetry of the Arbuckle Mountains. The data fusion product provides more accurate detection of topographic features than either of these data sets by themselves and enables a more thorough surface lineament analysis.

1.3.2. Concept. Data fusion is a remote sensing industry standard technique that combines data from varying spectral and spatial resolution data products to achieve higher resolution and combine the desired characteristics of each data product (Ghassemian, 2016). Commonly fused data products are satellite-borne optical and SAR products. Recent techniques in fusing PSInSAR data and LiDAR data have been developed (Ciampalini, et al., 2016) to conduct high resolution statistical analysis of landslide deformation that would not be possible without the LiDAR-derived DEM. This technique extends the same general methodology to photogrammetric products, which has not yet been accomplished. The benefit of using photogrammetry for analysis is two-fold. First, photogrammetric equipment is substantially less expensive and more readily available than satellite-based data. Second, photogrammetry is a passive means of remote sensing, as opposed to LiDAR which is active. Passive remote sensing is often a more attractive

solution within international contexts because no signal can be sensed by adversaries and, thus, allows for undetected acquisition of data.

1.3.3. Summary. Accurate elevation models are essential for a wide variety of applications in engineering and science. In developed countries, accurate elevation profiles developed from LIDAR or SRTM DEMs data are available in most locations. However, in developing countries, accurate, high spatial resolution elevation measurements are often not available. This study investigates the use of Synthetic Aperture Radar (SAR) data combined with low-cost photogrammetry to more accurately define elevation measurements in locations where there is a paucity of data. In this study, high resolution UAV acquired photogrammetry was fused with lower resolution Sentinel-1 SAR data. The resulting fused data product can be used to develop more accurate elevation measurements than can be generated using only SAR data and, thus, a more practical digital terrain model (DTM). Additionally, elevations developed from the fused data product have less error due to vegetation than models developed solely from photogrammetry. The accuracy of a triangulated irregular network (TIN) created with the fused data set was evaluated by comparison with a TIN developed from LIDAR data, and the fused data set generated more accurate elevations than did the non-fused data. A secondary benefit of fusing these data sets is lineament identification; comparison of fused and non-fused images showed that some lineaments are more easily detected in the fused images.

1.4. PHASE II

The goal of Phase II was to establish that lineament extraction from the data fusion of SAR and magnetic geophysics can identify surface and subsurface lineations to assist in identifying hydrologic features.

1.4.1. Objective. The Phase II objective endeavors to use the data fusion process from Phase I to fuse airborne magnetometry with SAR data to improve fracture characterization in Gulu District. Surface expressions of lineaments are detected with SAR and subsurface lineaments are detected with magnetometry. The integration of these datasets creates a data product with a more complete visualization of fracture networks for subsequent lineament extraction using supervised classification.

1.4.2. Concept. Igneous and metamorphic rock are often difficult environments to develop for water supply. In these rock types, groundwater yield will largely depend on drilling into a set of interconnected fractures, and groundwater recharge must also predominantly occur through these fractures. These fractures are seldom visible at the land surface but can sometimes be detected using remotely sensed or geophysical data. In Uganda, some fractures and paleodrainage channels have been observed in Alos Palsar satellite data. These are L-band radar data which penetrates an undetermined distance below the surface because soil moisture influences the depth of penetration and backscatter characteristics of the radar product. Additionally, airborne magnetometry data have been acquired over the Gulu District of Uganda which has revealed the locations of fracture sets that have accumulated iron from precipitation out of groundwater.

In this phase of research, satellite-based Alos Palsar L-Band SAR data has been fused with airborne magnetic data to improve fracture characterization. The efficacy of

the fused data product for detecting fractures has been evaluated by comparing all of the resulting images with fractures mapped during previous field and aerial research of the Aswa Shear Zone (Katumwehe et al., 2016).

Currently, geophysical data must be analyzed side-by-side with remotely sensed data. Fusion of the data reveals fracture patterns that cannot easily be determined from separate data products. Thus, this method develops a more efficient process for lineament detection while producing a dataset that can be used for a more complete hydrological analysis.

1.4.3. Summary. Lineament extraction of fault networks from remotely sensed data products is common practice in GIS and RS applications and is used in the characterization of hydrogeological regimes. Fractures are conduits for fluid flow and an important source of aquifer recharge. Existing techniques utilize single data products which may not always present a definitive classification of fractures, folds, or faults in areas where the terrain obscures lineaments expressions. SAR is commonly used for the development of lineament maps; however curvilinear surface hydrologic features are often detected simultaneously with fracture networks. Surface drainage patterns must be isolated from fracture networks to characterize surface recharge regimes more accurately. Magnetic geophysical data is commonly used to map fracture networks as well but does not detect all the lineaments within a fracture network. This research fuses various Alos Palsar L-Band polarimetric matrix decompositions (Appendix A) with various magnetic geophysical products to generate a lineament map that maximizes the number of lineaments detected while excluding hydrologic stream systems from the end product. PauliRGB, Van Zyl, and circular SAR products (Appendix B) are used in combination with

the magnetic analytic signal, horizontal gradient, and first vertical derivative to evaluate the most effective combination of data fusion products for lineament detection.

1.5. PHASE III

The last phase of this research used the previous lineament extraction as a parameter in the groundwater potentiality model.

1.5.1. Objective. A groundwater potentiality model has been developed using fused data and land use features. The intended goal of the model is to integrate surface topography, land use characteristics, and fracture density into a multicriteria decision-based matrix. The resultant model is a groundwater potentiality map that delineates groundwater provinces based on probability of groundwater recharge.

1.5.2. Concept. Groundwater resources in Uganda are largely unmapped, and consequently there is little information to guide drilling of community water supply wells. To better identify areas of potential groundwater supply, the groundwater recharge potential can be estimated using parameters from thematic maps. In Uganda, some of these parameters, such as land use/land cover, watershed delineation, slope, precipitation, drainage density, and potential for runoff can be estimated from remote sensing data. The lineament map developed in Phase II has been used as a parameter in the groundwater potentiality model to complete variables necessary for the decision matrix. The final groundwater potentiality map is an advancement for groundwater resource exploration in Gulu District as well as other developing communities.

1.5.3. Summary. GIS and remote sensing have been increasingly used to model groundwater potentiality in developing countries due to scarcity of ground-based data.

Gulu District, Uganda has few technological resources to acquire ground-based data, thus GIS and remote sensing are necessary to develop models for the location of groundwater resources. An analytical hierarchy process (AHP) has been applied to various GIS derived and remotely sensed datasets to investigate optimal borehole drilling locations. Precipitation, soils, lithology, drainage and lineament densities, land cover, and slope of the 3,900 km2 area of interest (AOI) were weighted according to the AHP method and processed with a weighted hydrologic model algorithm.

PAPER

I. DATA FUSION OF SYNTHETIC APERTURE RADAR (SAR) WITH UNMANNED AERIAL VEHICLE (UAV) PHOTOGRAMMETRY IN THE ARBUCKLE MOUNTAINS, OKLAHOMA USING IMAGE ENHANCEMENT FOR USE IN DIGITAL TERRAIN MODELS (DTMS) AND LINEAMENT ANALYSIS

Rachel Jones

Department of Geological Engineering, Missouri University of Science and Technology, Rolla, MO 65409

ABSTRACT

Accurate elevation models are essential for a wide variety of applications in engineering and science. In developed countries, accurate elevation profiles developed from LIDAR or SRTM DEMs data are available in most locations. However, in developing countries, accurate, high spatial resolution elevation measurements are often not available. This study investigates the use of Synthetic Aperture Radar (SAR) data combined with low-cost photogrammetry to more accurately define elevation measurements in locations where there is a paucity of data. In this study, high resolution Unmanned Aerial Vehicle (UAV) acquired photogrammetry data were fused with lower resolution Sentinel-1 SAR data. The resulting fused data product can be used to develop more accurate elevation measurements than can be generated using only SAR data and with less vegetation-induced error than in models developed solely from photogrammetry. This fused data product can be used to create a more useful digital terrain model (DTM).

This technique was evaluated by comparing the accuracy of a triangulated irregular network (TIN) generated with the fused data product to a TIN developed from LIDAR data, and the fused data set generated more accurate elevations than did the non-fused data. A secondary benefit of fusing these data sets is improved automated detection of lineaments. A comparison of automated lineament detection results using fused and non-fused images showed that fused images reduce the very large number of "false positives" caused by vegetation, thus making automated detection much more useful for geologic site characterization.

1. INTRODUCTION

1.1. ELEVATION MODEL DEVELOPMENT

Elevation data are necessary for topographic analyses, monitoring land surface changes, and analysis of geologic structures. Elevation models are generated using a variety of remotely sensed data products, including satellite- and aircraft-acquired data sets. Elevation models are most widely generated using data from Shuttle Radar Topography Mission (SRTM) satellite-borne datasets. SRTM digital elevation models (DEMs) are produced using at least two radar datasets from different angles to accurately calculate the geodetic surface. SRTM data are used to process synthetic aperture radar (SAR) data to generate single radar images that are geodetically accurate (Zhu et al., 2016).

SAR signals are acquired in different polarities and penetrate obstacles such as clouds and vegetation to image the bare earth surface (Walker, 2013). SAR data products are radiometrically terrain corrected (RTC), which embeds SRTM DEMs into the final

product, thus producing a geocoded image for high precision thematic maps (Galloway and Hoffmann, 2007; Zhang et al., 2018). SAR data are acquired over much of the earth, so are available in both developed and developing countries (Abdelkareem et al., 2012; Laurencelle et al., 2015).

Elevation models that have both high accuracy and high spatial resolution can be generated with Light detection and ranging (LiDAR) data. LiDAR are typically collected from an aircraft, where laser signals are transmitted to the surface, reflected, and then recorded at the aircraft. Although most LiDAR data are collected from manned aircraft, this method is becoming more commonly used on unmanned aerial vehicles (UAVs) (Luo et al., 2020). One important benefit of LiDAR data is that LiDAR-derived DEMs have higher spatial resolution than SAR data (Glenn et al., 2006).

If photogrammetry data acquired with UAVs are used to generate DEMs, one possible product is a digital surface model (DSM). DSMs include natural and built features (i.e., trees, powerlines, etc.) in the DEM and are most commonly generated using LiDAR data. Other useful DEMs are digital terrain models (DTMs), which show only the bare earth surface (omitting natural and built features) for a precise topographic surface. Photogrammetry data include reflections from vegetation, and thus are not as useful for independently developing DTMs, as the vegetation introduces error into estimates of the topographic elevation (Strozzi et al., 2010). However, photogrammetry data are relatively inexpensive and can be acquired with very high resolution (Xu et al., 2019). Thus, photogrammetry data are used extensively in earth science and engineering studies, especially in areas with dense cloud cover where optical satellite-borne imagery may be insufficient (Amro et al., 2011).

Both DTMs and DSMs can be used to visualize changes in elevation. Triangular irregular networks (TINs) are one technique for displaying elevation data. TINs are developed by constructing the edges and vertices of elevation points into triangles to develop a three-dimensional representation of a geomorphological surface. Precision of the geodetic surface is retained in TINs while interpolating between elevation points to highlight linear features such as ridgelines and stream channels and can be useful for identification of geologic structures.

1.2. DATA FUSION

This study investigates the potential of fused satellite-based SAR data and UAV-based photogrammetry data to increase the accuracy of elevation profiles by generating digital terrain models (DTMs) and to help identify surface lineaments. Data fusion combines data products with varying spectral and spatial resolutions to achieve higher accuracy products and combine the desired characteristics of each data product (Devi and Devanathan, 2019; Ghassemian, 2016). Commonly fused data products are satellite-borne optical and SAR products (Mahyoub et al., 2019). Multi-source data fusion techniques are an active area of research and include optical, radar, and various geophysical datasets (Pan et al., 2020).

Fusion of both remotely sensed data sets from satellites and aircraft have been used for a variety of applications and have become ubiquitous within the remote sensing industry (Vijayaraj et al., 2006). Elevation models derived from photogrammetry data have been used in combination with SAR data to analyze ground deformation of the Lascar volcano in Chile (Pavez et al., 2006). Other elevation models developed by fusing PSInSAR data

and LiDAR data have been used to conduct high resolution statistical analysis of landslide deformation (Ciampalini et al., 2016). High precision geologic maps of the Gascoyne Province, Western Australia have been produced using fused airborne gravity and magnetic data (Olierook et al., 2019). Another application of data fusion was employed using SAR, Landsat (ETM+) images, and elevation models to produce terrain and surficial geology maps of the Mackenzie Valley Pipeline Corridor, Canada (Pavlic et al., 2008). More recently, spatial-temporal fusion methods have been implemented using MODIS data and Landsat data using convolutional neural networks for target recognition and image classification (Wang and Wang, 2020).

Fusion of various data products has been well demonstrated in the literature, but the fusion of UAV photogrammetry with SAR is not a typical practice. This investigation generated a DTM of the land surface using SAR and a photogrammetric orthomosaic to improve the accuracy of elevation measurements using only the SAR data. This procedure is primarily useful in developing countries where high accuracy LIDAR data are not available. The fused data set may also be useful for lineament analysis (Luo et al., 2020). Lineament analysis is typically performed with individual datasets (Oyawale et al., 2020), but augmentation of existing lower spatial resolution DEMs with higher resolution photogrammetric data is beneficial in lineament analysis through DTM generation. UAV photogrammetry is becoming common in developing nations where access to technology is scarce (Milas et al., 2019), so the fusion of SAR and UAV photogrammetry may assist with both elevation estimation and lineament detection in these areas (Farahbakhsh et al., 2020).

One type of data fusion method is pixel-based analysis, which can be accomplished using pansharpening algorithms such as Brovey Transform, Gram-Schmidt, and Principal Component Analysis (PCA). These three techniques are considered component substitution methods which use a multispectral image projected onto a panchromatic image. PCA is the technique used for data fusion in this project. PCA is an unsupervised means of dataset classification to reduce a large number of variables to a simpler dataset while retaining the correlation between variables. Transforming multivariate data of correlated variables into a reduced subset of uncorrelated variables, the redundant information is removed from a dataset (Shahdoosti and Ghassemian, 2016). Since the PC fusion method uses eigenvalues and eigenvectors to calculate covariance matrices (Amro et al., 2011), the method is ideal to extract elevation data from SAR data and fuse the transformed topographic data into a smaller dataset.

1.3. ENHANCED LINEAMENT DETECTION

A secondary goal of the fusion of photogrammetry and SAR data in this project was to determine if surface lineaments were more detectable on the fused data product than on the non-fused images. Various data products have been effectively used for lineament detection including optical (Thannoun, 2013), SAR (Gaber et al., 2011), LiDAR (Yeomans et al., 2019), DEMs (Rahnama and Gloaguen, 2014), and airborne magnetic data (Alexandr, 2017; Gomes et al., 2014; Tagnon, 2016). UAV acquired photogrammetric data are capable of providing high resolution topographic data for surficial lineament analysis (Vasuki et al., 2014) where manual lineament detection can be performed efficiently (Yeomans et al., 2019; Oyawale et al., 2020). However, although manual methods of

lineament detection work well in smaller datasets, automated detection techniques are needed for large data sets. Data fusion can increase the likelihood of accurate lineament detection of larger datasets through image analysis techniques (Chabot et al., 2018).

2. METHODS

The methods for this research were developed to establish field techniques and a data fusion workflow for future lineament extraction of various datasets.

2.1. STUDY AREA

Data for this study were acquired at the Turner Falls Overlook, located within the Timbered Hills Group formation of the Arbuckle Mountains and along the southern border of Oklahoma. The Arbuckle Mountains are highly faulted and folded Precambrian and Cambrian basement rocks from the Ouachita Orogeny and include synclines, anticlines, thrust and fold faults, and various Ordovician and Cambrian outcrops (Figure 1). The Turner Falls Overlook is a 10 acre region, and it was chosen because the Cambrian exposures include moderately visible surface lineaments, and lineament detection was one of the objectives of this study. The site was also easily accessible to UAV flight missions and had high resolution LiDAR data for comparison of elevations.

2.2. UAV PHOTOGRAMMETRY DATA ACQUISITION AND PROCESSING

The UAV used to acquire data was a DJI Phantom 3 Professional. The mission was flown on August 10, 2018 using a double grid of 171 ft x 157 ft with 80% overlap of the images. The mission was flown at an altitude above ground of 15 m, and 225 images were

acquired (Table 1). The camera model onboard the UAV was an FC300X manufactured by DJI. The resolution of the images generated with this camera was 12.4 megapixel per image. The photogrammetry data was processed into an orthomosaic (Figure 2) using the Icaros OneButton photogrammetry software, a proprietary software package that performs all aspects of the orthomosaic construction process. The UAV-acquired orthomosaic was later fused with Sentinel-1 SAR data as a means of interpolating elevation data within the pixels of the SAR product and the orthomosaic and to determine whether lineament detection was improved by data fusion. In addition, a digital surface model (DSM) was developed from the data fusion and a subsequent triangular irregular network (TIN) was constructed to visualize the bare earth surface and validate the results of the final lineament extraction.

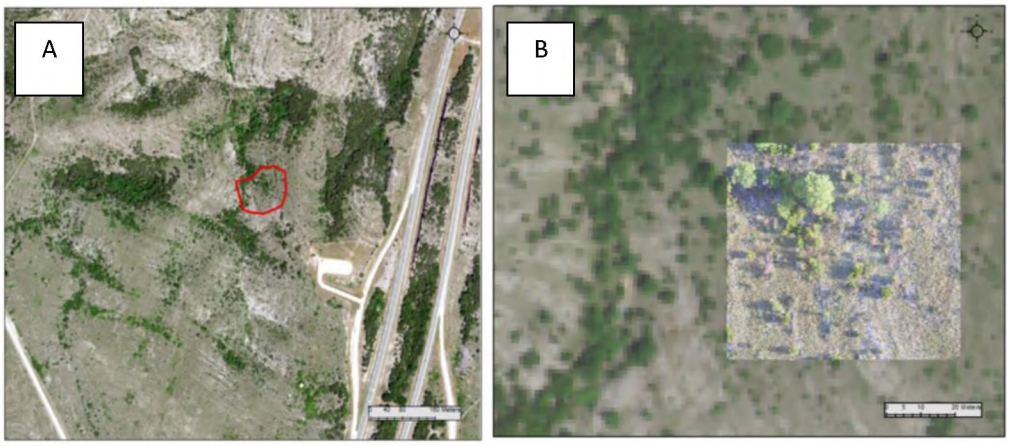

Figure 1. Arbuckle Mountains, Okalahoma aerial view. A) Regional location of UAV acquired photogrammetry at the Turner Falls Overlook. B) Photogrammetry of Turner Falls Overlook.

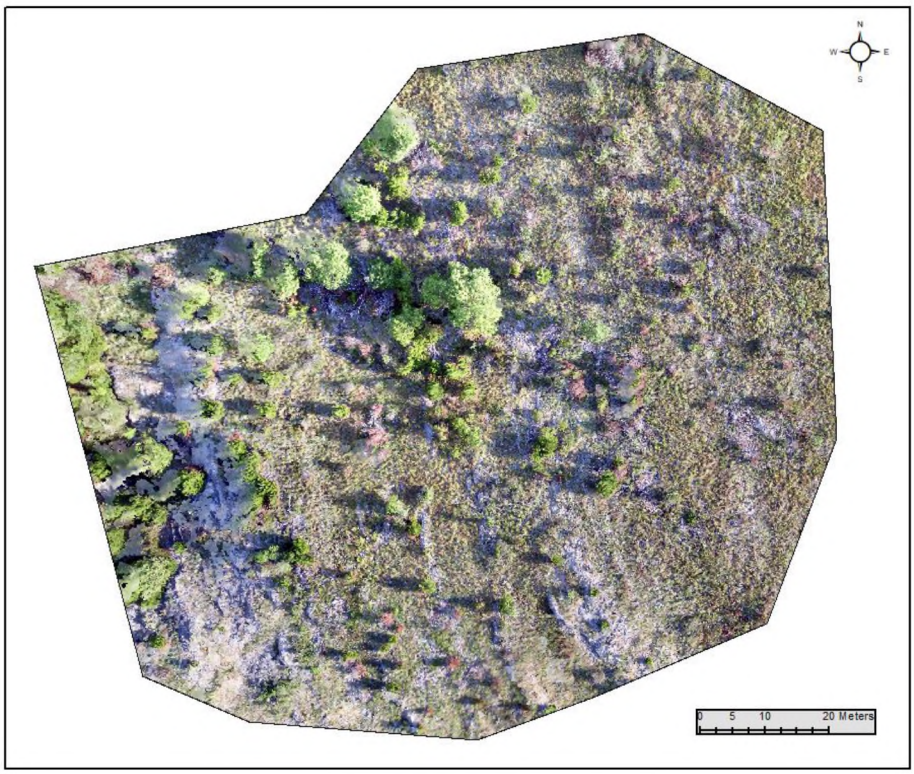

Figure 2. Results of UAV data photogrammetric processing over study area.

2.3. RADAR PROCESSING

The Sentinel family of satellites were launched by the European Space Agency (ESA). The Alaska Satellite Facility (ASF) archives a complete library of processed Sentinel-1 data. Sentinel-1 has a near-polar, sun synchronous orbit with a 12 day repeat cycle. The data used for this study were collected from the Sentinel 1A satellite in Interferometric Wide Swath (IW) mode on 9/29/2018 on the ascending orbit which correlates to an incidence angle of 45.3°. The default mode consists of a 250 km swath width with 5m x 20m ground resolution and 16 bits per pixel.

The Sentinel-1 data products are processed and available in three levels. The data product used for this study was processed by ESA to the Level 1 standard which is Ground

Range Detected (GRD) and geo-referenced. SAR data requires further on-site processing for calibration and despeckling (Kupidura, 2016). On-site processing was done using ENVI 5.5 algorithms. Specifically, an orbit file was applied to the data product for precise coordinate system transformation of orbit state vectors (Xu and Xu, 2016). The orbit file transforms the satellite-borne data through seven coordinate systems through the satellite's position to an earth-fixed geodetic reference frame (Noureldin et al., 2013).

The data were radiometrically calibrated using both the vertical and horizontal polarities of radar data. Next, the radiometric terrain flattening algorithm was applied to match the digital elevation model (DEM) for the geolocation of the corrected scene (Small, 2011). The DEM data product was acquired by the SRTM, and the DEM resampling method used for terrain flattening was bicubic interpolation. The results of the radiometric terrain flattening algorithm was then applied to the radar file using a Range Doppler Terrain Correction algorithm with a resampling method of bilinear interpolation. Finally, the Frost Correction algorithm for despeckling of radar data noise was applied to the vertical-vertical (VV) and vertical-horizontal (VH) polarities to reduce backscatter noise while preserving feature edges and lineations (Frost et al., 1982). The processed SAR images for the study area are shown in Figure 3.

2.4. DATA FUSION

Fusion of the SAR and photogrammetry data was accomplished by performing an image-to-image co-registration of the data products by selecting ground control points (GCPs) in the orthomosaic and in the SAR product. A total of 7 GCPs were distributed throughout the study area. The images were then warped and the resultant fused

orthomosaic was produced using PCA sharpening methods. In the acquired data, PCA fusion was used to allow for pixel level feature extraction from the fused dataset (Belfiore et al., 2016).

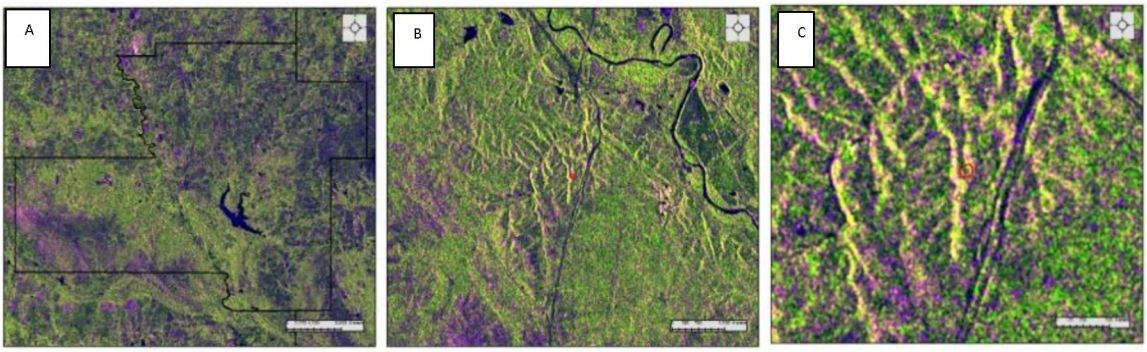

Figure 3. Sentinel 1A SAR. A) Murray County, Oklahoma. B) Central Murray County, Oklahoma. C) Turner Falls Overlook.

3. RESULTS AND DISCUSSION

The UAV-acquired orthomosaic as fused with Sentinel-1 SAR data as a means of interpolating elevation data within the pixels of the SAR product and the orthomosaic and to determine whether lineament detection was improved by data fusion. The resultant data fusion has retained topographic elevation data from the original orthomosaic while reducing the vegetative characteristics such as trees and larger bushes. In the fused image, low-lying vegetation was retained while larger bushes and trees were averaged out. It must be noted that while PCA fusion of SAR and photogrammetry is useful for spatial resolution enhancement (Shahdoosti and Ghassemian, 2016), spectral information is not preserved in the enhanced product (Vijayaraj et al., 2006). This is common in PCA fusion where

geometric complexity and edge enhancement are the desired characteristics in the final product (Thannoun, 2013).

3.1. DEVELOPMENT OF A DIGITAL TERRAIN MODEL

Geodetics employs DEMs, DSMs, DTMs, and triangular irregular networks (TINs) for various geospatial applications. DEMs of the bare earth surface are generated so that both natural and built features are absent from the data product for a precise topographic surface. Each pixel of a DEM corresponds to an elevation and is always associated with a geographical coordinate system. DSMs include natural and built features (i.e., trees, powerlines, etc.) and are commonly generated by LiDAR and UAV systems. DSMs are widely employed in construction, mining, and natural disasters for change detection. DTMs augment DEMs by including vector features such as mountain ridges and rivers by describing the land surface as a collection of three-dimensional data points. TINs are developed by constructing the edges and vertices of elevation points into triangles to develop a three-dimensional representation of a geomorphological surface. Precision of the geodetic surface is retained in TINs while interpolating between elevation points to highlight linear features such as ridgelines and stream channels and can be more useful for identification of geologic structures.

TINs were developed for using elevation data from only the SAR data (Figure 4A), from aircraft-borne LiDAR data (Figure 4B), from photogrammetry data (Figure 4C), and from fused SAR and photogrammetry data (Figure 4D). A comparison of the images in Figures 4A, 4B, 4C, and 4D shows that the same general patterns are shared by all images, but differences in precision and accuracy are apparent. The SAR-derived elevations have

high accuracy but very low precision, thus many of the smaller-scale topographic variations are absent. Figure 4B illustrates the LiDAR-derived elevations of the study area, which have high accuracy and much better precision than Figure 4A. The elevations derived from the original orthomosaic (non-fused photogrammetry) have much higher precision than data sets produced from SAR or LiDAR, but reduced accuracy in some areas (Figure 4C). For example, large trees appear as topographic highs on this image, resulting in erroneous elevation estimates. Finally, the SAR/orthomosaic fusion elevation data (Figure 4D) have higher precision than either Figure 4A or 4B and are more accurate than Figure 4C since the influence of vegetation has been reduced or removed.

To quantify the improvement in elevation estimation obtained through data fusion, the basic statistical parameters for the data sets shown in Figure 4 were calculated (Table 1). For comparison purposes, the LiDAR data were considered the most accurate and precise and were used as the "true" elevation. The root mean squared errors (RMSE) between the elevations derived from LIDAR data and from the other data sets are also shown in this table. Errors in data sets with greatly differing number of measurements were calculated by downscaling the data set with higher resolution to the same resolution as the coarser data set. An analysis of the mean elevation of each data set shows that each data type is fairly accurate (has approximately the same mean) when only an average elevation is needed. However, if enhanced precision is necessary, the RMSE values confirm what Figure 4 suggests visually: the fused orthomosaic is more similar to the LIDAR data than the original orthomosaic but has higher precision than the SAR data. The standard deviation measurements can sometimes be used as an indication of precision, but

the great differences in the number of measurements for different data sets makes comparisons difficult for this site.

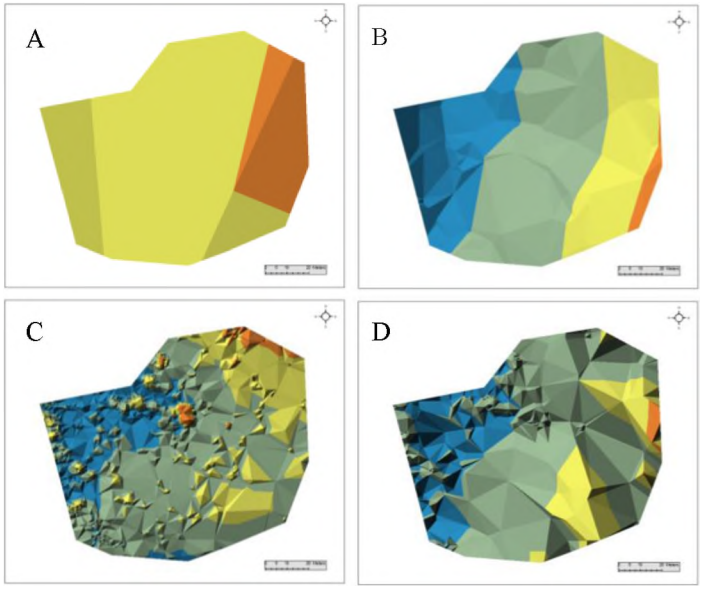

Figure 4. Comparison of TINs. A) Sentinel 1A SAR derived TIN. B) Oklahoma Geological Survey (OGS) 2 meter bare earth LiDAR derived TIN. C) Original photogrammetric orthomosaic TIN. D) Fused SAR and orthomosaic TIN.

Table 1. Statistics of the elevations of the LiDAR-derived DEM, original orthomosaic, SAR, and fused orthomosaic.

Elevations				
	LiDAR	Original Orthomosaic	SAR	Fused Orthomosaic
Mean, m	301	297	304	298
Standard Deviation	11.9	2	8	11.4
Number of Measurements	3,120	5,630,947	42	6,880
RMSE	N/A	10.4	2.02	2.3

3.2. LINEAMENT DETECTION AND VALIDATION

Enhanced lineament detection was one objective in this research. Figures 5A and 5B show the original and fused orthomosaics, respectively. Lineaments are visually detectable in both of these images. While visual identification of lineaments is important, large data sets require an automated lineament detection algorithm. To test automated linear detection, Geomatica image analysis and lineament detection software was applied to both the original and fused orthomosaics (Figures 5C and 5D, respectively). Input parameters and values used for the lineament detection algorithm were uniform between images (Table 2). In the original orthomosaic, 2,278 "lineaments" were detected. These lineaments have little structure and appear to be largely correlated to vegetation. In the fused orthomosaic, 101 lineaments were automatically detected, and the lineaments appear to be more correlated to topographic features or drainage channels. Thus, the fused orthomosaic appears to be of greater use in correlating automatically detected lineaments with geologic or topographic features. Although the fused orthomosaic appears to be better suited to automated image analysis than the original image, it should be noted that not all of the automatically detected lineaments in the fused image are easily correlated to topographic/drainage features. Thus, human review of algorithm results will probably be needed regardless of algorithm sophistication.

Manual detection of lineaments was also investigated using a subset of the study area. The subset area is shown as a rectangle in Figures 5A and 5A. Figures 5E and 5F show the manually detected lineaments for the original and fused orthomosaics, respectively. These Figures show that the fused data product seems to increase the visibility of lineaments for many features, as designated by the red ovals. The improved

visibility of these lineaments may due to the reduced effect of vegetation (due to fusion with SAR data) that may obscure the lineaments in the non-fused photogrammetric data. Although some lineaments are more visible in the fused data product, it should be noted that in other cases the lineaments are equally visible in both data sets (designated by yellow ovals in Figures 5E and 5F) or are less visible in the fused orthomosaic (designated by blue ovals). Thus, for manual detection of lineaments, the best detection strategy may be to analyze both fused and non-fused images.

Table 2. Input parameters and values for lineament detection.

Input	Value
Filter Radius (Pixels)	100
Edge Gradient Threshold	50
Curve Length Threshold (Pixels)	100
Line Fitting Error Threshold (Pixels)	100
Angular Difference Threshold (Degrees)	60
Linking Distance Threshold (Pixels)	100

3.3. SAR AND TOPOGRAPHY

Data fusion of SAR and photogrammetry at this site may be beneficial for lineament detection, though a direct correlation between SAR amplitude and topography cannot be made. A scatterplot comparing elevation values and SAR amplitude of the site was

generated using European Space Agency (ESA) Sentinel Applications Platform (SNAP). (Figure 6) The scatterplot was used to investigate the relationship between elevation and SAR amplitude. The scatterplot function displays the elevation plotted against SAR VH intensity. Regions with a high number of pixels are shown in yellow, a medium number of pixels in red, and individual values are shown in black. There is no direct correlation between elevation and SAR amplitude in this dataset, though PCA data fusion can possibly be used to find a correlation between multiple SAR amplitude datasets and elevation. The approach at this site may not be effective at other sites and more research is needed to identify datasets useful for a more direct correlation of SAR and topography. Possible datasets for further research of topography and PCA data fusion include LiDAR, InSAR, and photogrammetry.

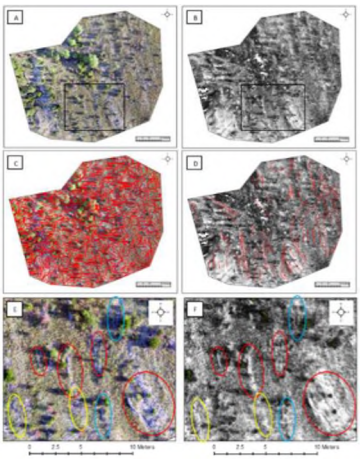

Figure 5. Lineaments detection analysis. A) Original orthomosaic. B) Fused orthomosaic. C) Automated lineament detection using original orthomosaic. D) Automated lineament detection using fused orthomosaic. E) Manual inspection of orthomosaic lineament visibility. F) Manual inspection of fused orthomosaic lineament visibility.

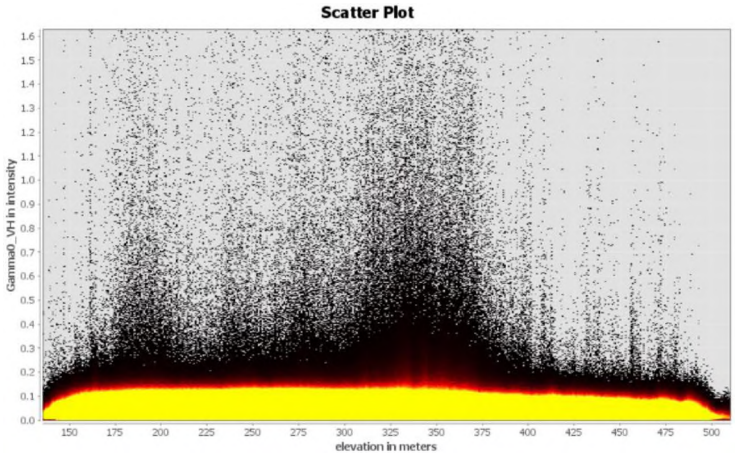

Figure 6. Scatterplot of SRTM DEM and Sentinel-1 SAR amplitude.

4. CONCLUSION

Data fusion of various satellite-borne products is routine within mapping platforms. SAR and LiDAR products have previously been fused to optical sensor data products to produce enhanced spectral and spatial characteristics. Fusion of photogrammetric data products to other data products has not yet been investigated thoroughly. This study investigates the PCA method of fusing UAV-acquired photogrammetry with Sentinel-1 SAR to improve digital elevation estimates in areas where LiDAR data are not available and to explore the potential for fused lineament visibility in the fused data set.

Comparisons of elevations estimated using LIDAR, only SAR data, only photogrammetry data, and fused SAR-photogrammetry data indicate that the fused data product does provide more accurate elevation estimates. The improvement in accuracy of the fused data set can be visually assessed by comparing the LIDAR-derived elevations (Figure 4B) and the fused data elevations (Figure 4D) and is statistically supported (Table

1). The results of this study indicate that fused SAR and photogrammetry data might be useful in developing more accurate terrain models in areas where LiDAR data are prohibitively expensive.

For detecting lineaments, the fused data product was useful in reducing the number of "false" positive" lineaments when automated detection techniques were used. The original orthomosaic has approximately 20 times more lineaments detected than the fused data set, but these "lineaments" appear to be largely related to vegetation and are not useful for geologic or topographic interpretation. Fused SAR and photogrammetry orthomosaics offer the resolution needed to detect lineaments, and the reduced impact of vegetation in the fused image makes automated detection possible, although human review of the detected lineaments is still advised.

Although this study has been useful for examining some applications of fusing SAR and photogrammetry data, many other potential benefits remain unexplored. Other pansharpening methods (in addition to PCA) of image enhancement of orthomosaics still need to be investigated to explore the potential benefits of varying spatial and spectral resolution manipulation. The particular benefits of each method of pansharpening will largely be determined by the desired application of the final data product. Also, though this investigation used Sentinel-1 SAR data for the data fusion, the preservation and enhancement of topography relied mainly on the SRTM DEM data within the radiometric correction process and subsequent co-registration. Future investigations could include the benefits of routine SRTM DEM fusion of data to photogrammetry for enhanced geocoding in the UAV data acquisition field for use in mining, construction, architectural, or humanitarian and disaster response applications.

REFERENCES

Abdelkareem, M., Ghoneim, E., El-Baz, F., Askalany, M., 2012. New insight on paleoriver development in the Nile basin of the eastern Sahara. J. African Earth Sci. 62, 35–40. https://doi.org/10.1016/j.jafrearsci.2011.09.001

Alexandr, F., 2017. Automated lineament analysis to assess geodynamic activity areas. Procedia Comput. Sci. 121, 699–706. https://doi.org/10.1016/j.procs.2017.11.091

Amro, I., Mateos, J., Vega, M., Molina, R., Katsaggelos, A.K., 2011. A survey of classical methods and new trends in pansharpening of multispectral images. J. Adv. Signal Process. 1–22.

Belfiore, O.R., Meneghini, C., Parente, C., Santamaria, R., 2016. Application of different pan-sharpening methods on Worldview-3 images. ARPN J. Eng. Appl. Sci. 11, 490–496.

Chabot, D., Dillon, C., Shemrock, A., Weissflog, N., Sager, E.P.S., 2018. An Object-Based Image Analysis Workflow for Monitoring Shallow-Water Aquatic Vegetation in Multispectral Drone Imagery. Int. J. Geo-Information. https://doi.org/10.3390/ijgi7080294

Ciampalini, A., Raspini, F., Frodella, W., Bardi, F., Bianchini, S., Moretti, S., 2016. The effectiveness of high-resolution LiDAR data combined with PSInSAR data in landslide study. Landslides 399–410. https://doi.org/10.1007/s10346-015-0663-5

Devi, M.B., Devanathan, R., 2019. Pansharpening of Remote Sensing Data of Earth Satellite Images. Procedia 6, 353–363.

Farahbakhsh, E., Chandra, R., Olierook, H.K.H., Scalzo, R., Clark, C., Reddy, S.M., Müller, R.D., Farahbakhsh, E., Chandra, R., Olierook, H.K.H., Scalzo, R., Clark, C., Reddy, S.M., Müller, R.D., 2020. Computer vision-based framework for extracting tectonic lineaments from optical remote sensing data. Int. J. Remote Sens. 41, 1760–1787. https://doi.org/10.1080/01431161.2019.1674462

Frost, V.S., Member, S., Stiles, J.A., Member, S., 1982. A Model for Radar Images and Its Application to Adaptive Digital Filtering of Multiplicative Noise. IEEE Trans. Pattern Anal. Mach. Intell. 8, 231–239.

Gaber, A., Koch, M., Griesh, M.H., Sato, M., 2011. SAR remote sensing of buried faults: Implications for groundwater exploration in the western desert of Egypt. Sens. Imaging 12, 133–151. https://doi.org/10.1007/s11220-011-0066-1

Ghassemian, H., 2016. A review of remote sensing image fusion methods. Inf. Fusion 32, 75–89. https://doi.org/10.1016/j.inffus.2016.03.003

Glenn, N.F., Streutker, D.R., Chadwick, D.J., Thackray, G.D., Dorsch, S.J., 2006. Analysis of LiDAR-derived topographic information for characterizing and differentiating landslide morphology and activity. Geomorphology 73, 131–148. https://doi.org/10.1016/j.geomorph.2005.07.006

Gomes, L., Rocha, D.M., César, A., Pires, B., Carmelo, A.C., Oswaldo, J., Filho, D.A., 2014. Geophysical characterization of the Azimuth 125 ◦ lineament with aeromagnetic data : Contributions to the geology of central Brazil. Precambrian Res. 249, 273–287. https://doi.org/10.1016/j.precamres.2014.05.005

Kupidura, P., 2016. Comparison of filters dedicated to speckle suppression in SAR Images. Int. Arch. Photogramm. Remote Sens. Spat. Inf. Sci. XLI, 12–19. https://doi.org/10.5194/isprsarchives-XLI-B7-269-2016

Laurencelle, J., Logan, T., Gens, R., 2015. ASF Radiometrically Terrain Corrected ALOS PALSAR products Product guide (No. 1.2). ASF Engineering.

Luo, Q., Hu, M., Zhao, Z., Li, J., Zeng, Z., 2020. Design and experiments of X-type artificial control targets for a UAV-LiDAR system. Int. J. Remote Sens. 41, 3307–3321. https://doi.org/10.1080/01431161.2019.1701210

Mahyoub, S., Fadil, A., Mansour, E.M., Rhinane, H., Al-nahmi, F., 2019. Fusing of optical and synthetic aperture radar (SAR) remote sensing data: a systematic literature review (SLR). Int. Arch. Photogramm. Remote Sens. Spat. Inf. Sci. XLII, 10–11.

Milas, A.S., Warner, T.A., Younan, N.H., Balenovic, I., Larson, M.D., Simic, A., Warner, T.A., Younan, N.H., Balenovic, I., 2019. Preface for the Special Issue of IJRS Drones section in conjunction with the 6th UAS4Enviro conference Preface for the Special Issue of IJRS Drones section in. Int. J. Remote Sens. 40, 9065–9069. https://doi.org/10.1080/01431161.2019.1658409

Noureldin, A., Karamat, T.B., Georgy, J., 2013. Fundamentals of inertial navigation, satellite-based positioning and their integration, Fundamentals of Inertial Navigation, Satellite-Based Positioning and their Integration. https://doi.org/10.1007/978-3-642-30466-8

Olierook, H.K.H., Scalzo, R., Kohn, D., Chandra, R., Farahbakhsh, E., Houseman, G., Clark, C., Reddy, S.M., Müller, R.D., 2019. Bayesian geological and geophysical data fusion for the construction and uncertainty quantification of 3D geological models. Solid Earth Discuss. 1–34.

Oyawale, A.A., Adeoti, F.O., Ajayi, T.R., Omitogun, A.A., 2020. Applications of remote sensing and geographic information system (GIS) in regional lineament mapping and structural analysis in Ikare Area , Southwestern Nigeria. J. Geol. Min. Res. 12, 13–24. https://doi.org/10.5897/JGMR2019.0310

Pan, Y., Ren, C., Liang, Y., Zhang, Z., Shi, Y., 2020. Inversion of surface vegetation water content based on GNSS - IR and MODIS data fusion. Satell. Navig. 1–15. https://doi.org/10.1186/s43020-020-00021-z

Pavez, A., Remy, D., Bonvalot, S., Diament, M., Gabalda, G., Froger, J., 2006. Insight into ground deformations at Lascar volcano (Chile) from SAR interferometry, photogrammetry and GPS data : Implications on volcano dynamics and future space monitoring. Remote Sens. Environ. 100, 307–320. https://doi.org/10.1016/j.rse.2005.10.013

Pavlic, G., Singhroy, V., Duk-Rodkin, A., Alasset, P., 2008. Satellite data fusion techniques for terrain and surficial geological mapping, in: IEEE IGARSS. pp. 314–317. https://doi.org/10.1109/IGARSS.2008.4779346

Rahnama, M., Gloaguen, R., 2014. TecLines: A MATLAB-Based Toolbox for Tectonic Lineament Analysis from Satellite Images and DEMs, Part 1: Line Segment Detection and Extraction. Remote Sens. 5938–5958. https://doi.org/10.3390/rs6075938

Shahdoosti, H.R., Ghassemian, H., 2016. Combining the spectral PCA and spatial PCA fusion methods by an optimal filter. Inf. Fusion 27, 150–160. https://doi.org/10.1016/j.inffus.2015.06.006

Small, D., 2011. Flattening Gamma : Radiometric Terrain Correction for SAR Imagery. IEEE Trans. Geosci. Remote Sens. 49, 3081–3093.

Strozzi, T., Delaloye, R., Kääb, A., Ambrosi, C., Perruchoud, E., 2010. Combined observations of rock mass movements using satellite SAR interferometry , differential GPS , airborne digital photogrammetry , and airborne photography interpretation. J. Geophys. Res. 115, 1–12. https://doi.org/10.1029/2009JF001311

Tagnon, B.O., 2016. Statistical and Geostatistical Analysis of Lineaments Network Mapped in The Precambrian Basement : Case of Divo-Oume Region (Southern Cote d ' Ivoire). Eur. Sci. J. 12, 299–318. https://doi.org/10.19044/esj.2016.v12n33p299

Thannoun, R.G., 2013. Automatic Extraction and Geospatial Analysis of Lineaments and their Tectonic Significance in some areas of Northern Iraq using Remote Sensing Techniques and GIS. Int. J. Enhanc. Reseaarch Sci. Technol. Eng. 2, 1–11.

Vasuki, Y., Holden, E., Kovesi, P., Micklethwaite, S., 2014. Semi-automatic mapping of geological structures using UAV-based photogrammetric data : An image analysis approach. Comput. Geosci. 69, 22–32. https://doi.org/10.1016/j.cageo.2014.04.012

Vijayaraj, V., Younan, N.H., Hara, C.G.O., 2006. Concepts of Image Fusion in Remote Sensing Applications, in: 2006 IEEE International Symposium on Geoscience and Remote Sensing. pp. 3781–3784. https://doi.org/10.1109/IGARSS.2006.973

Walker, P.J.P., 2013. Basis of an Australian Radar Soil Moisture Algorithm Theoretical Baseline Document (ATBD).

Wang, Xiaofei, Wang, Xiaoyi, 2020. Spatiotemporal Fusion of Remote Sensing Image Based on Deep Learning. J. Sensors 2020.

Xu, G., Xu, Y., 2016. GPS: Theory, algorithms and applications, third edition. GPS Theory, Algorithms Appl. Third Ed. 1–489. https://doi.org/10.1007/978-3-662-50367-6

Xu, W., Lan, Y., Li, Y., Luo, Y., He, Z., 2019. Classification method of cultivated land based on UAV visible light remote sensing. Int. J. Agric. Biol. Eng. 12, 103–109. https://doi.org/10.25165/j.ijabe.20191203.4754

Yeomans, C.M., Middleton, M., Shail, R.K., Grebby, S., Lusty, P.A.J., 2019. Integrated Object-Based Image Analysis for semi-automated geological lineament detection in southwest England. Comput. Geosci. 123, 137–148. https://doi.org/10.1016/j.cageo.2018.11.005

Zhang, X., Tang, X., Gao, X., Zhao, H., 2018. Multitemporal Soil Moisture Retrieval over Bare Agricultural Areas by Means of Alpha Model with Multisensor SAR Data. Adv. Meteorol. 2018, 17.

Zhu, X.X., Member, S., Montazeri, S., Gisinger, C., Hanssen, R.F., Member, S., Bamler, R., 2016. Geodetic SAR Tomography. IEEE Trans. Geosci. Remote Sens. 54, 18.

II. LINEAMENT EXTRACTION FROM SYNTHETIC APERTURE RADAR (SAR) AND MAGNETOMETRY FUSED DATA PRODUCTS FOR GROUNDWATER POTENTIALITY EXPLORATION: A CASE STUDY IN GULU DISTRICT, UGANDA

Rachel Jones

Deparment of Geological Engineering, Missouri University of Science and Technology, Rolla, MO 65409

ABSTRACT

Automated detection of fracture networks using remotely sensed data is a technique for assessing potential groundwater availability over large areas in fractured rock aquifers. Fractures are conduits for fluid flow and an important source of aquifer recharge. Existing techniques for detecting fractures usually use a single type of remote sensing data, which is not always effective in areas where the terrain obscures lineaments expressions. For example, SAR data are commonly used for the development of lineament maps, but curvilinear surface hydrologic features are often detected simultaneously with fracture networks, so distinguishing between fractures and surface features is difficult. Magnetic geophysical data are also used to map fracture networks, but often detect only a subset of lineaments within a fracture network. This research seeks to overcome these problems by fusing multiple Alos Palsar L-Band SAR polarimetric decompositions with airborne magnetic geophysical products to generate a lineament map that maximizes the number of lineaments detected while excluding stream systems from the end product. PauliRGB, Van Zyl, and circular SAR products were used in combination with the magnetic analytic signal,

horizontal gradient, and first vertical derivative to evaluate the most effective combination of data fusion products for lineament detection. Automated lineament detection algorithms were applied to the fused data sets, and the efficacy of different data combinations was tested by comparing the fused data products with validated field data from previously published research showing precise locations of in situ surface lineaments. Rose diagrams of all extracted lineaments were generated to validate the extracted lineaments with fracture network directional trends in previously published research. Extracted lineaments were also compared to lineaments manually observed on aerial imagery. The Van Zyl decomposition fused with the first vertical derivative magnetic data produced a lineament map most in conformity with previously published data.

1. INTRODUCTION

Regions with relatively thin soil layers that are underlain by igneous, metamorphic, or fine-grained sedimentary rock often depend on fractured rock aquifers to supply safe drinking water (Alexandr, 2017). Some regions in sub-Saharan Africa have this geology (Fenta et al., 2014), and in these regions, wells must be carefully located within intersecting fracture networks to supply sufficient water. Identifying these fracture networks is not straightforward (Farahbakhsh et al., 2020), and geologic field investigations are sometimes hampered by civil unrest or natural hazards. Remote sensing to detect fracture networks in these areas reduces the danger to aid workers by decreasing the time spent in the field and can save money by reducing the number of dry wells drilled. This research focuses on

the Gulu District in Uganda as a case study in remote sensing of fracture networks for groundwater exploration.

Many fracture networks or fault zones occur as linear or curvilinear features, and detection of these lineations for groundwater resource exploration or aquifer characterization using remotely sensed data is common (Brunner et al., 2007; Farahbakhsh et al., 2020; Oyawale et al., 2020; Tagnon, 2016). Traditionally, lineament extraction is done using aerial photography or satellite imagery (Thannoun, 2013). Aerial photography can be very useful for detecting lineament networks, but vegetation sometimes impedes image analysis. Therefore, methods that can penetrate foliage, such as synthetic aperture radar (SAR) and airborne magnetometry, may be more useful for this application. These methods are sensitive to different parameters and have different sampling depths, so have potential to provide an improved method of lineament detection.

SAR data are sensitive to changes in the near-surface dielectric permittivity, which is often related to soil moisture. Gaber et al. (2011) demonstrated the ability of SAR to detect surface lineaments in Wadi El-Kubanyia, Egypt, where the subsurface material is predominantly windblown dry sand. Surface expressions of fractures and drainage channels were derived from geologic maps, correlated with ALOS/PALSAR data, and validated with GPR data at three study sites. Drainage channels were subsequently excluded from the fracture network using classification algorithms. The resultant SAR images indicated multiple subsurface fracture networks. In another study, SAR data were used to identify surficial and shallow subsurface fracture zones and buried drainage channels (Yeomans et al., 2019). Although buried drainage channels, which are typically filled with high-permeability sediment, can be very important for understanding

groundwater seepage, it is necessary to isolate fracture networks from buried drainage channels to better understand deeper aquifer recharge and groundwater flow paths (Olierook et al., 2019). Thus, SAR data may be used most effectively when combined with another data type that can better distinguish between fractures and buried drainage channels.

One of the great strengths of SAR data is its ability to penetrate surficial vegetation and some distance into the subsurface. The penetration through the vegetation is a function of the incidence angle of the satellite, the signal frequency and polarization, and the density of vegetation (Srivastava et al., 2006). L-band SAR data can often penetrate moderate vegetation (Kim and van Zyl, 2009). Once the signal encounters the soil surface, the penetration depth of SAR data varies as a function of soil moisture, surface roughness, and SAR wavelength. Penetration depth is greater in dry soils than in wet soils (Blom et al., 1984), and is usually greater in rough, coarse-grained soils than in smoother fine-grained soils (Kim and van Zyl, 2009). For the relationship with wavelength, X-Band SAR has the least surface penetration, C-Band has varying levels of penetration, and L-Band has the greatest penetration depth. Since the penetration depth is a function of several different parameters, some of which are usually unknown, it is difficult to calculate the penetration depth without *in situ* data acquired simultaneously with SAR data for confirmation of results (Gaber et al., 2011). Ground Penetrating Radar (GPR) investigations (Gaber et al, 2011) confirm that L-band SAR data penetrated to a depth of up to approximately 6 meters in dry sand. In these favorable conditions, surveys in the Sahara have revealed paleochannels, sometimes called "radar rivers", paleolakes, paleotopographies, and various archaeological artifacts (AbuBakr et al, 2013).

Magnetometry is a geophysical technique that has been used to identify deeper fracture systems. Magnetic geophysical methods detect the remnant magnetism of ferromagnetic materials, where remnant magnetism is the residual magnetism present in a material in the absence of an induced magnetic field. Remnant magnetic data are measured in airborne magnetometry missions by sending a magnetic field into the subsurface, then measuring the magnetic field that results as the induced field interacts with the geologic media. The remnant magnetism is the difference between the measured and induced magnetic fields and is used to detect magnetic anomalies associated with the magnetic fabric of various geologic structures. The Analytic Signal Amplitude (ASA) is a filter that is used to identify the locations of shallow magnetic sources with high remnant magnetization (Li, 2001). The analytic signal is derived from the amplitudes of the three dimensional magnetism of the source body and is used to define contrasts and depths of sensed magnetic bodies. (Reynolds, 1997)

Magnetometry is a geophysical technique that has been used to identify magnetic minerals indicative of deeper faults and fracture systems. Magnetometry detects the remnant magnetism of ferromagnetic materials, where remnant magnetism is the residual magnetism present in a material in the absence of an induced magnetic field. Remnant magnetic data are measured in airborne magnetic missions by inducing a electromagnetic current into the subsurface, then measuring the change of magnetic flux, with respect to time, of the magnetic field that results as the induced field interacts with the geologic media. The remnant magnetism is the difference between the measured and induced magnetic fields and is used to detect magnetic anomalies associated with the magnetic fabric of various geologic structures. The Analytic Signal Amplitude (ASA) is a filter that

is used to identify the locations of shallow magnetic sources with high remnant magnetization (Li, 2001). The analytic signal is derived from the amplitudes of the three-dimensional magnetic response of the source body and is used to define contrasts and depths of sensed magnetic bodies (Reynolds, 1997).

Airborne TDEM data acquired over Uganda have been used for mining and petroleum exploration, to map geologic structures, and to correlate magnetic data with various other geophysical datasets. Fractures of the ASZ in the Gulu District have been detected with the magnetic data and have been confirmed in the field by Katumwehe, 2016, et. al. for previous structural analysis of the ASZ. Field work conducted by Saalmann, 2017, et. al. validated the location of fracture zones within the Aswa Shear Zone as well as magnetic testing of field samples within the fracture network (Saalmann et al., 2016). In situ measurements of the strike and dip of fractures within the shear zone correlated with the remotely sensed fractures. It was also noted that areas of the fractures are not fully detected in the outcrops and, thus the magnetic maps assist in field studies to trace the extents of surface fractures. Comparison of field results and predictions based on magnetic data also showed that the magnetic data sometimes indicated fracture sets that had originally been overlooked in the field, but which could be traced after their location was indicated by magnetic data. Samples of magnetic rocks were collected along the fracture zone to confirm the presence of the magnetic fabric and correlate remotely sensed data with field samples.

Magnetic methods can be used to detect fractures because differential remanent magnetism in various rock units creates a magnetic anomaly along steeply dipping lithologic interfaces, especially in areas of tectonic displacement. The fractures also have

a magnetic response because they are often filled with iron-bearing ferrisols, which have eroded from the overlying soil layers (Awad et al., 2019). Magnetometry is ideal for sensing fracture networks at the exclusion of drainage networks (Hall, 1986), because buried drainage channels do not usually have the same magnetic anomalies as deeper fractures. However, magnetic methods are not as sensitive to surface fractures as L-bandSAR methods, so the number of detected lineaments found using magnetic data is far less than that which is sensed using SAR data. Thus, the number of potential borehole drilling locations may be underestimated if only magnetic data are used (Elbeih, 2014). The goal of this research is to fuse SAR data with magnetic data to extract lineaments of fracture networks from a single data product. The specific objectives are to improve the detected fracture network and to isolate fracture networks from hydrologic channels.

Automated lineament detection of surface and subsurface fracture networks is necessary because lineament analysis is typically completed manually based on visual inspection of topographic and aerial maps (Alexandr, 2017). Thus, lineament analysis is time consuming which increases the economic disadvantages associated with structural analysis of geomorphological features. Automated lineament analysis reduces the inaccuracies of human interpretation and enhances complex lineament networks (Rahnama and Gloaguen, 2014). A literature review of SAR fused data products (Mahyoub et al., 2019) lists numerous studies that conclude the usefulness of SAR fused data products for surface lineament analysis including road network extraction, paleochannel detection, lithology investigations, and structural analysis. This research introduces magnetic data as a novel addition to data fusion techniques for lineament extraction.

2. MATERIALS AND METHODS

2.1. STUDY AREA

Uganda is situated along the western boundary of the East African Rift System (EARS). EARS is an active continental rift zone of a divergent tectonic system composed of the Somali plate and the Nubian Plate (Hall and Diggens, 2011). The study area is withing the Gulu District, which is located within the Nubian plate in the Aswa Shear Zone (ASZ), a structure that stretches over 1,000 km from southwestern South Sudan to western Kenya in a NW-SE trend (Saalmann, et al, 2016). The ASZ presents an extensive fracture network conducive to groundwater infiltration(Katumwehe et al., 2016).

The study area is composed of Archaean plutonic rocks of a gneissic and granitoid composition (Saalmann et al, 2016) between elevations of approximately 700 m and 1,100 m above mean sea level. Deeper aquifers exist in this region in the weathered and fractured bedrock, and the permeability of these aquifers depends on the number, distribution, and connectivity of these fractures. The depth to bedrock within Gulu District is highly variable and ranges from surface outcrops to 70 meters deep while the average depth to bedrock is 25 m (GWB, 2018). The soil is predominantly ferralsols formed from weathered bedrock (Macdonald and Davies, 2000a). Ferralsols sometimes have shallow SAR depth penetration due to their clayey composition, but these soils are well drained, so SAR penetration to at least shallow depths is expected.

2.2. SAR DATA ACQUISITION AND PROCESSING

The Advanced Land Observing Satellite (ALOS) was developed by the Japan Aerospace Exploration Agency and carried the Phased Array type L-Band Synthetic Aperture Radar (PALSAR) instrument which acquired data from 2006 through 2011. ALOS PALSAR acquired SAR data from variable observation geometries with various resolutions and polarizations and is made available by the European Space Agency for research purposes. The SAR data used for this research was acquired during a period of low solar activity and the location of the study area is at low latitude within the tropics. The calibration algorithms adopted by the European Space Agency (ESA) correct for the Faraday effect, therefore signal distortion within the linearly polarized data should be negligible.

The ALOS PALSAR data were acquired using high resolution global imagery (10 m) from 2006 through 2011 in all four polarizations (QUAD-POL) as described in Table 1. Field investigations have shown that Alos Palsar L-Band (1.27 GHz, 24 cm) data penetrate low electrical loss materials to variable depths (Lasaponara and Masini, 2013), which enables sensing of subsurface structures (Gaber et al., 2011). QUAD-POL data enhances the viewing geometries of radar backscatter which aids in detection of buried structures by penetrating the soil structure using variable look angles which aids in the detection of buried structures.

Radiometric Terrain Correction (RTC) processing of SAR data removes spatial distortions that are present in the data product and corrects for topographical errors that result from the side-looking geometry of the SAR sensor. The European Space Agency (ESA) publishes the SNAP S1TBX Toolbox that was used for RTC processing of the Alos

Palsar data (Figure 1). The orbit file was downloaded and applied to the data for geocoding the precise orbit determination (POD) (Escobar et al., 2017). This step ensures subpixel GPS accuracy between the sensor coordinate system and the geoid (Dubey et al., 2018). The data product was then calibrated to transform the sensed data to the magnitude of the radar backscatter coefficient, the fundamental data product used for quantifiable interpretation of SAR image data.

Table 1. Data characteristics of ALOS/PALSAR SAR data acquired over Gulu District, Uganda (Meadows et al, 2008).

Data Characteristics	
Sensor	ALOS/PALSAR
Format Level	1.1
Wavelength	22.9 cm
Polarization	HH+HV+VV+VH
Swath Width	21.5 km
Pixel Spacing, Range	9.4 m
Pixel Spacing, Azimuth	3.6 m
Ground Pixel Resolution (Range)	3.8 m
Ground Pixel Resolution (Azimuth)	18.7 m
Ground Resolution	24.7 m
Resolution (Range x Azimuth), m (SLC)	30 x 10

Multilooking the data was performed to segment the data into smaller sections for more accurate despeckling in the next step of processing. Despeckling is performed to reduce the radar noise in the sensed backscatter (Rott, 1984) that is present in the radar cross section (RCS) (Frost et al., 1982). The Lee filter (Kupidura, 2016) was used to preserve the edges in the image details while removing noise present using a minimum mean square algorithm (Wald et al., 2009). Next, the data was deskewed to adapt the radar

data to a zero Doppler geometry which corrects for satellite orbit velocity (Zeng et al., 2016). Terrain correction and flattening algorithms (Small, 2011) were applied for final processing. This final step geocodes the image pixels into an appropriate spatial relationship with the terrain and removes topographic effects.

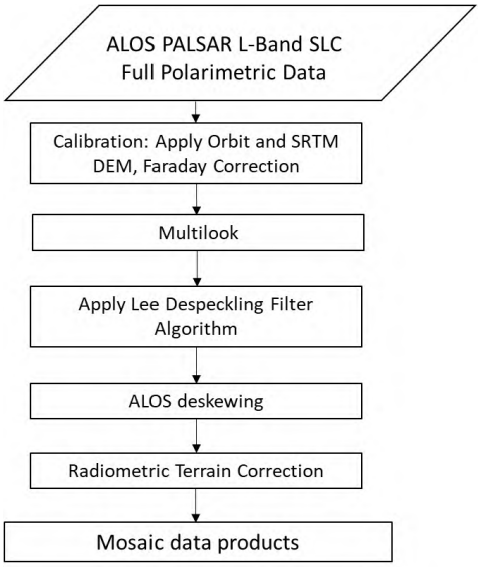

Figure 1. Workflow for radiometric processing of ALOS/PALSAR data.

Polarimetric decompositions (Appendix A, Appendix B) are used to reveal information about various surface properties and their backscattering mechanisms. Two general types of decompositions are Coherent Target Decomposition (CTD) and Incoherent Target Decomposition (ICTD). Coherent targets are used to study manmade objects which are known to have linear and uniform scattering mechanisms. Incoherent targets are natural targets the express distributed and non-uniform backscattering

properties. Another type of decomposition is circular polarization, which combines CTD and ICTD. Circular polarizations are not affected by Faraday rotation (Meyer and Nicoll, 2008) due to the curvilinear nature of the waveform. Experiments conducted in Eqypt revealed that the circular polarization product may more completely reveal buried faults and fault zone boundaries because strike zone depth and orientation occur in various directions. Subsurface structures sensed with only the linear polarizations will only reveal fault zone boundaries that occur in the direction of linear data transmitted and received (Gaber et al., 2011). Based on the results of previous researchers (Gaber et al., 2011), the PauliRGB CTD, the Van Zyl ICTD, and a synthesized circular polarimetric radar scattering matrix were used in addition to coherent and incoherent scattering targets (Figure 2). Figure 2 shows the image results from radar processing of all three decomposition methods. The PauliRGB decomposition (Figure 2A) aids in the classification of uniform scattering targets, the Van Zyl decomposition (Figure 2B) aids in the classification of distributed scattering targets, and the circular decomposition (Figure 2C) enhances angular scattering targets for classification purposes.

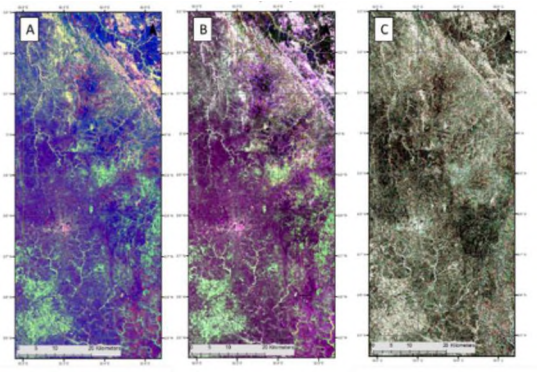

Figure 2. Alos Palsar decompositions; A: PauliRGB, B: Van Zyl; C: Circular.

2.3. MAGNETOMETRY DATA ACQUISITION AND PROCESSING

The Uganda Directorate of Geological Survey and Mines (DGSM) acquired airborne magnetic, electromagnetic, and radiometric geophysical data in 2006. The airborne magnetic survey for the Gulu District was flown over an area of approximately 18,197 km^2 with a line spacing of 200 m and a terrain clearance of 80 m, for a total of 101,290 km of survey lines (Republic of Uganda, 2019). The magnetic data was gridded to 50 meter cell size to produce various magnetic data products.

Airborne magnetic data acquired over Uganda has been used for mining and petroleum exploration, to map geologic structures, and to correlate magnetic data with various other geophysical datasets. Fractures of the ASZ in the Gulu District have been detected with the magnetic data and have been confirmed in the field by Katumwehe, 2016, et. al. for previous structural analysis of the ASZ. Field work conducted by Saalmann, 2017, et. al. validated the location of fracture zones within the Aswa Shear Zone as well as magnetic testing of field samples within the fracture network (Saalmann et al., 2016). In situ measurements of the strike and dip of fractures within the shear zone correlated with the remotely sensed fractures. It was also noted that areas of the fractures are not fully detected in the outcrops and, thus the magnetic maps assist in field studies to trace the extents of surface fractures. Samples of magnetic rocks were collected along the fracture zone to confirm the presence of the magnetic fabric and correlate remotely sensed data with field samples.

The magnetic products provided by the DGSM for this study (Figure 2.3) consist of the total magnetic intensity (TMI), analytic signal amplitude (ASA), the horizontal derivative (HD), and the first vertical derivative (FVD). The magnetic data was processed

using Seequent Geosoft Oasis montaj GM-SYS 3D version 9.8, which applies a filter to the acquired magnetic dataset to obtain the horizontal gradients ($\delta T/\delta x$ and $\delta T/\delta y$) (Eq. 1) and a fast Fourier transform (FFT) to derive the vertical gradient ($\delta T/\delta z$). Thus, the amplitude, A, of the analytic signal of the measured field, T, is given by:

$$|A(x,y)| = [(\delta T/\delta x)^2 + (\delta T/\delta y)^2 + (\delta T/\delta z)^2]^{\frac{1}{2}} \quad \text{Eq. 1}$$

Isolating the horizontal gradient from the above equation results in the ability to interpret magnetic anomalies present in an otherwise uniform magnetic fabric. The horizontal gradient is used in boundary analysis to identify regional fractures by emphasizing lineaments using edge filters. This is because the horizontal gradient is steepest at the edges of abrupt magnetic changes in both the x and y directions (Adeyinka et al., 2016).

The vertical gradient is used to remove the regional magnetic field and isolate magnetic anomalies that are highlighted in the data product. The first vertical derivative emphasizes the shift in the vertical direction between positive and negative anomalies. (Al-badani and Al-wathaf, 2018) The benefit of using the first vertical derivative, rather than the second vertical derivative that is often used, is that first order methods are less sensitive to noise (Salem et al., 2007).

2.4. DATA FUSION

PC sharpening is used in image analysis by sharpening a low spatial resolution product with a high spatial resolution product. The various SAR products were used as the

low spatial resolution product because the process requires a multi-band spectral (MS) image for the input. The magnetic data was used as the high spatial resolution data because it is panchromatic (PAN), which is also required for the algorithm. ENVI 5.5 was used for PC sharpening so that co-registration of the georeferenced products could be performed simultaneously. The PC sharpening process first transforms the SAR MS data into a PC eigenspace and then replaces the first band of the PC data with the high resolution (PAN) magnetic data. Then an inverse transform is performed to fuse the data. Finally, the MS data is resampled using linear interpolation of four pixels using a nearest neighbor method (Figure 4).

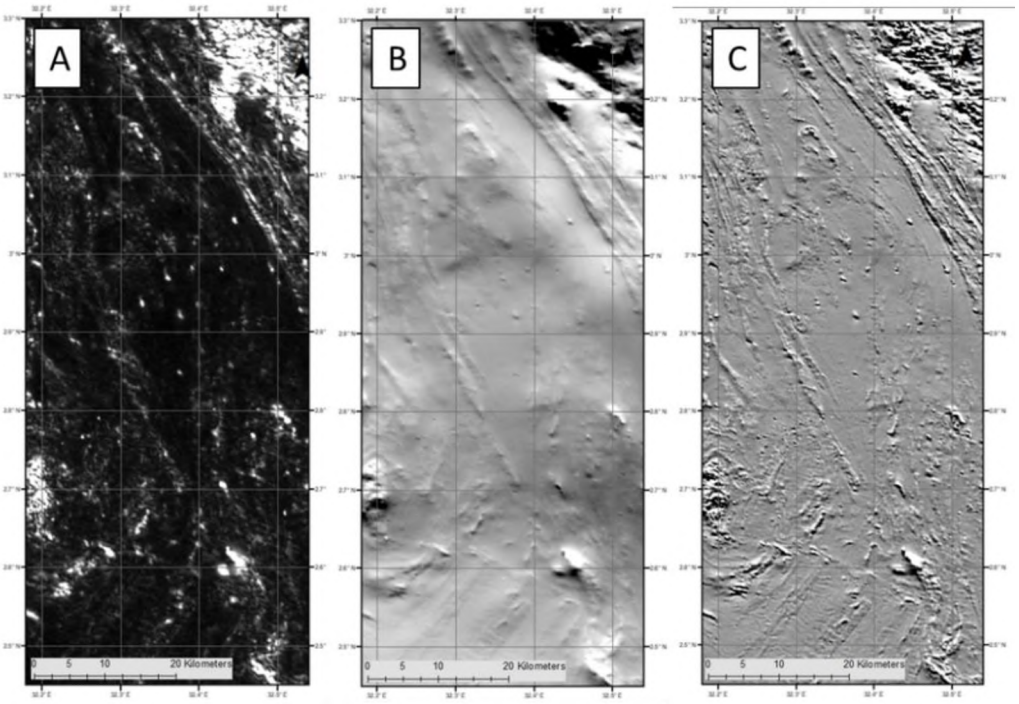

Figure 3. Airborne magnetic data acquired over Gulu District, Uganda. A) Magnetic analytic signal. B) Magnetic horizontal gradient. C) First vertical derivative.

3. THEORY

3.1. PAULI/RGB

The PauliRGB decomposition is derived from Pauli spin matrices used in quantum mechanics and is a coherent target decomposition (CTD). It is based on linear combinations of backscattering matrix vectors. PauliRGB is represented by a (3x3) Coherency **[T3]** matrix which represents scattering mechanisms within a pixel as well as their subsequent contribution to the total radar signal. A coherency matrix is used to analyze partially polarized waves by representing the correlations of the wave components (Gil, 2014). All nine elements of the [T3] Coherency matrix were computed for each pixel of the image.

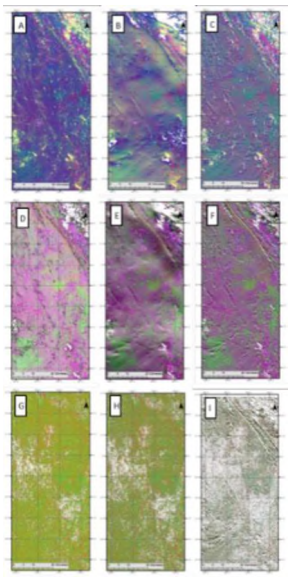

Figure 4. SAR data fused with magnetic data using PC Sharpening. A) PauliRGB/Analytic Signal. B) PauliRGB/Horizontal Gradient. C) PauliRGB/First Vertical Derivative. D) Van Zyl/Analytic Signal. E) Van Zyl/Horizontal Gradient. F) Van Zyl/First Vertical Derivative.

The final PauliRGB decomposition utilizes the diagonal elements of the matrix as the red ($T22$), green ($T33$), and blue ($T11$) (Eq. 2, Eq. 3, Eq. 4) by convention and is defined as:

$$T_{11} = |S_{HH} + S_{VV}|^2 \quad \text{Eq. 2}$$

$$T_{22} = |S_{HH} - S_{VV}|^2 \quad \text{Eq. 3}$$

$$T_{33=}2|S_{HV}|^2 \quad \text{Eq. 4}$$

PauliRGB backscattering matrix target decompositions results in a color-coding of the polarimetric channels of HH-VV, HV, and HH+VV, respectively. These polarimetric channels correspond to the backscattering mechanisms associated with double bounce scattering reflected from objects, volume scattering from object geometry, and single bounce scattering from the surface.

3.2. VAN ZYL

Van Zyl The Van Zyl decomposition is a type of ICTD and is characterized by single (surface) bounce, double bounce, and volume scattering mechanisms (Arii et al., 2011). Turkar, et al, tested various ICTD for use in classification algorithms and found that the Van Zyl decomposition yields the best results when tested for classifiers such as mangroves, water, agricultural fields, and villages. These results are reasonable since the Van Zyl method was derived to measure the natural variability in geophysical parameters

(Turkar and Bombay, 2011). The Van Zyl algorithm is a vectorized form of the Sinclair matrix used for PauliRGB decomposition and is considered an eigenvalue method (Zyl et al., 2011).

The Van Zyl decomposition utilizes a 3x3 Covariance [C3] matrix. A covariance matrix correlates each of the polarization channels and is based on the decomposition of the [T3] Coherency matrix (Van Zyl, Jakob; Kim, 2011). The [C3] covariance matrix (Eq. 5, Eq. 6, Eq. 7) is defined as:

$$C_{11} = |S_{HH}|^2 \quad \text{Eq. 5}$$

$$C_{22} = |S_{HV}|^2 \quad \text{Eq. 6}$$

$$C_{33} = |S_{VV}|^2 \quad \text{Eq. 7}$$

The resulting Van Zyl image is classified based on these parameters. The surface scatterer (C_{11}), the dihedral scatterer (C_{22}), and the diffuse scattering mechanism (C_{33}). This method finds the single, dominant scatterer for each pixel rather than the total power of the three scatterings mechanisms.

3.3. CIRCULAR POLARIZATION

A synthetic circular polarization was constructed using ESA's SNAP radar processing platform. The data was processed according to the right and left circular geometries and a scattering matrix was generated. The previously described RTC process

was employed to generate the final circular polarimetric product using the right circular vertical, right circular horizontal, and left horizontal horizontal (RCV/RCH/LHH) combination.

3.4. DATA FUSION WITH PRINCIPAL COMPONENT SHARPENING

Principal Component Analysis (PCA) is an eigenvector-based method of variable analysis used in signal processing to explain the variance between datasets. PCA sharpening is a common image processing technique that extracts the principal components of two unrelated datasets and linearly transforms them into a set of data that can be analyzed for variance (Amro et al., 2011). The final transformation of the dataset is the fusion product. The fusion product is then used for feature extraction at the pixel level. This is especially valuable for edge detection of boundaries.

Multi-sensor data fusion methods are becoming more common in the literature and are used to explore relationships between varying datasets (Ghassemian, 2016). Spatial, spectral, and temporal qualities of datasets are commonly fused to enhance complex relationships among data for analysis. Therefore, the fusion of SAR data and magnetic data, though novel, is reasonable.

3.5. LINEAMENT EXTRACTION

The practice of using remotely sensed data for lineament mapping of faults and fractures is well established for determining groundwater potential (Mutiti et al., 2010). Fractures are conduits for fluid flow and the mapping of fracture networks identifies regions of surface water infiltration into local or regional aquifers. Lineament extraction

algorithms are commonly used on remotely sensed optical, radar, and magnetic data. Surface expressions of lineaments from optical data are obstructed by vegetation and soil and the resulting lineament maps are generally only useful for regional scale analysis. Lineaments derived from radar or airborne geophysical data are commonly used and are considered definitive for precise lineament location (Brunner et al., 2007). Lineament extraction algorithms extract features from raster images that are linear or curvilinear. The extracted lineaments are then placed in a vector file for further analysis.

4. RESULTS AND DISCUSSION

Geomatica (Ontario, Canada) 2017 for Students was used for the lineament extraction algorithm on all data products (Table 2, Table 3) This algorithm requires several input parameters to derive pixel level lineament patterns. The filter radius is measured in pixel distance of the lineament to establish the edges of the lineament. A pixel size of 5 was chosen for all data products to minimize noise and maximize the detail of edges detected. The edge gradient threshold sets the binary gradient for which edges are measured and is measured with values ranging from 0 to 255. The values assigned for this parameter were established by visual inspection of the final output image. A low value for edge gradient reduces noise in the resulting lines. The curve length threshold is measured in pixels and measures the minimum length of a curve that should be considered a lineament. A uniform value of 30 pixels was used. The line fitting error threshold establishes the minimum number of pixels to link a line segment and a curve. A uniform value of 3 pixels is standard. The angular difference determines the maximum angle between two vectors to

be considered a lineament. Values of 30° and 60° were chosen dependent on the hydrological channels that were visible within the data product. Finally, the linking distance threshold is measured in pixels and defines the maximum distance between two lineaments for them to be associated.

Lineament extraction was performed on all datasets to establish lineament networks useful for hydrologic analysis of groundwater infiltration due to fractures, folds, and faults in Gulu District. (Apppendix C) SAR-derived lineaments include both the dendritic drainage channels of the river system as well as the extensive fracture network of the ASZ. Lineaments derived from the magnetic data expose only the lineaments associated with the ASZ. Extraction of lineaments from the fused products eliminated the hydrologic drainage pattern and retained the extent of the fracture system from both data products.

The fused data products display NW-SE trending structures, absent of drainage channels, and in agreement with the previously mapped structures. (Table 4) All circular datasets exhibit the greatest variability among detected lineament orientations and could not be correlated to published known lineaments. The PauliRGB fused data products were comparable to the Van Zyl fused data products in the detected orientation of lineaments, however the Van Zyl/Horizontal Gradient and Van Zyl/First Vertical Derivative fused data products displayed lineament orientations within the range of published lineament orientations. This is reasonable because published lineament maps are derived from the Horizontal Gradient and First Vertical Derivative magnetic products. Though the Van Zyl/Horizontal Gradient fused data product is within the lineament orientation range, the Van Zyl/First Vertical Derivative (Figure 5) lineament map had a mean lineament orientation (321°) most closely matching the orientation of the original dataset.

Table 2. Lineament extraction inputs for SAR and magnetic datasets.

Product	PauliRGB	Van Zyl	Circular	Analytic Signal	Horizontal Gradient	First Vertical Derivative
Filter Radius (Pixels)	5	5	5	5	5	5
Edge Gradient	10	10	50	50	5	10
Curve Length (Pixels)	30	30	30	30	20	30
Line Fitting Error (Pixels)	3	3	3	3	3	3
Angular Difference (Degrees)	60	60	60	30	30	30
Linking Distance (Pixels)	20	20	50	20	30	50

Table 3. Lineament extraction inputs for fused datasets.

Product	PauliRGB / Analytic Signal	PauliRGB / Horizontal Gradient	PauliRGB / First Vertical Derivative
Filter Radius (Pixels)	5	5	5
Edge Gradient Threshold	50	50	50
Curve Length Threshold (Pixels)	30	30	30
Line Fitting Error Threshold (Pixels)	3	3	3
Angular Difference Threshold (Degrees)	30	60	60
Linking Distance Threshold (Pixels)	50	50	50
Product	**VanZyl / Analytic Signal**	**VanZyl / Horizontal Gradient**	**VanZyl / First Vertical Derivative**
Filter Radius (Pixels)	5	5	5
Edge Gradient Threshold	50	50	50
Curve Length Threshold (Pixels)	30	30	30
Line Fitting Error Threshold (Pixels)	3	3	3
Angular Difference Threshold (Degrees)	30	30	30
Linking Distance Threshold (Pixels)	50	50	50
Product	**Circular Mosaic / Horizontal Gradient**	**Circular Mosaic / Analytic Signal**	**Circular Mosaic / First Vertical Derivative**
Filter Radius (Pixels)	5	5	5
Edge Gradient Threshold	50	50	50
Curve Length Threshold (Pixels)	30	30	30
Line Fitting Error Threshold (Pixels)	3	3	3
Angular Difference Threshold (Degrees)	60	60	60
Linking Distance Threshold (Pixels)	100	100	100

Table 4. Lineament orientations, confidence interval, and range of orientations for all datasets.

Data Product	n	Mean Orientation
Original	263	323
PaulirRGB/Analytic Signal	237	334
PauliRGB/Horizontal Gradient	228	340
PauliRGB/First Vertical Derivative	570	326
Van Zyl/Analytic Signal	447	342
Van Zyl/Horizontal Gradient	374	330
Van Zyl/First Vertical Derivative	1136	321
Circular/Analytic Signal	584	349
Circular/Horizontal Gradient	290	334
Circular/First Vertical Derivative	1032	335

Lineament extraction is routinely performed on remotely sensed optical, radar, and geophysical data. Cloud cover is an impediment to optical data within the study area while surface expressions of fracture networks scarce. Therefore, optical data cannot be depended on to sense fractures that are necessary to detect areas of aquifer recharge. Alos Palsar radar data is ideal for lineament detection in this area because of the capability of L-band SAR to penetrate surface vegetation and soil. L-band SAR detected vast networks of fractures within the ASZ but also detected lineaments of the dendritic drainage channels of the river system. Fracture networks and stream systems have different mechanisms of aquifer recharge so it is necessary to isolate the networks from one another. Magnetic data senses the fractures networks, excluding the stream system, however magnetic data does not detect as many fractures as does the radar data.

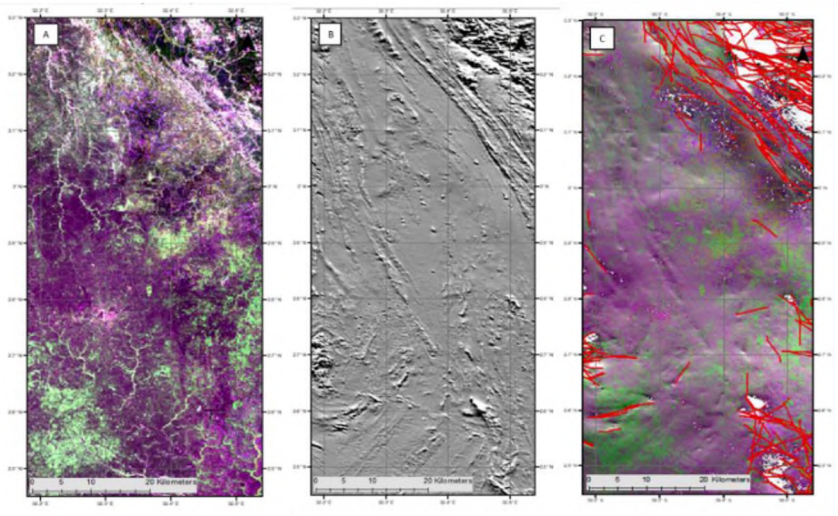

Figure 5. Van Zyl/First Vertical Derivative data fusion and lineament extraction. A) Van Zyl decomposition. B) First Vertical Derivative Decomposition. C) Van Zyl/First Vertical Derivative data fusion with lineaments.

The fusion of SAR and magnetic data combined the fracture networks of the ASZ and eliminated the curvilinear features of the drainage channels. Several radar products were used to determine which polarimetric decomposition and magnetic product yields the best combination for lineament detection. SAR polarimetric decompositions used include PauliRGB, Van Zyl, and a Circular band combination. Magnetic products include the analytic signal, horizontal gradient, and first vertical derivative of the magnetic field. Combinations of these 6 products were fused and lineaments were extracted from each fused data product. Lineament extraction was performed on each data product and rose diagrams of the lineament networks were produced for each of them.

The Van Zyl family of fusion products most closely agree with previous research performed by Katumwehe, et. al, who remotely sensed the ASZ and validated the strike and dip measurements in the field. The results of this research supplement their results.

The Van Zyl polarimetric decomposition displayed the NW-SE trending fracture networks most clearly which is also indicated by the rose diagram. Similarly, the First Vertical Derivative of the magnetic field produces a lineament network that most closely matches the previously mapped lineaments. The fusion of these two products yields 1,136 lineaments with a NW-SE trend.

5. CONCLUSIONS

Geophysical exploration programs for groundwater access in crisis and disaster areas present hazardous obstacles for personnel and require substantial economic resources for beneficial results. Investigations of crisis and disaster areas using remote sensing techniques to identify optimal borehole drilling locations is ideal for this application.

Lineaments extracted from remotely sensed data products are valuable for the identification and investigation of hydrogeologic features necessary to conduct borehole drilling programs. Polarimetric SAR enhances surficial hydrologic channels of the geomorphologic terrain by reducing the vegetative footprint. Airborne magnetic surveys yield subsurface faults, folds, and fractures that are also valuable for the identification of subsurface fluid flow.

The fusion of SAR and magnetometry is beneficial to evaluate lineament networks in study areas that are difficult to access. Magnetic geophysical data coupled with SAR data yields a fused product which more clearly defines systemic fracture networks than using either one separately. The fused product condenses lineament maps for groundwater potentiality models necessary to reduce the number of dry holes drilled in the field.

This study concludes that lineaments derived from a fusion of the magnetic analytic signal and the polarimetric Van Zyl decomposition SAR product yields the most accurate results for input into a groundwater potentiality model. More research is necessary to evaluate the effects of other fusion techniques or polarimetric decompositions on lineament extraction. This research establishes a baseline for further remotely sensed geophysical investigations in the study area.

REFERENCES

Abdelkareem, M., Ghoneim, E., El-Baz, F., Askalany, M., 2012. New insight on paleoriver development in the Nile basin of the eastern Sahara. J. African Earth Sci. 62, 35–40. https://doi.org/10.1016/j.jafrearsci.2011.09.001

AbuBakr, M., Ghoneim, E., El-Baz, F., Zeneldin, M., Zeid, S., 2013. Use of radar data to unveil the paleolakes and the ancestral course of Wadi El-Arish, Sinai Peninsula, Egypt. Geomorphology 194, 34–45. https://doi.org/10.1016/j.geomorph.2013.04.005

Adeyinka, M., Idowu, A., Alaba, M., Adedapo, M., 2016. Interpretation of high resolution aeromagnetic data for lineaments study and occurrence of Banded Iron Formation in Ogbomoso area , Southwestern Nigeria. J. African Earth Sci. 114, 43–53. https://doi.org/10.1016/j.jafrearsci.2015.10.015

Ahmad, I., Verma, M.K., 2018. Application of Analytic Hierarchy Process in Water Resources Planning : A GIS Based Approach in the Identification of Suitable Site for Water Storage. Water Resour. Manag. 5093–5114.

Al-badani, M.A., Al-wathaf, Y.M., 2018. Using the aeromagnetic data for mapping the basement depth and contact locations , at southern part of Tihamah region , western Yemen. Egypt. J. Pet. 27, 485–495. https://doi.org/10.1016/j.ejpe.2017.07.015

Alexandr, F., 2017. Automated lineament analysis to assess geodynamic activity areas. Procedia Comput. Sci. 121, 699–706. https://doi.org/10.1016/j.procs.2017.11.091

Amro, I., Mateos, J., Vega, M., Molina, R., Katsaggelos, A.K., 2011. A survey of classical methods and new trends in pansharpening of multispectral images. J. Adv. Signal Process. 1–22.

Arii, M., Zyl, J.J. Van, Kim, Y., Member, S., 2011. Adaptive Model-Based Decomposition of Polarimetric SAR Covariance Matrices. IEEE Trans. Geosci. Remote Sens. 49, 1104–1113. https://doi.org/10.1109/TGRS.2010.2076285

Awad, S., Araffa, S., Helaly, A.S., Khozium, A., Lala, A.M.S., Soliman, S.A., Hassan, N.M., Awad, S., Araffa, S., Helaly, A.S., Khozium, A., Amir, M.S., Awad, S., Araffa, S., Helaly, A.S., Khozium, A., 2019. Delineating groundwater and subsurface structures by using 2D resistivity, gravity and 3D magnetic data NRIAG J. Astron. Geophys. 4, 134–146. https://doi.org/10.1016/j.nrjag.2015.06.004

Awawdeh, M., Obeidat, M., Al-Mohammad, M., Al-Qudah, K., Jaradat, R., 2014. Integrated GIS and remote sensing for mapping groundwater potentiality in the Tulul al Ashaqif, Northeast Jordan. Arab. J. Geosci. 7, 2377–2392. https://doi.org/10.1007/s12517-013-0964-8

Azizur, M., Rusteberg, B., Salah, M., Lutz, A., 2013. An integrated study of spatial multicriteria analysis and mathematical modelling for managed aquifer recharge site suitability mapping and site ranking at Northern Gaza coastal aquifer. J. Environ. Manage. 124, 25–39. https://doi.org/10.1016/j.jenvman.2013.03.023

Bauman, P.D., Woods, L., Miazga, C., Layton, M., 2018. Community Groundwater Supply Development in Acholiland, Northern Uganda.

Belfiore, O.R., Meneghini, C., Parente, C., Santamaria, R., 2016. Application of different pan-sharpening methods on Worldview-3 images. ARPN J. Eng. Appl. Sci. 11, 490–496.

BGS, 2017. Hydrogeology of Uganda. Earthwise Africa Groundw. Atlas.

Blom, R.G., Crippen, R.E., Elachi, C., 1984. Detection of subsurface features in Seasat radar images of Means Valley, Mojave Desert, California. Geology 12, 346–349. https://doi.org/10.1130/0091-7613(1984)12<346:DOSFIS>2.0.CO;2

Brunner, P., Hendricks Franssen, H.J., Kgotlhang, L., Bauer-Gottwein, P., Kinzelbach, W., 2007. How can remote sensing contribute in groundwater modeling? Hydrogeol. J. 15, 5–18. https://doi.org/10.1007/s10040-006-0127-z

Chabot, D., Dillon, C., Shemrock, A., Weissflog, N., Sager, E.P.S., 2018. An Object-Based Image Analysis Workflow for Monitoring Shallow-Water Aquatic Vegetation in Multispectral Drone Imagery. Int. J. Geo-Information. https://doi.org/10.3390/ijgi7080294

Ciampalini, A., Raspini, F., Frodella, W., Bardi, F., Bianchini, S., Moretti, S., 2016. The effectiveness of high-resolution LiDAR data combined with PSInSAR data in landslide study. Landslides 399–410. https://doi.org/10.1007/s10346-015-0663-5

Demek, J., 1972. Manual of detailed geomorphological mapping. Academia, Prague.

Devi, M.B., Devanathan, R., 2019. Pansharpening of Remote Sensing Data of Earth Satellite Images. Procedia 6, 353–363.

Dhany, A., Muttil, N., Gokhan, A., Perera, B.J.C., 2017. Using the Analytic Hierarchy Process to identify parameter weights for developing a water quality index. Ecol. Indic. 75, 220–233. https://doi.org/10.1016/j.ecolind.2016.12.043

Dubey, B., Kartikeyan, B., Subbiah, M.M., 2018. Rational Polynomial Coefficients Modeling and Bias Correction by Using Iterative Polynomial Augmentation. J. Indian Soc. Remote Sens. 0123456789. https://doi.org/10.1007/s12524-018-0883

Durbach, I., Lahdelma, R., Salminen, P., 2014. The analytic hierarchy process with stochastic judgements. Eur. J. Oper. Res. 238, 552–559. https://doi.org/10.1016/j.ejor.2014.03.045

Elbeih, S.F., 2014. An overview of integrated remote sensing and GIS for groundwater mapping in Egypt. Ain Shams Eng. J. 6, 1–15. https://doi.org/10.1016/j.asej.2014.08.008

Escobar, D., Ayuga, F., Arnold, D., Wermuth, M., Ferna, J., 2017. ScienceDirect Sentinel-1A – First precise orbit determination results. Adv. Sp. Res. 60, 879–892. https://doi.org/10.1016/j.asr.2017.05.034

FAO, 2017. Mineral soils conditioned by a Wet (Sub) Tropical Climate [WWW Document]. URL http://www.fao.org/docrep/003/y1899e/y1899e08a.htm (accessed 1.1.17).

FAO, 1997. Soil Map of the World. Rome.

Farahbakhsh, E., Chandra, R., Olierook, H.K.H., Scalzo, R., Clark, C., Reddy, S.M., Müller, R.D., Farahbakhsh, E., Chandra, R., Olierook, H.K.H., Scalzo, R., Clark, C., Reddy, S.M., Müller, R.D., 2020. Computer vision-based framework for extracting tectonic lineaments from optical remote sensing data. Int. J. Remote Sens. 41, 1760–1787. https://doi.org/10.1080/01431161.2019.1674462

Fenta, A.A., Kifle, A., Gebreyohannes, T., Hailu, G., 2014. Spatial analysis of groundwater potential using remote sensing and GIS-based multi-criteria evaluation in Raya Valley, northern Ethiopia . Hydrogeol. J. 23, 195–206. https://doi.org/10.1007/s10040-014-1198-x

Frost, V.S., Member, S., Stiles, J.A., Member, S., 1982. A Model for Radar Images and Its Application to Adaptive Digital Filtering of Multiplicative Noise. IEEE Trans. Pattern Anal. Mach. Intell. 8, 231–239.

Gaber, A., Koch, M., Griesh, M.H., Sato, M., 2011. SAR remote sensing of buried faults: Implications for groundwater exploration in the western desert of Egypt. Sens. Imaging 12, 133–151. https://doi.org/10.1007/s11220-011-0066-1

Ghassemian, H., 2016. A review of remote sensing image fusion methods. Inf. Fusion 32, 75–89. https://doi.org/10.1016/j.inffus.2016.03.003

Ghayoumian, J., Saravi, M.M., 2007. Application of GIS techniques to determine areas most suitable for artificial groundwater recharge in a coastal aquifer in southern Iran 30, 364–374. https://doi.org/10.1016/j.jseaes.2006.11.002

Gil, J.J., 2014. Interpretation of the coherency matrix for three-dimensional polarization states. Phys. Rev. A 90.

Glenn, N.F., Streutker, D.R., Chadwick, D.J., Thackray, G.D., Dorsch, S.J., 2006. Analysis of LiDAR-derived topographic information for characterizing and differentiating landslide morphology and activity. Geomorphology 73, 131–148. https://doi.org/10.1016/j.geomorph.2005.07.006

Gomes, L., Rocha, D.M., César, A., Pires, B., Carmelo, A.C., Oswaldo, J., Filho, D.A., 2014. Geophysical characterization of the Azimuth 125 ◦ lineament with aeromagnetic data : Contributions to the geology of central Brazil. Precambrian Res. 249, 273–287. https://doi.org/10.1016/j.precamres.2014.05.005

GWB, 2018. Community Groundwater Supply Development in Acholiland , Northern Uganda. Calgary, AB.

Hall, J., 1986. Geophysical Lineaments and Deep Continental Structure. Philos. Trans. R. Soc. London 317, 33–44.

Hall, M., Diggens, J., 2011. The East African Rift System - A view from space. Geo Expro Mag. Vol 8., 96.

Hengl, T., Jesus, J.M. De, Heuvelink, G.B.M., Ruiperez, M., Kilibarda, M., Blagoti, A., Shangguan, W., Wright, M.N., Geng, X., Bauer-marschallinger, B., Guevara, M.A., Vargas, R., Macmillan, R.A., Batjes, N.H., Leenaars, J.G.B., Ribeiro, E., Wheeler, I., Mantel, S., Kempen, B., 2017. SoilGrids250m : Global gridded soil information based on machine learning. PLoS One 1–41. https://doi.org/10.1371/journal.pone.0169748

Henrique, P., Santos, D., Miranda, S., Ornaghi, D., Anna, S., Henrique, C., Oliveira, D., Duarte, H., 2019. The analytic hierarchy process supporting decision making for sustainable development : An overview of applications. J. Clean. Prod. 212, 119–138. https://doi.org/10.1016/j.jclepro.2018.11.270

Katumwehe, A.B., Abdelsalam, M.G., Atekwana, E.A., Laó-Dávila, D.A., 2016. Extent, kinematics and tectonic origin of the Precambrian Aswa Shear Zone in eastern Africa. Gondwana Res. 34, 241–253. https://doi.org/10.1016/j.gr.2015.03.007

Kim, Y., van Zyl, J.J., 2009. A Time-Series Approach to Estimate Soil Moisture Using Polarimetric Radar Data. Geosci. Remote Sensing, IEEE Trans. 47, 2519–2527. https://doi.org/10.1109/TGRS.2009.2014944

Kupidura, P., 2016. Comparison of filters dedicated to speckle suppression in SAR Images. Int. Arch. Photogramm. Remote Sens. Spat. Inf. Sci. XLI, 12–19. https://doi.org/10.5194/isprsarchives-XLI-B7-269-2016

Lasaponara, R., Masini, N., 2013. Satellite synthetic aperture radar in archaeology and cultural landscape: An overview. Archaeol. Prospect. 20, 71–78. https://doi.org/10.1002/arp.1452

Laurencelle, J., Logan, T., Gens, R., 2015. ASF Radiometrically Terrain Corrected ALOS PALSAR products Product guide (No. 1.2). ASF Engineering.

Lee, J., Fellow, L., Ainsworth, T.L., Member, S., 2011. The Effect of Orientation Angle Compensation on Coherency Matrix and Polarimetric Target Decompositions. IEEE Trans. Geosci. Remote Sens. 49, 53–64. https://doi.org/10.1109/TGRS.2010.2048333

Lee, S., Kim, Y.S., Oh, H.J., 2012. Application of a weights-of-evidence method and GIS to regional groundwater productivity potential mapping. J. Environ. Manage. 96, 91–105. https://doi.org/10.1016/j.jenvman.2011.09.016

Li, X., 2001. Tutorial Ellipsoid , geoid , gravity , geodesy , and geophysics 66, 1660–1668.

Luo, Q., Hu, M., Zhao, Z., Li, J., Zeng, Z., 2020. Design and experiments of X-type artificial control targets for a UAV-LiDAR system. Int. J. Remote Sens. 41, 3307–3321. https://doi.org/10.1080/01431161.2019.1701210

Macdonald, A.M., Davies, J., 2000a. A brief review of groundwater for rural water supply in sub-Saharan. Br. Geol. Surv. Tech. Rep. WC/00/33 13. https://doi.org/WC/00/33

Macdonald, A.M., Davies, J., 2000b. A brief review of groundwater for rural water supply in sub-Saharan Africa. Br. Geol. Surv. Tech. Rep. WC/00/33 13. https://doi.org/WC/00/33

Mahyoub, S., Fadil, A., Mansour, E.M., Rhinane, H., Al-nahmi, F., 2019. Fusing of optical and synthetic aperture radar (SAR) remote sensing data: a systematic literature review (SLR). Int. Arch. Photogramm. Remote Sens. Spat. Inf. Sci. XLII, 10–11

Meyer, F.J., Nicoll, J.B., 2008. Prediction , Detection , and Correction of Faraday Rotation in Full-Polarimetric L-Band SAR Data. IEEE Trans. Geosci. Remote Sens. 46, 3076–3086. https://doi.org/10.1109/TGRS.2008.2003002

Milas, A.S., Warner, T.A., Younan, N.H., Balenovic, I., Larson, M.D., Simic, A., Warner, T.A., Younan, N.H., Balenovic, I., 2019. Preface for the Special Issue of IJRS Drones section in conjunction with the 6th UAS4Enviro conference Preface for the Special Issue of IJRS Drones section in. Int. J. Remote Sens. 40, 9065–9069. https://doi.org/10.1080/01431161.2019.1658409

Mutiti, S., Levy, J., Mutiti, C., Gaturu, N.S., 2010. Assessing ground water development potential using Landsat imagery. Ground Water 48, 295–305. https://doi.org/10.1111/j.1745-6584.2008.00524.x

Noureldin, A., Karamat, T.B., Georgy, J., 2013. Fundamentals of inertial navigation, satellite-based positioning and their integration, Fundamentals of Inertial Navigation, Satellite-Based Positioning and their Integration. https://doi.org/10.1007/978-3-642-30466-8

Olierook, H.K.H., Scalzo, R., Kohn, D., Chandra, R., Farahbakhsh, E., Houseman, G., Clark, C., Reddy, S.M., Müller, R.D., 2019. Bayesian geological and geophysical data fusion for the construction and uncertainty quantification of 3D geological models. Solid Earth Discuss. 1–34.

Oyawale, A.A., Adeoti, F.O., Ajayi, T.R., Omitogun, A.A., 2020. Applications of remote sensing and geographic information system (GIS) in regional lineament mapping and structural analysis in Ikare Area , Southwestern Nigeria. J. Geol. Min. Res. 12, 13–24. https://doi.org/10.5897/JGMR2019.0310

Pan, Y., Ren, C., Liang, Y., Zhang, Z., Shi, Y., 2020. Inversion of surface vegetation water content based on GNSS - IR and MODIS data fusion. Satell. Navig. 1–15. https://doi.org/10.1186/s43020-020-00021-z

Pavez, A., Remy, D., Bonvalot, S., Diament, M., Gabalda, G., Froger, J., 2006. Insight into ground deformations at Lascar volcano (Chile) from SAR interferometry , photogrammetry and GPS data : Implications on volcano dynamics and future space monitoring. Remote Sens. Environ. 100, 307–320. https://doi.org/10.1016/j.rse.2005.10.013

Pavlic, G., Singhroy, V., Duk-Rodkin, A., Alasset, P., 2008. Satellite data fusion techniques for terrain and surficial geological mapping, in: IEEE IGARSS. pp. 314–317. https://doi.org/10.1109/IGARSS.2008.4779346

Rahmati, O., Haghizadeh, A., Stefanidis, S., 2016. Assessing the Accuracy of GIS-Based Analytical Hierarchy Process for Watershed Prioritization ; Gorganrood River 1131–1150. https://doi.org/10.1007/s11269-015-1215-4

Rahnama, M., Gloaguen, R., 2014. TecLines: A MATLAB-Based Toolbox for Tectonic Lineament Analysis from Satellite Images and DEMs, Part 1: Line Segment Detection and Extraction. Remote Sens. 5938–5958. https://doi.org/10.3390/rs6075938

Republic of Uganda, 2019. Airborne Geophysical Digital Data Dissemination Policy.

Reynolds, J.M., 1997. An Introduction to Applied and Environmental Geophysics. John Wiley & Sons Ltd.

Robins, N.S., Davies, J., Farr, J.L., Calow, R.C., 2006. The changing role of hydrogeology in semi-arid southern and eastern Africa. Hydrogeol. J. 14, 1483–1492. https://doi.org/10.1007/s10040-006-0056-x

Rott, H., 1984. The Analysis of Backscattering Properties from SAR Data of Mountain Regions. IEEE J. Ocean. Eng. 9, 347–355. https://doi.org/10.1109/JOE.1984.1145655

Russo, T.A., Fisher, A.T., Lockwood, B.S., 2015. Assessment of Managed Aquifer Recharge Site Suitability Using a GIS and Modeling 53, 389–400. https://doi.org/10.1111/gwat.12213

Saalmann, K., Mänttäri, I., Nyakecho, C., Isabirye, E., 2016. Age, tectonic evolution and origin of the Aswa Shear Zone in Uganda: Activation of an oblique ramp during convergence in the East African Orogen. J. African Earth Sci. 117, 303–330. https://doi.org/10.1016/j.jafrearsci.2016.02.002

Saaty, T.L., 1994. How To Make A Decision : The Analytic Hierarchy Process 75–105.

Salem, A., Fairhead, J., Ravat, D., Smith, R., 2007. Tilt-depth method : A simple depth estimation method using first-order magnetic derivatives. Lead. Edge 3–6.

Sandoval, J.A., Tiburan, C.L., 2019. Identification of potential artificial groundwater recharge sites in Mount Makiling Forest Reserve , Philippines using GIS and Analytical Hierarchy Process. Appl. Geogr. 105, 73–85. https://doi.org/10.1016/j.apgeog.2019.01.010

Senanayake, I.P., Dissanayake, D.M.D.O.K., Mayadunna, B.B., Weerasekera, W.L., 2016. An approach to delineate groundwater recharge potential sites in Ambalantota, Sri Lanka using GIS techniques. Geosci. Front. 7, 115–124. https://doi.org/10.1016/j.gsf.2015.03.002

Sener, E., Davraz, A., 2013. Assessment of groundwater vulnerability based on a modified DRASTIC model , GIS and an analytic hierarchy process (AHP) method: the case of Egirdir Lake basin (Isparta , Turkey). Hydrogeol. J. 701–714. https://doi.org/10.1007/s10040-012-0947-y

Shahdoosti, H.R., Ghassemian, H., 2016. Combining the spectral PCA and spatial PCA fusion methods by an optimal filter. Inf. Fusion 27, 150–160. https://doi.org/10.1016/j.inffus.2015.06.006

Sloots, R., 2010. Ministry of Water and Environment Assessment of Groundwater Investigations and Borehole Drilling Capacity in Uganda.

Small, D., 2011. Flattening Gamma : Radiometric Terrain Correction for SAR Imagery. IEEE Trans. Geosci. Remote Sens. 49, 3081–3093.

Srivastava, H.S., Patel, P., Navalgund, R.R., 2006. How far SAR has fulfilled its expectation for soil moisture retrieval. Microw. Remote Sens. Atmos. Environ. 6410, 641001. https://doi.org/10.1117/12.693946

Strozzi, T., Delaloye, R., Kääb, A., Ambrosi, C., Perruchoud, E., 2010. Combined observations of rock mass movements using satellite SAR interferometry , differential GPS , airborne digital photogrammetry , and airborne photography interpretation. J. Geophys. Res. 115, 1–12. https://doi.org/10.1029/2009JF001311

Tagnon, B.O., 2016. Statistical and Geostatistical Analysis of Lineaments Network Mapped in The Precambrian Basement : Case of Divo-Oume Region (Southern Cote d ' Ivoire). Eur. Sci. J. 12, 299–318. https://doi.org/10.19044/esj.2016.v12n33p299

Thannoun, R.G., 2013. Automatic Extraction and Geospatial Analysis of Lineaments and their Tectonic Significance in some areas of Northern Iraq using Remote Sensing Techniques and GIS. Int. J. Enhanc. Reseaarch Sci. Technol. Eng. 2, 1–11.

Tsiko, R.G., Haile, T.S., 2011. Integrating Geographical Information Systems, Fuzzy Logic and Analytical Hierarchy Process in Modelling Optimum Sites for Locating Water Reservoirs. A Case Study of the Debub District in Eritrea. Water 254–290. https://doi.org/10.3390/w3010254

Turkar, V., Bombay, I.I.T., 2011. Applying Coherent and Incoherent Target Decomposition Techniques to Polarimetric SAR Data 23–29.

UNDP, WHO, WFP, Uganda, R. of, Project, N.U.E.R., 2013. Rays of Hope in Lango Sub-Region, Northern Uganda.

Van Zyl, Jakob; Kim, Y., 2011. Synthetic Aperture Radar Polarimetry. John Wiley & Sons, Inc.

Vasuki, Y., Holden, E., Kovesi, P., Micklethwaite, S., 2014. Semi-automatic mapping of geological structures using UAV-based photogrammetric data : An image analysis approach. Comput. Geosci. 69, 22–32. https://doi.org/10.1016/j.cageo.2014.04.012

Vijayaraj, V., Younan, N.H., Hara, C.G.O., 2006. Concepts of Image Fusion in Remote Sensing Applications, in: 2006 IEEE International Symposium on Geoscience and Remote Sensing. pp. 3781–3784. https://doi.org/10.1109/IGARSS.2006.973

Wald, L., Ranchin, T., Mangolini, M., Wald, L., Ranchin, T., Mangolini, M., 2009. Fusion of satellite images of different spatial resolutions : Assessing the quality of resulting images To cite this version : HAL Id : hal-00365304.

Walker, P.J.P., 2013. Basis of an Australian Radar Soil Moisture Algorithm Theoretical Baseline Document (ATBD).

Wang, Xiaofei, Wang, Xiaoyi, 2020. Spatiotemporal Fusion of Remote Sensing Image Based on Deep Learning. J. Sensors 2020.

Xu, G., Xu, Y., 2016. GPS: Theory, algorithms and applications, third edition. GPS Theory, Algorithms Appl. Third Ed. 1–489. https://doi.org/10.1007/978-3-662-50367-6

Xu, W., Lan, Y., Li, Y., Luo, Y., He, Z., 2019. Classification method of cultivated land based on UAV visible light remote sensing. Int. J. Agric. Biol. Eng. 12, 103–109. https://doi.org/10.25165/j.ijabe.20191203.4754

Yeomans, C.M., Middleton, M., Shail, R.K., Grebby, S., Lusty, P.A.J., 2019. Integrated Object-Based Image Analysis for semi-automated geological lineament detection in southwest England. Comput. Geosci. 123, 137–148. https://doi.org/10.1016/j.cageo.2018.11.005

Zeng, T., Yin, W., Ding, Z., Long, T., 2016. Motion and Doppler Characteristics Analysis Based on Circular Motion Model in Geosynchronous SAR. IEEE J. Sel. Top. Appl. Earth Obs. Remote Sens. 9, 1132–1142. https://doi.org/10.1109/JSTARS.2015.2429915

Zhang, X., Tang, X., Gao, X., Zhao, H., 2018. Multitemporal Soil Moisture Retrieval over Bare Agricultural Areas by Means of Alpha Model with Multisensor SAR Data. Adv. Meteorol. 2018, 17.

Zhu, X.X., Member, S., Montazeri, S., Gisinger, C., Hanssen, R.F., Member, S., Bamler, R., 2016. Geodetic SAR Tomography. IEEE Trans. Geosci. Remote Sens. 54, 18–35. https://doi.org/10.1109/TGRS.2015.2448686

Zyl, J.J. Van, Arii, M., Kim, Y., Member, S., 2011. Model-Based Decomposition of Polarimetric SAR Covariance Matrices Constrained for Nonnegative Eigenvalues. IEEE Trans. Geosci. Remote Sens. 49, 3452–3459.

III. GROUNDWATER POTENTIALITY MODEL OF GULU DISTRICT, UGANDA USING GIS AND REMOTE SENSING WITH THE ANALYTICAL HIERARCHY PROCESS (AHP) METHOD

Rachel Jones

Deparment of Geological Engineering, Missouri University of Science and Technology, Rolla, MO 65409

ABSTRACT

GIS and remote sensing have been increasingly used to model groundwater potentiality in developing countries due to scarcity of ground-based data. Gulu District, Uganda has few technological resources to acquire ground-based data, thus GIS and remote sensing are necessary to develop models for the location of groundwater resources. An analytical hierarchy process (AHP) has been applied to various GIS derived and remotely sensed datasets to investigate optimal borehole drilling locations. Precipitation, soils, lithology, drainage and lineament densities, land cover, and slope of the 3,899 km^2 area of interest (AOI) were weighted according to the AHP method and processed with the hydrologic model algorithm. The results of the groundwater potentiality model of Gulu District estimates that 0.3% of the district has poor groundwater potentiality, 37% of the area has fair groundwater potentiality, 51% of the district has good groundwater potentiality, and 11.7% of the area has very good potential for groundwater resources.

1. INTRODUCTION

Water use is at historically high levels in developed countries where population centers are increasingly exhausting established aquifer systems (Senanayake et al., 2016). These populations often struggle with the overuse or misuse of water. Conversely, sustainable groundwater programs in developing countries are often nonexistent or boreholes for water wells are drilled at the point of need rather than at optimal locations for long term sustainability (Macdonald and Davies, 2000; Sloots, 2010). Lack of hydrogeological data compounds this problem where progress is slow for disadvantaged populations in developing countries (Robins et al., 2006).

The absence of technological resources and difficulty in accessing remote areas in developing countries restrict broader applications of ground-based hydrogeological data for groundwater resource exploration. Additionally, the development of new groundwater resources often occur in crisis and disaster situations. These events present significant hazards to groundwater development investigations that require the transportation and use of geophysical equipment. Remote sensing (RS) and geospatial information systems (GIS) methods are valuable alternative tools to conduct hydrogeological investigations in developing countries where ground-based investigations are typically hazardous. GIS methods facilitate a cartographic means of visualizing geographic data simultaneous with hydrological data to integrate various thematic maps (Ghayoumian and Saravi, 2007; Mutiti et al., 2010). Remote sensing of earth's resources using satellite and airborne data provides measurements of terrain that would otherwise be inaccessible or cost prohibitive to scientists. Anthropogenic concerns such as sanitation, hygiene, and food security in

developing countries increase the urgency to establish groundwater exploration programs (UNDP et al., 2013). Therefore, groundwater resource exploration programs in developing countries face the dual problem of critical need paired with lack of information.

Model-based groundwater potentiality assessments using various datasets including geological maps, precipitation data, soil maps, and slope have been increasingly used for remote groundwater investigations (Awawdeh et al., 2014; Elbeih, 2014; Lee et al., 2012; Sandoval and Tiburan, 2019). These assessments utilize various thematic maps for weight-based multi-criteria analysis (Azizur et al., 2013; Fenta et al., 2014). Specifically, the Analytic Hierarchy Process (AHP) has been proven as a reliable method to evaluate a selection of datasets and establish a weight-based system through a decision matrix (Rahmati et al., 2016). Hydrogeological datasets for developing countries is sparse, but the AHP method provides the capability of evaluating available data for the most optimal result. While there are other methods of multicriteria decision making analysis (e.g. fuzzy theory, technique for order preference by similarity to ideal solution (TOPSIS), etc.) the AHP method is a frequently used method for decision analysis (Henrique et al., 2019; Jesiya and Gopinath, 2019; Tsiko and Haile, 2011).

The goal of this study is to apply the AHP method to available hydrogeological data to assemble a groundwater potentiality map for Gulu District of Uganda. This map can help future development of groundwater boreholes. The specific objectives are to 1) characterize the AHP inputs, 2) develop the groundwater potentially map, and 3) benchmark the map using available electrical resistivity tomography (ERT) data and well logs.

2. MATERIALS AND METHODS

2.1. CHARACTERIZATION OF GULU DISTRICT, UGANDA

Gulu District is located in northern Uganda, within Sub-Saharan Africa and the East African Rift System (EARS) (Figure 1). EARS is an active, continental tectonic system where the Somali and Nubian plates diverge and shear (Hall and Diggens, 2011). Gulu District is located on the Nubian plate in the Aswa Shear Zone (ASZ) of the EARS. The ASZ trends NW-SE from southwestern South Sudan, through Uganda, and ends in western Kenya for a length of over 1,000 km (Saalmann et al., 2016). Numerous fractures exist within the ASZ and are a major contributor to the groundwater flow regime in Gulu District (Gaber et al., 2011). Fissures in the Precambrian basement complex contribute to high permeability as a function of the distribution and number of fractures. These fractures are conduits for fluid flow within the groundwater aquifer regime which is leaky and semi-confined.

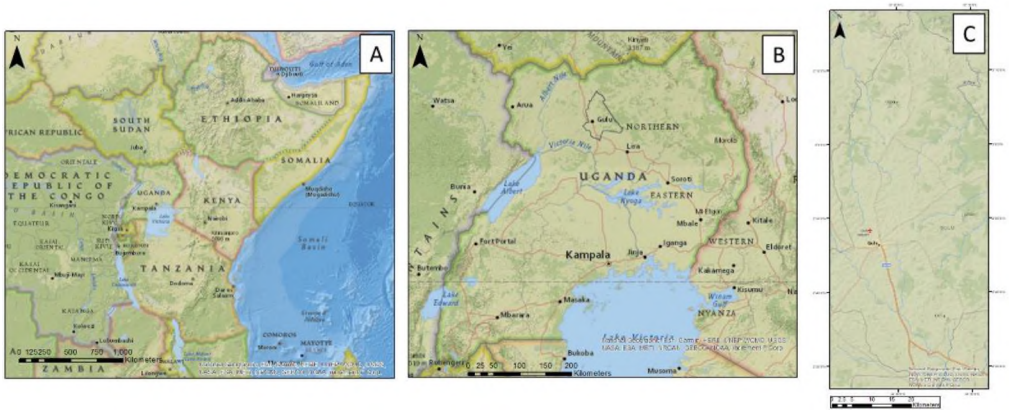

Figure 1. Area of interest. A) East Central Africa. B) Uganda. C) Gulu District, Uganda.

The headwaters of the White Nile originate in southern Uganda in Lake Victoria. The stream is considered the Victorian Nile as it travels north from Lake Victoria, through Lake Kyoga in central Uganda, and then west to Lake Albert where the name changes to the White Nile. The White Nile travels north along the border of Uganda and the Democratic Republic of Congo (DRC) and through South Sudan and Sudan where it reaches its ultimate confluence with the Nile in Khartoum, Sudan.

Dendritic stream networks dominate Gulu District as the main surface water resource. Three rivers flow from Gulu District. The Tochi River in the south flows south to the Victorian Nile. The Achwa river flows north-northwest to the White Nile in South Sudan. The Unyama River flows northeast to its confluence with the White Nile at the border of Uganda and South Sudan.

The northern Uganda Precambrian mobile/orogenic belt has an Archean-Plutonic granulite composition with granitoid rocks, gneisses, and mafic volcanic intrusions (Survey, 2017). Soils within the study area are common in sub-tropical regions and consist mainly of acrisols, and ferralsols. Ferralsols have good permeability and porosity, low soil pH, and geomorphologic stability. They are clayey and are characterized by advanced weathering. The clay content is kaolinitic and, thus, is favorable to good drainage and aquifer recharge rates (FAO, 2017). Acrisols are located in the undulating topographies of sub-tropical regions where intense weatherization has occurred. They have a porous soil structure, low pH, and are found under forest canopies. Nitisols result from the erosion of basic to intermediate parent rocks found in savannah vegetation profiles and in tropical rainforests.

2.2. WORKFLOW FOR MAP DEVELOPMENT

The workflow for the development of a groundwater potentiality map consisted of 1) data collection, 2) GIS processing, 3) layer operations, and 4) a weighted overlay (Figure 2). Data collection included precipitation data, a SRTM DEM for the study area, soils data, a Land Use / Land Cover Map, and a geologic map of the area of interest. The data collected were used to derive a precipitation map, drainage density, slope map, lineament density, and lithology for the area. All datasets were reclassed into five divisions for the final model. Layer operations included assigning AHP weights to each factor within the model and assign values to the reclassified divisions of data. A weighted overlay model was performed and groundwater potentiality maps were produced.

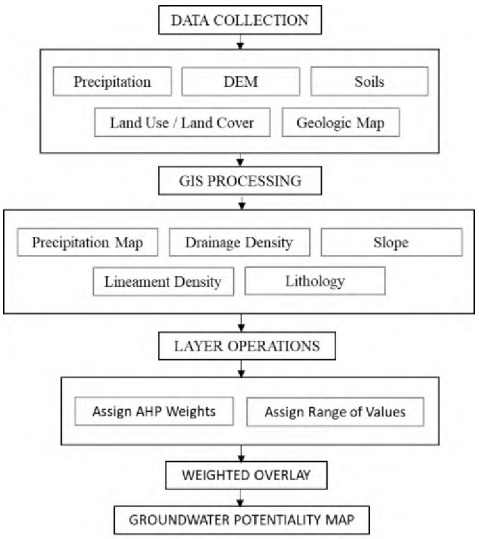

Figure 2. Workflow for groundwater potentiality map development.

2.3. THEMATIC INPUT LAYERS

Thematic maps were selected according to their relevance to groundwater potentiality, quality of data, and availability of data and include precipitation, drainage density, land cover, soil taxononmy, lineament density, slope, and lithology (Figure 3). Several layers are derivatives from base data, such as using digital elevation models to derive slope. These derivatives were processed using ArcGIS (v. 10.7, ESRI, Inc.) with details described below.

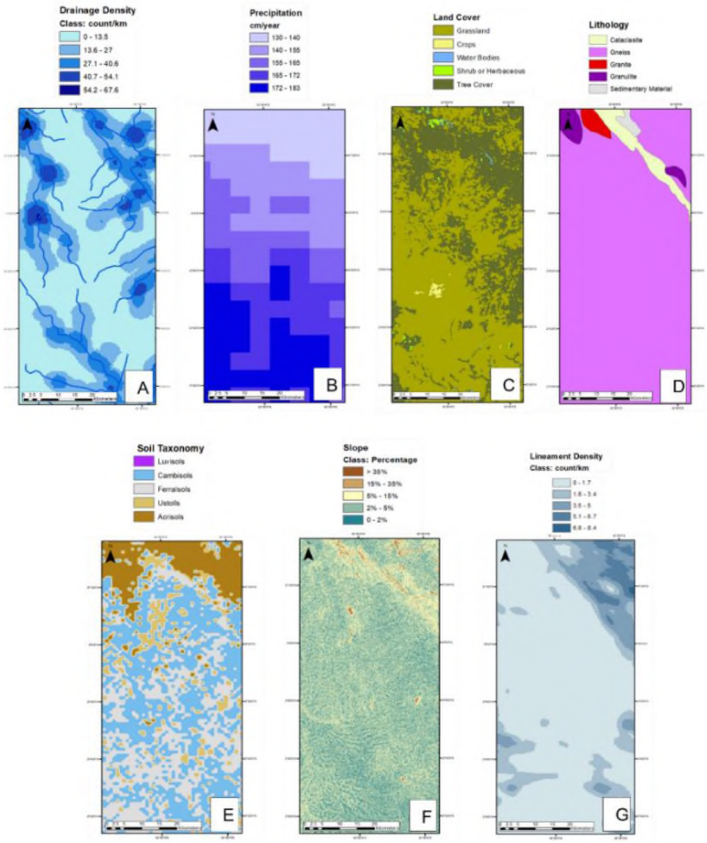

Figure 3. Thematic maps used for groundwater potentiality model. A) Drainage Density. B) Precipitation. C) Land Cover. D) Lithology. E) Soil Taxonomy. F) Percent slope. G) Lineament Density.

The drainage density of a stream network is a necessary factor to determine groundwater potentiality. The total length of stream channels within a basin is divided by the area of the basin to determine drainage density. It is a means of determining the capability of a stream network to distribute streamflow and identify locations of concentrated flow. High drainage density indicates areas of high streamflow and less recharge to the groundwater system. Lower drainage density indicates slower runoff velocities and a greater potential for surface infiltration. The drainage density for the study area (Figure 3A) was calculated using ArcGIS (v. 10.7, ESRI, Inc.). Watersheds were delineated by using the SRTM DEM to calculate streamflow direction and accumulation. Pour points were designated along the stream channels then the ArcGIS Watershed Delineation tool was used. This product was used to calculate the basin areas within the study area. Stream lengths were calculated using the calculate geometry tool and a final drainage density map was produced by dividing the length of the stream channels by the basin areas.

The UN Food and Agriculture Organization (FAO) provides on online database Water Productivity Open-access Portal using Remote sensing technologies (WaPOR) to monitor water productivity through remotely sensed data and derived data. Precipitation data was accessed through the UN FAO WaPOR (https://wapor.apps.fao.org). The dataset sourced from the Climate Hazards Group InfraRed Precipitation with Station (CHIRPS) version 2.0 global rainfall dataset with an approximately 5 km (0.05 degree) resolution and was classified into five categories (Figure 3B). Annual precipitation data for the year 2019 was used and is expressed as average daily precipitation.

Land cover data is made available by the UN Food and Agriculture Organization's (FAO) WaPOR portal. The dataset is based on the Copernicus Global Land cover map (v. 2.0.2), the Earth Observation program of the European Commission, and is published annually. The Land Cover Classification System (LCCS) applied to the map was developed by the FAO. The dataset was reclassified to five categories consisting of grassland, crops, water bodies, flooded shrub or herbaceous cover, and tree cover (Figure 3C).

The lithologic map was accessed through the Uganda Directorate of Geological Survey of Mines' Geoscience Data Portal which is available online for public access (http://ugandageosciencedataportal.minerals.go.ug). The portal was created as part of the African Resource Geoscience Initiative (ARGI) and makes available various geophysical data products. The geological map (Saalmann et al., 2016) was accessed as a .tif file and vectorized (Figure 3D).

The World Reference Base (WRB) for Soil Resources is an international soil classification standard developed by the International Soil Reference and Information Centre (ISRIC) and endorsed by the International Union of Soil Sciences (IUSS). The WRB relies heavily on the USDA soil classification standards and is based on soil morphology. The diagnostic criteria for soil classification in the WRB correlate to the USDA system as well as other international systems (FAO, 1997). Accuracy assessments of the WRB system have been performed and the correspondence between the WRB and USDA classification systems are relatively high (Hengl et al., 2017).

Soil data for the study area was made available by the International Soil Reference and Information Centre's (ISRIC) SoilGrid database (https://soilgrids.org). SoilGrids uses

machine learning to map the distribution of soil properties according to spatial criteria. Global data is available at a spatial resolution of 250 meters. Local and regional soil maps are not electronically accessible for the subject area therefore the SoilGrid database is the most reliable and highest resolution data available. The soil was classified according to five categories: ferralsols, acrisols, ustolls, cambisols, and luvisols (Figure 3E).

Slopes were derived from the Shuttle Radar Topography Mission (SRTM) digital elevation model (DEM) surface slope algorithm (Figure 3F). The resulting slope map was then classified into five groups according to established geomorphological percent slope divisions (Demek, 1972). Infiltration rates of surface runoff are greater for gentler slopes because surface flow has a lower velocity and, thus, more time to penetrate soils. Conversely, areas with steeper slopes are less ideal for surface flow infiltration.

Surface expressions of fractures within the ASZ were delineated and a lineament density map was produced. The initial lineament map was produced by fusing Alos Palsar synthetic aperture radar (SAR) data with magnetometry data acquired by the Uganda Directorate of Survey and Mines (DGSM) (Jones, 2021). The length of the lineaments of the fracture network were divided by the total area of the region to develop the lineament density map (Figure 3G).

Additional lineament density maps were produced to investigate the benefits of other data products on the final Groundwater Potentiality Map. (Figure 4) Lineaments were extracted and lineament density maps were produced from SRTM DEM (Figure 4A) and various DGSM magnetic datasets including magnetic analytic signal (Figure 4B), magnetic first vertical derivative (Figure 4C), and the magnetic horizontal gradient (Figure 4D).

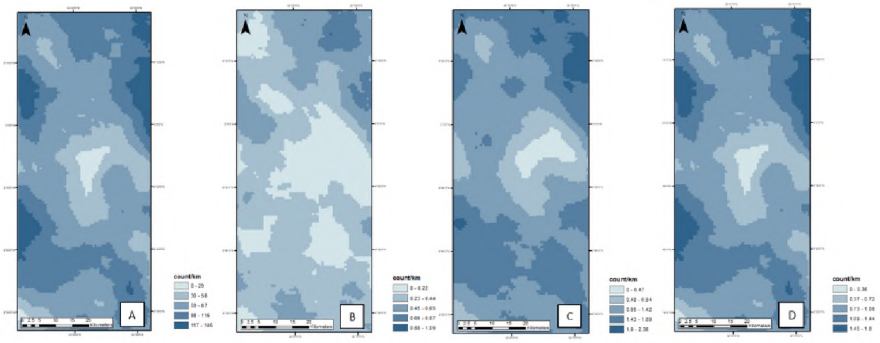

Figure 4. Lineament density maps used for variations of the Groundwater Potentiality Model. A) SRTM DEM. B) Magnetic analytic signal. C) Magnetic first vertical derivative. D) Magnetic horizontal gradient.

2.4. ANALYTIC HIERARCHY PROCESS (AHP)

A weighted overlay method was used to classify thematic maps based on a multi-criteria AHP weighted analysis (Figure 2) using ArcGIS (v. 10.7, ESRI, Inc.). The AHP is an arithmetic method of deriving weights for multiple criteria within a decision matrix (Saaty, 1994). The AHP method uses numbers to calculate the priority of variables within the hierarchy for the goal of structuring a conclusion based on objective criteria. Thus, qualitative elements of a hierarchy of criteria are transformed into a quantitative method of judgment. The result is that each element of the hierarchical process is given a weight by which to evaluate the final result (Fenta et al., 2014). This technique is practical because it considers the effect of each element on other elements within each level of the hierarchy.

Seven thematic maps have been used to produce a groundwater potentiality map. These maps are: precipitation, soil, lithology, drainage density, lineament density, land use / land cover, and the slope. A 9 point semantic scale (Durbach et al., 2014) is used to construct a pairwise comparison according to the AHP method (Tsiko and Haile, 2011). The AHP pairwise comparison is located in Table 1. Elements with greater importance are

given a value of 1 while elements of lesser importance are given a value of 9. The level of importance for each element was determined by evaluating criteria used in similar research for groundwater potentiality mapping (Ahmad and Verma, 2018; Dhany et al., 2017; Sandoval and Tiburan, 2019; Sener and Davraz, 2013; Tsiko and Haile, 2011). Elements with equal importance are assigned the same values. The total preparatory factors were calculated to establish the factor of weights for the next step.

Table 1. Analytic Hierarchy Process (AHP) pairwise comparison.

Pairwise Comparison							
	Precipitation	Drainage Density	Lineament Density	Slope	Land Use / Land Cover	Soil	Lithology
Precipitation	1	3	3	5	5	7	9
Drainage Density	1/3	1	1	3	5	7	7
Lineament Density	1/3	1	1	3	5	5	5
Slope	1/5	1/3	1/3	1	3	3	5
Land Use / Land Cover	1/5	1/5	1/5	1/3	1	1	3
Soil	1/7	1/7	1/5	1/3	1	1	3
Lithology	1/9	1/7	1/5	1/5	1/3	1/3	1
Total	2.32	5.82	5.93	12.87	20.33	24.33	33.00

The total factor of weights from Table 1 are used to evaluate the final weights for the groundwater potentiality model (Table 2). The preparatory factor is divided by the total factor for each column in Table 1 to establish the factor of weights in Table 2. This factor of weight is then averaged in comparison to the remaining hierarchical elements to establish a final mean weight expressed as a percentage. Each element of the hierarchy is further divided by classification into 5 categories of very low, low, moderate, high, and

very high according to the element's influence on groundwater potentiality (Table 3). The final weight for each category of classification is the effectiveness and is determined by multiplying the rating value and the weight.

Table 2. AHP final weights calculated from the pairwise comparison.

Final Weights								
	Precipitation	Drainage Density	Lineament Density	Slope	Land Use / Land Cover	Soil	Lithology	Weight
Precipitation	0.43	0.52	0.51	0.39	0.25	0.29	0.27	0.38
Drainage Density	0.14	0.17	0.17	0.23	0.25	0.29	0.21	0.21
Lineament Density	0.14	0.17	0.17	0.23	0.25	0.21	0.15	0.19
Slope	0.09	0.06	0.06	0.08	0.15	0.12	0.15	0.10
Land Use / Land Cover	0.09	0.03	0.03	0.03	0.05	0.04	0.09	0.05
Soil	0.06	0.02	0.03	0.03	0.05	0.04	0.09	0.05
Lithology	0.05	0.02	0.03	0.02	0.02	0.01	0.03	0.03

2.5. GROUNDWATER POTENTIALITY MAP

The groundwater potentiality map (Figure 5) was produced using thematic maps according to the AHP weights and calculated with a weighted overlay algorithm. The resulting map integrates data from the maps according to the AHP weights and is classified into 4 regions of groundwater potentiality, denoted by poor, fair, good, and very good potentiality. Thematic maps were resampled to 1 meter pixel size to obtain finer resolution end product.

Multi-source spatial data has been acquired and evaluated to design and evaluate a groundwater potentiality map and delineate regions that are suitable for optimal borehole placement (Russo et al., 2015). Validation for the groundwater potentiality map is done using available electrical resistivity tomography (ERT) data and well logs documented during previous field research performed in the study area and available in the public

domain for further humanitarian studies. Wells were manually drilled and logged by geophysicists and villagers in collaboration for community development.

Table 3. AHP final weights by percentage and effectiveness.

Factor	Class	Value	Rating	Weight	Effectiveness
	Very Low	130-140	10		4
	Low	140-155	30		11
	Moderate	155-165	50		19
	High	165-172	70		26
Precipitation	Very High	172-183	90	38%	34
	Very Low	0 - 13.5	10		2
	Low	13.6 - 27	30		6
	Moderate	27.1 - 40.6	50		10
	High	40.7 - 54.1	70		15
Drainage Density	Very High	54.2 - 67.6	90	21%	19
	Very Low	0 - 1.7	10		2
	Low	1.8 - 3.4	30		6
	Moderate	3.5 - 5	50		9
	High	5.1 - 6.7	70		13
Lineament Density	Very High	6.8 - 8.4	90	19%	17
	Very Low	> 35	10		1
	Low	15 - 35	30		3
	Moderate	5 - 15	50		5
	High	2 - 5	70		7
Slope	Very High	0 - 2	90	10%	9
	Very Low	Trees	10		1
	Low	Shrubs	30		2
	Moderate	Crops	50		3
	High	Grassland	70		4
Land Use / Land Cover	Very High	Water bodies	90	5%	5
	Very Low	Luvisol, very poorly drained	10		0
	Low	Cambisol, very poorly drained	30		1
	Moderate	Ferralsols, very poorly drained	50		2
	High	Ustoll, poorly drained	70		3
Soil	Very High	Acrisols, poorly drained	90	5%	4
	Very Low	Granite	10		0
	Low	Granulite	30		1
	Moderate	Gneiss	50		1
	High	Cataclasite	70		2
Lithology	Very High	Sedimentary Material	90	3%	2

3. RESULTS AND DISCUSSION

3.1. CHARACTERIZATION OF THEMATIC INPUT LAYERS

The region exhibits a dendritic drainage pattern with the three major river systems. The rivers are the Tochi River draining in the southern region of Gulu District, the Achwa River drains to the northeast of the region, and the Unyama River drains to the northwest (Figure 2A). However, precipitation was classified as the single greatest factor in groundwater potentiality (Figure 2B). The Gulu region experienced a maximum precipitation of 183 cm per year, which is classified as high within the AHP model, and a minimum precipitation of 130 cm per year in the northern region, which rates as low in the model. The granularity or coarseness of the precipitation data was a limiting factor.

The subject area is covered mainly by both grassland (57%) and tree cover (27%) and less area covered by crops (7%), water bodies (2%), and shrubs or herbaceous vegetation (6.8%) (Figure 2C) (Table 4). Grassland dominated the southern range of the study area while forests areas coincided roughly with regions with higher drainage density. Crops are concentrated in the central region near Gulu City. Water bodies are sporadic and poorly sensed in this dataset as rivers are barely visible and only in the northern region. Shrubs appear sporadically in the south and north.

The study area is composed mainly of gneiss (76%) with smaller areas of granulite (7%), granite (2%), cataclasite (1%), and unspecified sedimentary material (14%) (Figure 2D) (Table 4). Basement rocks of the study area are generally weathered crystalline granites and granitoids which have low permeability. Sedimentary materials occur within and adjacent to the Aswa Shear Zone and have higher permeabilities.

Soils in the study area are composed mainly of cambisols (42%)s and ferralsols (37%) (Table 4). Ustolls (9%) occur sporadically throughout the entire study area. Acrisols (12%) are concentrated mainly in the northern region while luvisols (<1%) only occur in the central region and are not visible in the soil map. All of the soil types in the study area are poorly drained or very poorly drained. The slopes are moderate to ideal (Figure 2F) with 62.9% of the subject area having 5% or less slope, which is favorable for recharge (Table 4). Lineament density is low over much of the study area (57.6%) with the highest lineament densities appearing in the Aswa Shear Zone in the northeast of the area (Figure 2G).

Table 4. AHP factors listed by percent area of interest and total area in kilometers.

Factor	Class	% AOI	Area (km^2)
Precipitation	Very Low	48.4	1,839
	Low	22.5	855
	Moderate	18.8	714
	High	8.7	331
	Very High	1.6	61
Drainage Density	Very Low	55.4	2,105
	Low	25.5	969
	Moderate	14.7	559
	High	4.1	156
	Very High	0.3	114
Lineament Density	Very Low	57.6	2,189
	Low	23.8	904
	Moderate	13.2	502
	High	4.7	179
	Very High	0.7	27
Slope	Very Low	0.2	600
	Low	1.3	1,790
	Moderate	35.6	1,353
	High	47.1	49
	Very High	15.8	8
Land Use / Land Cover	Very Low	26.8	1,018
	Low	6.8	258
	Moderate	7.4	281
	High	56.9	2,162
	Very High	2.1	80
Soil	Very Low	<1	<1
	Low	41.8	1589
	Moderate	36.5	1403
	High	9.2	354
	Very High	11.8	453
Lithology	Very Low	2	67
	Low	7	264
	Moderate	76	2,881
	High	1	54
	Very High	14	531

3.2. GROUNDWATER POTENTIALITY MAP

The highest groundwater potentiality is located in the very good classification with 455 km^2 (11.67%) of the subject area (Figure 4). The good classification is comprised of 1,980 km^2 of the study area which represents half (50.78%) of the land surface. These regions are mainly, but not entirely, located in the southern half of the study area where precipitation and vegetation is denser. There is 1,450 km^2 of fair groundwater potentiality, which is 37.12% of the surface within the study area. Poor groundwater potentiality is 13 km^2 in area and is 0.3% of the study area, located exclusively in the northern half of the study area.

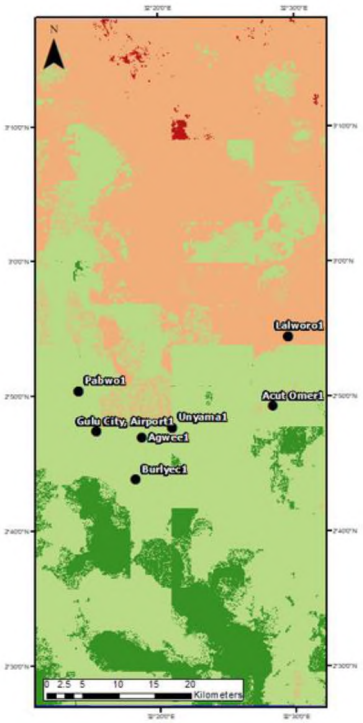

Figure 5. Groundwater potentiality map of Gulu District, Uganda with validation locations.

The distribution of greatest groundwater potentiality is situated in the southern half of the subject area with gradually decreasing groundwater potentiality toward the northern boundary of the study area. This is despite more porous lithology in the northern portion of the study area. The primary driver is the concentration of precipitation in the southern areas. This contributes to shallow aquifer recharge. The densest vegetation of the study area is located in the northern regions.

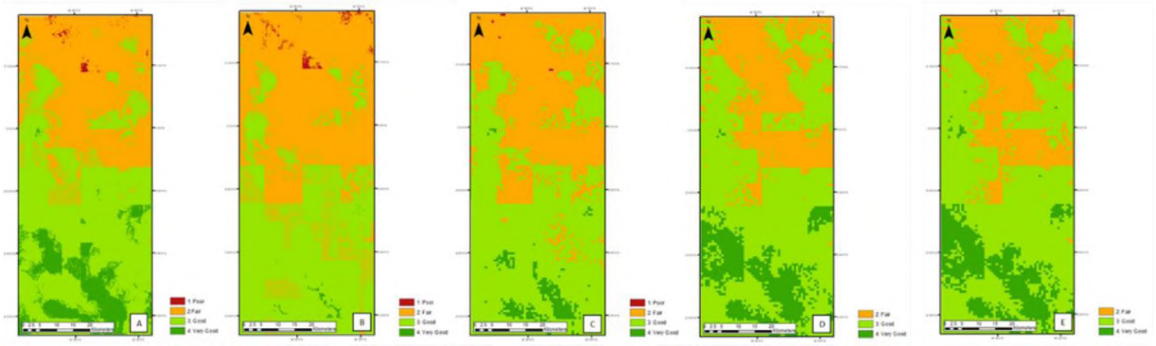

Figure 6. Groundwater potentiality maps varied according to lineament density maps. A) data fusion of SAR/magnetometry. B) SRTM DEM. C) Magnetic analytic signal. D) Magnetic first vertical derivative. E) Magnetic horizontal gradient.

The northern half of the study area is composed of mainly poor and fair groundwater potential which is expected due to lower precipitation levels, by comparison. Areas of good groundwater potentiality in the northern half of the study area is correlated to areas of high stream and lineament density. Similarly, areas of fair groundwater potentiality have comparatively low precipitation (<165 cm/year) and high stream density which contributes to greater surface water runoff instead of aquifer recharge. Areas of poor

groundwater potentiality lie in regions that have the least stream density and precipitation as well as less suitable soils and lithologies for groundwater recharge. Lineament density is greatest in the northeastern region of the subject area which contributes to localized regions that are rated as good groundwater potentiality rather than a classification of fair.

Groundwater potentiality across all data products exhibit very good potentiality near the southern portion of the study area with decreasing potentiality moving northward. Areas having a classification of poor were eliminated within the maps using the lineament density maps derived from the first vertical derivative and the magnetic horizontal gradient and comprised less than one percent of the area within the remaining data products (Figure 6) (Table 5). Areas classified as fair exists within all data products, ranging from 37% using the lineament density map from the fused data product, up to 50% in the potentiality map based on the SRTM DEM lineament density map. Areas classified at good groundwater potentiality are classified in all maps, which ranges from 50% to 59% of the study area. Areas classified as very good groundwater potentiality exist in all maps. Areas of very good groundwater potentiality based on the SRTM DEM lineament density map is less than 1% of the study area, potentiality based on the analytic signal is less than 4% of the study area and is between and 12% and 14% of the study area for the remaining maps.

Lineament density maps were used to generate several variations of groundwater potentiality maps. (Figure 6). The generated maps assessed groundwater potentiality based on lineament maps derived from a SAR/DGSM magnetometry data fusion (Figure 6A), an SRTM DEM (Figure 6B), the magnetic analytic signal (Figure 6C), the magnetic first

vertical derivative (Figure 6D), and the magnetic horizontal gradient (Figure 6E). (Jones et al, *in prep*) Other thematic maps used for the model were not varied from Figure 3.

Table 5. Percent and area of groundwater potentiality ratings according to lineament data product.

Factor	Class	Value	% AOI	Area (km^2)
	Very Low	130-140	48.4	1,839
	Low	140-155	22.5	855
	Moderate	155-165	18.8	714
	High	165-172	8.7	331
Precipitation	Very High	172-183	1.6	61
	Very Low	0 - 13.5	55.4	2,105
	Low	13.6 - 27	25.5	969
	Moderate	27.1 - 40.6	14.7	559
	High	40.7 - 54.1	4.1	156
Drainage Density	Very High	54.2 - 67.6	0.3	114
	Very Low	0 - 1.7	57.6	2,189
	Low	1.8 - 3.4	23.8	904
	Moderate	3.5 - 5	13.2	502
Lineament	High	5.1 - 6.7	4.7	179
Density	Very High	6.8 - 8.4	0.7	27
	Very Low	> 35	0.2	600
	Low	15 - 35	1.3	1,790
	Moderate	5 - 15	35.6	1,353
	High	2 - 5	47.1	49
Slope	Very High	0 - 2	15.8	8
	Very Low	Trees	26.8	1,018
	Low	Shrubs	6.8	258
	Moderate	Crops	7.4	281
Land Use / Land	High	Grassland	56.9	2,162
Cover	Very High	Water bodies	2.1	80
	Very Low	Luvisol, very poorly drained	<1	<1
	Low	Cambisol, very poorly drained	41.8	1589
	Moderate	Ferralsols, very poorly drained	36.5	1403
	High	Ustoll, poorly drained	9.2	354
Soil	Very High	Acrisols, poorly drained	11.8	453
	Very Low	Granite	2	67
	Low	Granulite	7	264
	Moderate	Gneiss	76	2,881
	High	Cataclasite	1	54
Lithology	Very High	Sedimentary Material	14	531

The distribution of greatest groundwater potentiality across all potentiality maps is situated in the southern half of the subject area with gradually decreasing groundwater potentiality moving toward the northern boundary of the study area. This may be due to the concentration of precipitation in the southern areas. The densest vegetation of the study area is located in the southern regions which is proportional to precipitation amounts and

may have a great affect on the end product. Coarse resolution of the precipitation data product appears to have influenced pixilation in all potentiality maps, though the map utilizing the lineament density map based on fused data appears to be the least pixelated.

The northern half of the study area across all data products is composed of mainly poor and fair groundwater potential. Areas of good groundwater potentiality in the northern half of the study area appears correlated to areas of high stream and lineament density. Similarly, areas of fair groundwater potentiality have comparatively low precipitation and high stream density which contributes to greater surface water runoff instead of aquifer recharge. Areas of poor groundwater potentiality lie in regions that have the least stream density and precipitation as well as less suitable soils and lithologies for groundwater recharge. Lineament density is greatest in the northeastern region of the subject area which appears to contribute to localized regions and may influence a higher rating of groundwater potentiality.

3.3. VALIDATION

Geoscientists Without Borders (GWB) conducted a geophysical groundwater project including groundwater exploration, well repair and maintenance, drilling, well construction, and water chemistry study of Acholiland, Northern Uganda, in 2018 (Bauman et al., 2018). Gulu District is one of seven districts located in Acholiland where the groundwater study occurred. Seven of the locations within the GWB investigation are located within the boundaries of this study area and have been located on the groundwater potentiality map based on the SAR/magnetic data fusion derived lineament density map.

Electrical Resistivity Tomography (ERT) surveys were conducted at each of the seven sites as well as either depth to groundwater or depth to bedrock in the corresponding boreholes.

All ERT surveys for the seven sites described the subsurface as massive, continuous crystalline bedrock overlain by either saturated saprolites or laterites, both of variable thicknesses. The saprolite layer is the optimal layer for aquifer access because boreholes are manually drilled. This layer varies from absent to a depth of up to 40 meters. In addition, field investigations of surrounding geology confirm the soil and lithology maps are accurate with regard to the reported materials and their extent. The reported average depth to bedrock from well logs among the entire Acholiland study is 25 meters.

Five of the seven sites have completed boreholes with 10.2 meters as the average depth to groundwater. Six of the seven sites are located with the classification of good on the groundwater potentiality map. The Lalworo site is the survey that lies within the fair classification region with 8 meters depth to groundwater drilled in the saturated saprolite. This demonstrates that the regions listed as fair in the groundwater potentiality map continue to have potential for groundwater access. The Lalworo location is the only one of the seven study sites with a well log, which documents well production of 6.1 gallons per minute. This suggests that though the potential for groundwater access exists in the fair classification, productivity of the well may not be optimal due to the low flow rate. In addition, it is unknown how long this flow rate was sustained.

3.4. SENSITIVITY ANALYSIS

A sensitivity analysis on the final groundwater potentiality map was performed by varying the order of the four highest weighted thematic maps and using the lineament density map derived from the data fusion of SAR/magnetometry lineament map (Figure 7). Four variations of the AHP were developed to assess the influence of each of the four highest weighted thematic maps and qualitatively determine the impact of each of the four weighted factors (Appendix D). Precipitation was the highest weighted AHP factor in Figure 4 followed by drainage density, lineament density, and slope and is duplicated in Figure 7A for ease of comparison. The first variation utilized the lineament density map is the highest weighted factor followed by drainage density, slope, and precipitation (Figure 7B). Drainage density is weighted as the most influential factor in the second variation followed by lineament density, precipitation, and slope (Figure 7C). The third variation uses slope as the highest weighted factor followed by precipitation, lineament density, and drainage density (Figure 7D). The fourth variation employs precipitation as the highest weighted factor as in Figure 7A but varies the order of the next three variables as slope, drainage density, and lineament density (Figure 7E).

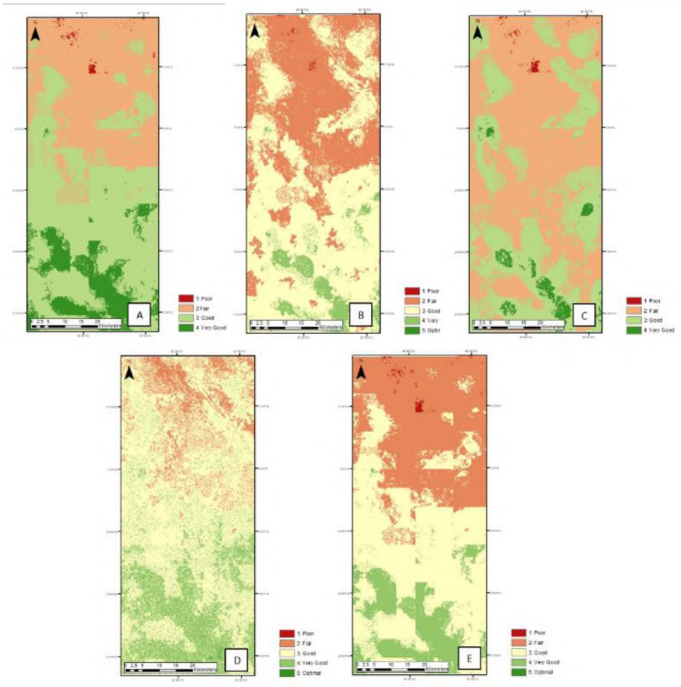

Figure 7. Groundwater potentiality maps varied according to variations of the top four weighted AHP factors. A) Precipitation, drainage density, lineament density, and slope (duplicated from previous figure). B) Lineament density, drainage density, slope, and precipitation. C) Drainage density, lineament density, precipitation, slope. D) Slope, precipitation, lineament density, drainage density. E) Precipitation, slope, drainage density, and lineament density.

4. CONCLUSION

This study evaluated several thematic maps of Gulu District, Uganda to develop a groundwater potentiality map according to the AHP method. Precipitation, DEM, soil, land cover, and geologic data was collected and processed. The resulting thematic maps include precipitation, slope, drainage density, soils, lithology, land cover, and lineament density. An AHP weighted model was developed to evaluate the priority and weights of variables necessary to assess the subject area for groundwater potentiality.

Precipitation has the greatest influence for groundwater recharge and potentiality and was given the highest weight in the model. The study region has high values of precipitation, mainly during the monsoon months, which positively influences the resulting groundwater potentiality map. However, the granularity of precipitation data is coarse, which results in a more pixelated end product. Drainage density of stream channels was the next highest weighted variable in the AHP model because streams are areas of high recharge concentration. Drainage density is concentrated along the southern region of the subject area as well as the northwest and northeast areas. Groundwater potentiality along the southern region mimics the shape of the stream density map resulting in high potential for aquifer productivity. Stream density in the northwest and northeast regions does not contribute a high influence due to less precipitation in the northern region of the study area.

Lineament density and slope are given weights of 19% and 10%, respectively, in the AHP method because they control surficial hydrologic inputs to the system's water balance. Lineaments of the ASZ are highly concentrated in the northeastern region where a fair to poor classification of potentiality dominates. There are sporadic areas of good groundwater potentiality in the regions with higher lineament density which appears somewhat correlated. There is a 15% slope in 98% of the subject area and 5% slope in 63% of the study area. Aquifer recharge from precipitation is greater in low slope regions because water has a lower flow velocity over gentle slopes than on steep slopes, thus has more time for soil penetration. Slope over the subject area is fairly uniform and, therefore, has a uniform effect over the majority of the study area. A region of poor groundwater potentiality exists in the eastern area of the northwest quadrant which correlates to a high

slope area. This indicates that though the slope has a uniform effect over much of the subject area, high slopes in this location greatly affect the groundwater potential.

The next lowest weights in the AHP model were given to both the soil and land cover maps. Soils in the region are generally saturated saprolites and laterites weathered from crystalline rock and are generally uniformly distributed throughout the region. Land cover consists mainly of grassland and tree cover, which are important for interception, but do not heavily influence recharge rates. These two maps contribute to groundwater potential; however, the low AHP weight ensures that these two maps do not heavily influence the end product. The lithological map was given the lowest weight in the AHP method due to the low permeability of crystalline rocks. The lithology predominantly consists of granitic or gneissic crystalline rocks which do not contribute to aquifer recharge.

The groundwater potentiality map was validated with geophysical ground-based ERT surveys and well log data. Groundwater potential was able to be validated throughout the central region but ground-based data was unavailable for the northern and southern regions. ERT surveys confirm that areas of good groundwater potential are valid because saturated saprolite aquifers are abundant in the survey areas. One ERT survey with an accompanying well log was documented in a region of fair groundwater potentiality. This particular well is currently productive. Thus, regions noted to be of fair groundwater potentiality may prove promising for future borehole drilling programs. More research is needed in areas of ground-based geophysical studies in this region to confirm groundwater potentiality findings.

A sensitivity analysis was performed to qualitatively assess the impact of each of the four highest weighted thematic maps on the final groundwater potentiality model. All

groundwater potentiality maps agree regarding general regional potentiality and classifications. Two groundwater potentiality maps with the least pixilation and the most agreement are the models using lineament density and slope as the highest weighted factors. These two maps appear to display preferential groundwater potentiality in areas of the Aswa Shear Zone fracture network in the northeast corner of the study area. Maps using precipitation as the highest weighted factor exhibit pixilation and appear to delineate potentiality along straight lines which is unreasonable thought precipitation could be the most influential factor. A higher quality precipitation data product would benefit this analysis greatly as would an analysis that considers monthly precipitation variations since groundwater potentiality is expected to vary across seasons.

In addition to needing finer resolution precipitation data to assess groundwater potentiality, other thematic maps would be beneficial to increase the confidence of regional and perhaps localized estimated groundwater potentiality. Well logs can provide the depth to groundwater data to produce piezometric maps, which could be used as a thematic map and factor in the potentiality model or used as a means of model validation. Available well logs in the study area are sporadic through the center of the study area while absent in the north and south, thus depth to groundwater cannot be extrapolated to adjacent regions. Access to more detailed geologic maps and evapotranspiration data would enable map generation for variables such as surficial geology, infiltration capacity, and water loss from the system. Aquifer permeability and vadose zone thickness are additional parameters that would aid in a thorough groundwater potentiality investigation, though developing countries are unlikely to have this level of data and these variables cannot be remotely sensed with confidence of accuracy. Finally, additional ERT investigations throughout the

study region would increase the confidence of potentiality model validation. More research is needed in areas of ground-based geophysical studies in this region to confirm groundwater potentiality findings and increase the confidence of groundwater potentiality estimates.

REFERENCES

Abdelkareem, M., Ghoneim, E., El-Baz, F., Askalany, M., 2012. New insight on paleoriver development in the Nile basin of the eastern Sahara. J. African Earth Sci. 62, 35–40. https://doi.org/10.1016/j.jafrearsci.2011.09.001

AbuBakr, M., Ghoneim, E., El-Baz, F., Zeneldin, M., Zeid, S., 2013. Use of radar data to unveil the paleolakes and the ancestral course of Wadi El-Arish, Sinai Peninsula, Egypt. Geomorphology 194, 34–45. https://doi.org/10.1016/j.geomorph.2013.04.005

Adeyinka, M., Idowu, A., Alaba, M., Adedapo, M., 2016. Interpretation of high resolution aeromagnetic data for lineaments study and occurrence of Banded Iron Formation in Ogbomoso area , Southwestern Nigeria. J. African Earth Sci. 114, 43–53. https://doi.org/10.1016/j.jafrearsci.2015.10.015

Ahmad, I., Verma, M.K., 2018. Application of Analytic Hierarchy Process in Water Resources Planning : A GIS Based Approach in the Identification of Suitable Site for Water Storage. Water Resour. Manag. 5093–5114.

Al-badani, M.A., Al-wathaf, Y.M., 2018. Using the aeromagnetic data for mapping the basement depth and contact locations , at southern part of Tihamah region , western Yemen. Egypt. J. Pet. 27, 485–495. https://doi.org/10.1016/j.ejpe.2017.07.015

Alexandr, F., 2017. Automated lineament analysis to assess geodynamic activity areas. Procedia Comput. Sci. 121, 699–706. https://doi.org/10.1016/j.procs.2017.11.091

Amro, I., Mateos, J., Vega, M., Molina, R., Katsaggelos, A.K., 2011. A survey of classical methods and new trends in pansharpening of multispectral images. J. Adv. Signal Process. 1–22.

Arii, M., Zyl, J.J. Van, Kim, Y., Member, S., 2011. Adaptive Model-Based Decomposition of Polarimetric SAR Covariance Matrices. IEEE Trans. Geosci. Remote Sens. 49, 1104–1113. https://doi.org/10.1109/TGRS.2010.2076285

Awad, S., Araffa, S., Helaly, A.S., Khozium, A., Lala, A.M.S., Soliman, S.A., Hassan, N.M., Awad, S., Araffa, S., Helaly, A.S., Khozium, A., Amir, M.S., Awad, S., Araffa, S., Helaly, A.S., Khozium, A., 2019. Delineating groundwater and subsurface structures by using 2D resistivity , gravity and 3D magnetic data. NRIAG J. Astron. Geophys. 4, 134–146. https://doi.org/10.1016/j.nrjag.2015.06.004

Awawdeh, M., Obeidat, M., Al-Mohammad, M., Al-Qudah, K., Jaradat, R., 2014. Integrated GIS and remote sensing for mapping groundwater potentiality in the Tulul al Ashaqif, Northeast Jordan. Arab. J. Geosci. 7, 2377–2392. https://doi.org/10.1007/s12517-013-0964-8

Azizur, M., Rusteberg, B., Salah, M., Lutz, A., 2013. An integrated study of spatial multicriteria analysis and mathematical modelling for managed aquifer recharge site suitability mapping and site ranking at Northern Gaza coastal aquifer. J. Environ. Manage. 124, 25–39. https://doi.org/10.1016/j.jenvman.2013.03.023

Bauman, P.D., Woods, L., Miazga, C., Layton, M., 2018. Community Groundwater Supply Development in Acholiland, Northern Uganda.

Belfiore, O.R., Meneghini, C., Parente, C., Santamaria, R., 2016. Application of different pan-sharpening methods on Worldview-3 images. ARPN J. Eng. Appl. Sci. 11, 490–496.

BGS, 2017. Hydrogeology of Uganda. Earthwise Africa Groundw. Atlas.

Blom, R.G., Crippen, R.E., Elachi, C., 1984. Detection of subsurface features in Seasat radar images of Means Valley, Mojave Desert, California. Geology 12, 346–349. https://doi.org/10.1130/0091-7613(1984)12<346:DOSFIS>2.0.CO;2

Brunner, P., Hendricks Franssen, H.J., Kgotlhang, L., Bauer-Gottwein, P., Kinzelbach, W., 2007. How can remote sensing contribute in groundwater modeling? Hydrogeol. J. 15, 5–18. https://doi.org/10.1007/s10040-006-0127-z

Chabot, D., Dillon, C., Shemrock, A., Weissflog, N., Sager, E.P.S., 2018. An Object-Based Image Analysis Workflow for Monitoring Shallow-Water Aquatic Vegetation in Multispectral Drone Imagery. Int. J. Geo-Information. https://doi.org/10.3390/ijgi7080294

Ciampalini, A., Raspini, F., Frodella, W., Bardi, F., Bianchini, S., Moretti, S., 2016. The effectiveness of high-resolution LiDAR data combined with PSInSAR data in landslide study. Landslides 399–410. https://doi.org/10.1007/s10346-015-0663-5

Demek, J., 1972. Manual of detailed geomorphological mapping. Academia, Prague.

Devi, M.B., Devanathan, R., 2019. Pansharpening of Remote Sensing Data of Earth Satellite Images. Procedia 6, 353–363.

Dhany, A., Muttil, N., Gokhan, A., Perera, B.J.C., 2017. Using the Analytic Hierarchy Process to identify parameter weights for developing a water quality index. Ecol. Indic. 75, 220–233. https://doi.org/10.1016/j.ecolind.2016.12.043

Dubey, B., Kartikeyan, B., Subbiah, M.M., 2018. Rational Polynomial Coefficients Modeling and Bias Correction by Using Iterative Polynomial Augmentation. J. Indian Soc. Remote Sens. 0123456789. https://doi.org/10.1007/s12524-018-0883-y

Durbach, I., Lahdelma, R., Salminen, P., 2014. The analytic hierarchy process with stochastic judgements. Eur. J. Oper. Res. 238, 552–559. https://doi.org/10.1016/j.ejor.2014.03.045

Elbeih, S.F., 2014. An overview of integrated remote sensing and GIS for groundwater mapping in Egypt. Ain Shams Eng. J. 6, 1–15. https://doi.org/10.1016/j.asej.2014.08.008

Escobar, D., Ayuga, F., Arnold, D., Wermuth, M., Ferna, J., 2017. ScienceDirect Sentinel-1A – First precise orbit determination results. Adv. Sp. Res. 60, 879–892. https://doi.org/10.1016/j.asr.2017.05.034

FAO, 2017. Mineral soils conditioned by a Wet (Sub) Tropical Climate [WWW Document]. URL http://www.fao.org/docrep/003/y1899e/y1899e08a.htm (accessed 1.1.17).

FAO, 1997. Soil Map of the World. Rome.

Farahbakhsh, E., Chandra, R., Olierook, H.K.H., Scalzo, R., Clark, C., Reddy, S.M., Müller, R.D., Farahbakhsh, E., Chandra, R., Olierook, H.K.H., Scalzo, R., Clark, C., Reddy, S.M., Müller, R.D., 2020. Computer vision-based framework for extracting tectonic lineaments from optical remote sensing data. Int. J. Remote Sens. 41, 1760–1787. https://doi.org/10.1080/01431161.2019.1674462

Fenta, A.A., Kifle, A., Gebreyohannes, T., Hailu, G., 2014. Spatial analysis of groundwater potential using remote sensing and GIS-based multi-criteria evaluation in Raya Valley, northern Ethiopia . Hydrogeol. J. 23, 195–206. https://doi.org/10.1007/s10040-014-1198-x

Frost, V.S., Member, S., Stiles, J.A., Member, S., 1982. A Model for Radar Images and Its Application to Adaptive Digital Filtering of Multiplicative Noise. IEEE Trans. Pattern Anal. Mach. Intell. 8, 231–239.

Gaber, A., Koch, M., Griesh, M.H., Sato, M., 2011. SAR remote sensing of buried faults: Implications for groundwater exploration in the western desert of Egypt. Sens. Imaging 12, 133–151. https://doi.org/10.1007/s11220-011-0066-1

Ghassemian, H., 2016. A review of remote sensing image fusion methods. Inf. Fusion 32, 75–89. https://doi.org/10.1016/j.inffus.2016.03.003

Ghayoumian, J., Saravi, M.M., 2007. Application of GIS techniques to determine areas most suitable for artificial groundwater recharge in a coastal aquifer in southern Iran 30, 364–374. https://doi.org/10.1016/j.jseaes.2006.11.002

Gil, J.J., 2014. Interpretation of the coherency matrix for three-dimensional polarization states. Phys. Rev. A 90.

Glenn, N.F., Streutker, D.R., Chadwick, D.J., Thackray, G.D., Dorsch, S.J., 2006. Analysis of LiDAR-derived topographic information for characterizing and differentiating landslide morphology and activity. Geomorphology 73, 131–148. https://doi.org/10.1016/j.geomorph.2005.07.006

Gomes, L., Rocha, D.M., César, A., Pires, B., Carmelo, A.C., Oswaldo, J., Filho, D.A., 2014. Geophysical characterization of the Azimuth 125 ◦ lineament with aeromagnetic data : Contributions to the geology of central Brazil. Precambrian Res. 249, 273–287. https://doi.org/10.1016/j.precamres.2014.05.005

GWB, 2018. Community Groundwater Supply Development in Acholiland , Northern Uganda. Calgary, AB.

Hall, J., 1986. Geophysical Lineaments and Deep Continental Structure. Philos. Trans. R. Soc. London 317, 33–44.

Hall, M., Diggens, J., 2011. The East African Rift System - A view from space. Geo Expro Mag. Vol 8., 96.

Hengl, T., Jesus, J.M. De, Heuvelink, G.B.M., Ruiperez, M., Kilibarda, M., Blagoti, A., Shangguan, W., Wright, M.N., Geng, X., Bauer-marschallinger, B., Guevara, M.A., Vargas, R., Macmillan, R.A., Batjes, N.H., Leenaars, J.G.B., Ribeiro, E., Wheeler, I., Mantel, S., Kempen, B., 2017. SoilGrids250m : Global gridded soil information based on machine learning. PLoS One 1–41. https://doi.org/10.1371/journal.pone.0169748

Henrique, P., Santos, D., Miranda, S., Ornaghi, D., Anna, S., Henrique, C., Oliveira, D., Duarte, H., 2019. The analytic hierarchy process supporting decision making for sustainable development : An overview of applications. J. Clean. Prod. 212, 119–138. https://doi.org/10.1016/j.jclepro.2018.11.270

Katumwehe, A.B., Abdelsalam, M.G., Atekwana, E.A., Laó-Dávila, D.A., 2016. Extent, kinematics and tectonic origin of the Precambrian Aswa Shear Zone in eastern Africa. Gondwana Res. 34, 241–253. https://doi.org/10.1016/j.gr.2015.03.007

Kim, Y., van Zyl, J.J., 2009. A Time-Series Approach to Estimate Soil Moisture Using Polarimetric Radar Data. Geosci. Remote Sensing, IEEE Trans. 47, 2519–2527. https://doi.org/10.1109/TGRS.2009.2014944

Kupidura, P., 2016. Comparison of filters dedicated to speckle suppression in SAR Images. Int. Arch. Photogramm. Remote Sens. Spat. Inf. Sci. XLI, 12–19. https://doi.org/10.5194/isprsarchives-XLI-B7-269-2016

Lasaponara, R., Masini, N., 2013. Satellite synthetic aperture radar in archaeology and cultural landscape: An overview. Archaeol. Prospect. 20, 71–78. https://doi.org/10.1002/arp.1452

Laurencelle, J., Logan, T., Gens, R., 2015. ASF Radiometrically Terrain Corrected ALOS PALSAR products Product guide (No. 1.2). ASF Engineering.

Lee, J., Fellow, L., Ainsworth, T.L., Member, S., 2011. The Effect of Orientation Angle Compensation on Coherency Matrix and Polarimetric Target Decompositions. IEEE Trans. Geosci. Remote Sens. 49, 53–64. https://doi.org/10.1109/TGRS.2010.2048333

Lee, S., Kim, Y.S., Oh, H.J., 2012. Application of a weights-of-evidence method and GIS to regional groundwater productivity potential mapping. J. Environ. Manage. 96, 91–105. https://doi.org/10.1016/j.jenvman.2011.09.016

Li, X., 2001. Tutorial Ellipsoid , geoid , gravity , geodesy , and geophysics 66, 1660–1668.

Luo, Q., Hu, M., Zhao, Z., Li, J., Zeng, Z., 2020. Design and experiments of X-type artificial control targets for a UAV-LiDAR system. Int. J. Remote Sens. 41, 3307–3321. https://doi.org/10.1080/01431161.2019.1701210

Macdonald, A.M., Davies, J., 2000a. A brief review of groundwater for rural water supply in sub-Saharan. Br. Geol. Surv. Tech. Rep. WC/00/33 13. https://doi.org/WC/00/33

Macdonald, A.M., Davies, J., 2000b. A brief review of groundwater for rural water supply in sub-Saharan Africa. Br. Geol. Surv. Tech. Rep. WC/00/33 13. https://doi.org/WC/00/33

Mahyoub, S., Fadil, A., Mansour, E.M., Rhinane, H., Al-nahmi, F., 2019. Fusing of optical and synthetic aperture radar (SAR) remote sensing data: a systematic literature review (SLR). Int. Arch. Photogramm. Remote Sens. Spat. Inf. Sci. XLII, 10–11.

Meyer, F.J., Nicoll, J.B., 2008. Prediction , Detection , and Correction of Faraday Rotation in Full-Polarimetric L-Band SAR Data. IEEE Trans. Geosci. Remote Sens. 46, 3076–3086. https://doi.org/10.1109/TGRS.2008.2003002

Milas, A.S., Warner, T.A., Younan, N.H., Balenovic, I., Larson, M.D., Simic, A., Warner, T.A., Younan, N.H., Balenovic, I., 2019. Preface for the Special Issue of IJRS Drones section in. Int. J. Remote Sens. 40, 9065–9069. https://doi.org/10.1080/01431161.2019.1658409

Mutiti, S., Levy, J., Mutiti, C., Gaturu, N.S., 2010. Assessing ground water development potential using Landsat imagery. Ground Water 48, 295–305. https://doi.org/10.1111/j.1745-6584.2008.00524.x

Noureldin, A., Karamat, T.B., Georgy, J., 2013. Fundamentals of inertial navigation, satellite-based positioning and their integration, Fundamentals of Inertial Navigation, Satellite-Based Positioning and their Integration. https://doi.org/10.1007/978-3-642-30466-8

Olierook, H.K.H., Scalzo, R., Kohn, D., Chandra, R., Farahbakhsh, E., Houseman, G., Clark, C., Reddy, S.M., Müller, R.D., 2019. Bayesian geological and geophysical data fusion for the construction and uncertainty quantification of 3D geological models. Solid Earth Discuss. 1–34.

Oyawale, A.A., Adeoti, F.O., Ajayi, T.R., Omitogun, A.A., 2020. Applications of remote sensing and geographic information system (GIS) in regional lineament mapping and structural analysis in Ikare Area , Southwestern Nigeria. J. Geol. Min. Res. 12, 13–24. https://doi.org/10.5897/JGMR2019.0310

Pan, Y., Ren, C., Liang, Y., Zhang, Z., Shi, Y., 2020. Inversion of surface vegetation water content based on GNSS - IR and MODIS data fusion. Satell. Navig. 1–15. https://doi.org/10.1186/s43020-020-00021-z

Pavez, A., Remy, D., Bonvalot, S., Diament, M., Gabalda, G., Froger, J., 2006. Insight into ground deformations at Lascar volcano (Chile) from SAR interferometry , photogrammetry and GPS data : Implications on volcano dynamics and future space monitoring. Remote Sens. Environ. 100, 307–320. https://doi.org/10.1016/j.rse.2005.10.013

Pavlic, G., Singhroy, V., Duk-Rodkin, A., Alasset, P., 2008. Satellite data fusion techniques for terrain and surficial geological mapping, in: IEEE IGARSS. pp. 314–317. https://doi.org/10.1109/IGARSS.2008.4779346

Rahmati, O., Haghizadeh, A., Stefanidis, S., 2016. Assessing the Accuracy of GIS-Based Analytical Hierarchy Process for Watershed Prioritization ; Gorganrood River 1131–1150. https://doi.org/10.1007/s11269-015-1215-4

Rahnama, M., Gloaguen, R., 2014. TecLines: A MATLAB-Based Toolbox for Tectonic Lineament Analysis from Satellite Images and DEMs, Part 1: Line Segment Detection and Extraction. Remote Sens. 5938–5958. https://doi.org/10.3390/rs6075938

Republic of Uganda, 2019. Airborne Geophysical Digital Data Dissemination Policy.

Reynolds, J.M., 1997. An Introduction to Applied and Environmental Geophysics. John Wiley & Sons Ltd.

Robins, N.S., Davies, J., Farr, J.L., Calow, R.C., 2006. The changing role of hydrogeology in semi-arid southern and eastern Africa. Hydrogeol. J. 14, 1483–1492. https://doi.org/10.1007/s10040-006-0056-x

Rott, H., 1984. The Analysis of Backscattering Properties from SAR Data of Mountain Regions. IEEE J. Ocean. Eng. 9, 347–355. https://doi.org/10.1109/JOE.1984.1145655

Russo, T.A., Fisher, A.T., Lockwood, B.S., 2015. Assessment of Managed Aquifer Recharge Site Suitability Using a GIS and Modeling 53, 389–400. https://doi.org/10.1111/gwat.12213

Saalmann, K., Mänttäri, I., Nyakecho, C., Isabirye, E., 2016. Age, tectonic evolution and origin of the Aswa Shear Zone in Uganda: Activation of an oblique ramp during convergence in the East African Orogen. J. African Earth Sci. 117, 303–330. https://doi.org/10.1016/j.jafrearsci.2016.02.002

Saaty, T.L., 1994. How To Make A Decision : The Analytic Hierarchy Process 75–105.

Salem, A., Fairhead, J., Ravat, D., Smith, R., 2007. Tilt-depth method : A simple depth estimation method using first-order magnetic derivatives. Lead. Edge 3–6.

Sandoval, J.A., Tiburan, C.L., 2019. Identification of potential artificial groundwater recharge sites in Mount Makiling Forest Reserve , Philippines using GIS and Analytical Hierarchy Process. Appl. Geogr. 105, 73–85. https://doi.org/10.1016/j.apgeog.2019.01.010

Senanayake, I.P., Dissanayake, D.M.D.O.K., Mayadunna, B.B., Weerasekera, W.L., 2016. An approach to delineate groundwater recharge potential sites in Ambalantota, Sri Lanka using GIS techniques. Geosci. Front. 7, 115–124. https://doi.org/10.1016/j.gsf.2015.03.002

Sener, E., Davraz, A., 2013. Assessment of groundwater vulnerability based on a modified DRASTIC model , GIS and an analytic hierarchy process (AHP) method: the case of Egirdir Lake basin (Isparta , Turkey). Hydrogeol. J. 701–714. https://doi.org/10.1007/s10040-012-0947-y

Shahdoosti, H.R., Ghassemian, H., 2016. Combining the spectral PCA and spatial PCA fusion methods by an optimal filter. Inf. Fusion 27, 150–160. https://doi.org/10.1016/j.inffus.2015.06.006

Sloots, R., 2010. Ministry of Water and Environment Assessment of Groundwater Investigations and Borehole Drilling Capacity in Uganda.

Small, D., 2011. Flattening Gamma : Radiometric Terrain Correction for SAR Imagery. IEEE Trans. Geosci. Remote Sens. 49, 3081–3093.

Srivastava, H.S., Patel, P., Navalgund, R.R., 2006. How far SAR has fulfilled its expectation for soil moisture retrieval. Microw. Remote Sens. Atmos. Environ. 6410, 641001. https://doi.org/10.1117/12.693946

Strozzi, T., Delaloye, R., Kääb, A., Ambrosi, C., Perruchoud, E., 2010. Combined observations of rock mass movements using satellite SAR interferometry , differential GPS , airborne digital photogrammetry , and airborne photography interpretation. J. Geophys. Res. 115, 1–12. https://doi.org/10.1029/2009JF001311

Tagnon, B.O., 2016. Statistical and Geostatistical Analysis of Lineaments Network Mapped in The Precambrian Basement : Case of Divo-Oume Region (Southern Cote d ' Ivoire). Eur. Sci. J. 12, 299–318. https://doi.org/10.19044/esj.2016.v12n33p299

Thannoun, R.G., 2013. Automatic Extraction and Geospatial Analysis of Lineaments and their Tectonic Significance in some areas of Northern Iraq using Remote Sensing Techniques and GIS. Int. J. Enhanc. Reseaarch Sci. Technol. Eng. 2, 1–11.

Tsiko, R.G., Haile, T.S., 2011. Integrating Geographical Information Systems, Fuzzy Logic and Analytical Hierarchy Process in Modelling Optimum Sites for Locating Water Reservoirs. A Case Study of the Debub District in Eritrea. Water 254–290. https://doi.org/10.3390/w3010254

Turkar, V., Bombay, I.I.T., 2011. Applying Coherent and Incoherent Target Decomposition Techniques to Polarimetric SAR Data 23–29.

UNDP, WHO, WFP, Uganda, R. of, Project, N.U.E.R., 2013. Rays of Hope in Lango Sub-Region, Northern Uganda.

Van Zyl, Jakob; Kim, Y., 2011. Synthetic Aperture Radar Polarimetry. John Wiley & Sons, Inc.

Vasuki, Y., Holden, E., Kovesi, P., Micklethwaite, S., 2014. Semi-automatic mapping of geological structures using UAV-based photogrammetric data : An image analysis approach. Comput. Geosci. 69, 22–32. https://doi.org/10.1016/j.cageo.2014.04.012

Vijayaraj, V., Younan, N.H., Hara, C.G.O., 2006. Concepts of Image Fusion in Remote Sensing Applications, in: 2006 IEEE International Symposium on Geoscience and Remote Sensing. pp. 3781–3784. https://doi.org/10.1109/IGARSS.2006.973

Wald, L., Ranchin, T., Mangolini, M., Wald, L., Ranchin, T., Mangolini, M., 2009. Fusion of satellite images of different spatial resolutions : Assessing the quality of resulting images To cite this version : HAL Id : hal-00365304.

Walker, P.J.P., 2013. Basis of an Australian Radar Soil Moisture Algorithm Theoretical Baseline Document (ATBD).

Wang, Xiaofei, Wang, Xiaoyi, 2020. Spatiotemporal Fusion of Remote Sensing Image Based on Deep Learning. J. Sensors 2020.

Xu, G., Xu, Y., 2016. GPS: Theory, algorithms and applications, third edition. GPS Theory, Algorithms Appl. Third Ed. 1–489. https://doi.org/10.1007/978-3-662-50367-6

Xu, W., Lan, Y., Li, Y., Luo, Y., He, Z., 2019. Classification method of cultivated land based on UAV visible light remote sensing. Int. J. Agric. Biol. Eng. 12, 103–109. https://doi.org/10.25165/j.ijabe.20191203.4754

Yeomans, C.M., Middleton, M., Shail, R.K., Grebby, S., Lusty, P.A.J., 2019. Integrated Object-Based Image Analysis for semi-automated geological lineament detection in southwest England. Comput. Geosci. 123, 137–148. https://doi.org/10.1016/j.cageo.2018.11.005

Zeng, T., Yin, W., Ding, Z., Long, T., 2016. Motion and Doppler Characteristics Analysis Based on Circular Motion Model in Geosynchronous SAR. IEEE J. Sel. Top. Appl. Earth Obs. Remote Sens. 9, 1132–1142. https://doi.org/10.1109/JSTARS.2015.2429915

Zhang, X., Tang, X., Gao, X., Zhao, H., 2018. Multitemporal Soil Moisture Retrieval over Bare Agricultural Areas by Means of Alpha Model with Multisensor SAR Data. Adv. Meteorol. 2018, 17.

Zhu, X.X., Member, S., Montazeri, S., Gisinger, C., Hanssen, R.F., Member, S., Bamler, R., 2016. Geodetic SAR Tomography. IEEE Trans. Geosci. Remote Sens. 54, 18–35. https://doi.org/10.1109/TGRS.2015.2448686

Zyl, J.J. Van, Arii, M., Kim, Y., Member, S., 2011. Model-Based Decomposition of Polarimetric SAR Covariance Matrices Constrained for Nonnegative Eigenvalues. IEEE Trans. Geosci. Remote Sens. 49, 3452–3459. https://doi.org/10.1109/TGRS.2011.2128325

SECTION

2. CONCLUSIONS AND RECOMMENDATIONS

2.1. CONCLUSIONS

This dissertation research has endeavored to develop a methodology by which to investigate groundwater potentiality in developing countries using GIS and RS techniques. Pixel level data fusion was proposed and proven as a viable process to enhance edge detection within photogrammetry and SAR for lineament analysis. This data fusion method was later used to integrate lineament structures observed in SAR and magnetometry for surface and subsurface lineament detection. This data product was then used as one of several thematic maps to develop a groundwater potentiality map of Gulu District, Uganda using a weighted multi-criteria decision matrix. The overall methodology is applicable to any area that has both airborne magnetic data and Alos Palsar quad pol data available.

Though several optimal well drilling regions have been delineated, it is the author's experience that exploitation of drilling sites must be selective for sustainable water well development and anthropogenic concerns regarding food security. The life of a typical, successful water well in this AOI has been approximated at five years. Failure is due to a lack of skilled labor for operations and maintenance of well heads, pump systems, etc. Historically, villages have become dependent on a sole water resource only to suffer from thirst and famine when the well system becomes dysfunctional, therefore anthropogenic considerations are paramount for a viable humanitarian solutions framework.

Consideration has been given to the development of this method for rapid assessment of borehole drilling programs in the case of natural disasters and armed conflict scenarios within developing countries. Various United Nations agencies coordinate with United States CIV-MIL operations to provide humanitarian assistance within the first 24 hours of any disaster. Typically, UNOCHA, UNICEF, UNHCR, and UNDP personnel are not equipped with the skills to identify regional, emergency water resources for effective, emergency borehole drilling programs in developing countries. The shortfall in skilled, rapid borehole placement prolongs the transportation of potable water to disaster-stricken areas. Though the rapid placement of borehole location using remotely sensed data cannot ensure successful well completion in all geologic provinces, it will reduce the number of dry holes drilled which is typical in refugee and IDP camp construction.

The universe of discourse within this research paradigm advances groundwater investigations within the international humanitarian space, which supplements the tradecraft of national security through aid efforts targeting natural disaster and armed conflict theaters. Domestic natural disaster recovery efforts are often isolated from armed conflict situations; however, to separate the two within an international context is to present a false dichotomy – they occur simultaneously. Water is always the first need after disaster strikes within any context and remote sensing can easily be used to target water resources for vulnerable populations.

2.2. RECOMMENDATIONS

This research has aimed to investigate surface expressions of shallow subsurface features and anomalies. Future research of shallow subsurface features using X, C, L, and

P bands of high resolution SAR is possible to develop an array of intelligence, security, or humanitarian endeavors. Relevant object detection includes fractures, buried munitions, foxholes, landmines, UXO, mass graves, and other buried features. A feature of this method is that the material properties of buried objects are unnecessary for identification of a generalizable object location since the method can often remotely sense what is *not* there, rather than what *is* there. For example, buried UXO will not only be surrounded by void spaces but also a variation in soil moisture along object boundaries can be detected when high resolution SAR data products are available. Remote identification of buried features affords greater security to assets in the field by minimizing the time spent ground truthing in-country during humanitarian missions.

Geomorphologic terrain analysis as well as terrestrial identification of shallow subsurface environments and their surface expressions has been accomplished within this research, therefore aforementioned feature identification is anticipated to be within the scope of the research capabilities for future image interpretation and modeling efforts. Upon completion of this doctoral research, it is this principal investigator's intention to continue the research with the goal of remote object identification using high resolution SAR data products, varying polarizations, and object image analysis methods as well as machine learning and computer vision modeling methods.

APPENDIX A.

MATRIX DECOMPOSITIONS

Polarimetric SAR processing and analysis relies heavily on matrix mathematics, therefore it is necessary to set the foundation of the mathematics presented in this paper. Matrix mathematics is essential in the study of SAR polarimetry because it is a convenient method to represent systems of linear equations of radar signals into vector spaces. Linear systems of equations associated with a vector space are described as eigenvalues and eigenvectors and the vector space is referred to as an eigenspace. A set of vectors in a vector space is referred to as a basis, B. Matrix manipulation of vector space is necessary to transform between coordinate systems of the sensing platforms, define SAR polarimetry operations, and perform pixel operations on sensed data.

The eigen equation of matrix **A**, from the vector space, **v**, is:

$$\mathbf{A}\mathbf{v} = \lambda\mathbf{v} \qquad \text{Eq. 1}$$

where λ is a scalar known as the eigenvalue and **v** is the eigenvector of **Av**. The matrix **A** multiplies the eigenvector **v** by the value of λ. **A** can be also written as:

$$(\lambda I - \mathrm{A})\mathbf{v} = 0 \qquad \text{Eq. 2}$$

where I is the unit matrix of the square N x N matrix. This results in the equation:

$$det(\lambda \boldsymbol{I} - \boldsymbol{A}) = |\lambda \boldsymbol{I} - \boldsymbol{A}| = 0 \qquad \text{Eq. 3}$$

where the determinant (det) is the scalar value that describes the scaling factor of the characteristic polynomial:

$$\boldsymbol{AV} = \boldsymbol{A}[\boldsymbol{v}_1,\ldots,\boldsymbol{v}_n] = [\lambda_1\boldsymbol{v}_1,\ldots,\lambda_n\boldsymbol{v}_n] = [\boldsymbol{v}_1,\ldots,\boldsymbol{v}_n]\begin{bmatrix}\lambda_1 & 0 & \ldots & 0\\ 0 & \lambda_2 & \ldots & 0\\ \vdots & \vdots & \ddots & \vdots\\ 0 & 0 & \ldots & \lambda_n\end{bmatrix} = \boldsymbol{V\Lambda} \qquad \text{Eq. 4}$$

where:

$$\boldsymbol{\Lambda} = diag[\lambda_1,\ldots,\lambda_n] \qquad \text{and} \qquad \boldsymbol{V} = [\boldsymbol{v}_1,\ldots,\boldsymbol{v}_n] \qquad \text{Eq. 5}$$

Alternatively, these equations can be written as:

$$\boldsymbol{A} = \boldsymbol{V\Lambda V^{-1}} \qquad \text{Eq. 6}$$

which is a product of three matrices, called the eigenvalue decomposition. Or:

$$\boldsymbol{V^{-1}AV} = \boldsymbol{\Lambda} \qquad \text{Eq. 7}$$

where **A** is diagonalized by the eigenvector matrix **V**.

Diagonalizing a matrix is a method of finding a matrix's eignevalues by transforming the matrix into a separate coordinate system. It is a technique used to simplify the *NxN* matrix for analysis of the characteristics of the eigenspace properties

and is a linear transformation of a vector space. The notation for the transformation of $\mathbb{R}^n$ to $\mathbb{R}^m$ is represented by:

$$T: \mathbb{R}^n \rightarrow \mathbb{R}^m \qquad \text{Eq. 8}$$

where T is the transformation that assigns each vector x in $\mathbb{R}^n$ a vector $T(x)$ in $\mathbb{R}^m$.

Concepts such as eigenspaces, diagonalization, and linear transformation of basis are necessary concepts for polarimetric matrix operations such as decompositions. Matrix decomposition, also known as spectral decomposition, is the process of factoring a matrix into the product of three other matrices to describe the eigenspace. This process effectively decorrelates the radar signal data and reduces the dimensionality of data which enables analysis of eigenspace properties through the simplification of more complex operations. A variety of decomposition methods exist for varying purposes. This paper utilizes three methods: principal component (PC) analysis, Pauli matrices, and the Van Zyl decomposition. The circular polarization method augments the previous methods in that is is a synthetic polarization obtained through algorithmic combinations of both the horizontal and vertical polarizations.

APPENDIX B.

SAR POLARIMETRIC DECOMPOSITIONS

SAR sensors transmit electromagnetic fields to the surface of the earth and the radar backscatter is received as a result. The field is transmitted and the backscatter is received in either horizontal or vertical waveforms, thus a horizontally transmitted electromagnetic wave and the horizontally received backscatter data are described as HH with the first term describing the transmit geometry and the second term describing the receiving geometry. Alos Palsar QUAD-POL data was used for this study to obtain a complete characterization of the study area. The polarizations acquired during satellite orbit were HH, HV, VV, and VH and are called polarization states. Subsequent to data acquisition a synthetic circular polarization was constructed. Objects sensed on the ground are called scatterers and each scatterer transforms the polarization state of the received backscatter data which is described in vector form in a scattering matrix. Combinations of the various polarized scattering matrices are called polarimetric decompositions and are useful for analysis and interpretation of the radar cross section (RCS).

Polarimetric decompositions are used to reveal information about various surface properties and their backscattering mechanisms. Two general types of decompositions are Coherent Target Decomposition (CTD) and Incoherent Target Decomposition (ICTD). Coherent targets are used to study manmade objects which are known to have linear and uniform scattering mechanisms. Incoherent targets are natural targets the express distributed and non-uniform backscattering properties. This paper uses the PauliRGB CTD, the Van Zyl ICTD, and a synthesized circular polarimetric radar scattering matrix to differentiate between coherent and incoherent scattering targets.

The PauliRGB decomposition is derived from Pauli spin matrices used in quantum mechanics and is a coherent target decomposition (CTD). It is based on linear combinations

of backscattering matrix vectors. PauliRGB is represented by a (3x3) Coherency **[T3]** matrix which represents scattering mechanisms within a pixel as well as their subsequent contribution to the total radar signal. A coherency matrix is used to analyze partially polarized waves by representing the correlations of the wave components. The **[T3]** matrix is found by projecting a Sinclair matrix onto the Pauli spin matrix set.

The coherent backscattering matrix, *S (Eq. 1)*, (also called the Sinclair matrix) of a backscattered electromagnetic wave is represented by the scattering matrix:

$$\begin{pmatrix} S_{hh} & S_{hv} \\ S_{hv} & S_{vv} \end{pmatrix} = S_{hh}\begin{pmatrix} 1 & 0 \\ 0 & 0 \end{pmatrix} + S_{hv}\begin{pmatrix} 0 & 1 \\ 1 & 0 \end{pmatrix} + S_{vv}\begin{pmatrix} 0 & 0 \\ 0 & 1 \end{pmatrix} \quad \text{Eq. 1}$$

which yields the vector form (Eq. 2):

$$\begin{pmatrix} S_{hh} \\ S_{hv} \\ S_{vv} \end{pmatrix} = S_{hh}\begin{pmatrix} 1 \\ 0 \\ 0 \end{pmatrix} + S_{hv}\begin{pmatrix} 0 \\ 1 \\ 0 \end{pmatrix} + S_{vv}\begin{pmatrix} 0 \\ 0 \\ 1 \end{pmatrix} \quad \text{Eq. 2}$$

It should be noted that the polarizations HV and VH are considered symmetrical (cross-channel reciprocity) and, thus, only the HV polarizations is utilized within the matrices (Eq. 3).

$$\begin{pmatrix} S_{hh} & S_{hv} \\ S_{hv} & S_{vv} \end{pmatrix} = \frac{a}{\sqrt{2}}\begin{bmatrix} 1 & 0 \\ 0 & 1 \end{bmatrix} + \frac{b}{\sqrt{2}}\begin{bmatrix} 1 & 0 \\ 0 & -1 \end{bmatrix} + c\begin{bmatrix} 0 & 1 \\ 1 & 0 \end{bmatrix} + d\begin{bmatrix} 0 & -j \\ j & 0 \end{bmatrix} \quad \text{Eq. 3}$$

where the complex values are given by (Eq. 4, Eq. 5, Eq. 6, Eq. 7):

$$a = \frac{S_{hh} + S_{vv}}{\sqrt{2}} \quad \text{Eq. 4}$$

$$b = \frac{S_{hh} - S_{vv}}{\sqrt{2}} \quad \text{Eq. 5}$$

$$c = \frac{S_{hv} + S_{vh}}{\sqrt{2}} \quad \text{Eq. 6}$$

$$d = j\frac{S_{hv} + S_{vh}}{\sqrt{2}} \quad \text{Eq. 7}$$

The complex values are the four scattering mechanisms: *a*. odd or single bounce (surface) scattering, *b*. even or double bounce scattering, *c*. volume scattering, and *d*. the antisymmetric components of the *S* matrix. Where HV and VH are considered symmetric (cross-channel reciprocity), S_{hv}=S_{vh} *c* and *d* are modified to (Eq. 8, Eq. 9):

$$c = \frac{S_{hv} + S_{vh}}{\sqrt{2}} = 2\frac{S_{hv} + S_{hv}}{\sqrt{2}} = 2\frac{S_{vh} + S_{vh}}{\sqrt{2}} = 2\frac{S_{hv}}{\sqrt{2}} = 2\frac{S_{vh}}{\sqrt{2}} \quad \text{Eq. 8}$$

$$d = j\frac{S_{hv} - S_{vh}}{\sqrt{2}} = j\frac{S_{hv} - S_{hv}}{\sqrt{2}} = j\frac{S_{vh} - S_{vh}}{\sqrt{2}} = j\frac{0}{\sqrt{2}} = 0 \quad \text{Eq. 9}$$

The final Pauli basis decomposition is expressed as the coherent scattering vector (Pauli vector) κ_p (Eq. 10):

$$\kappa_p = \begin{bmatrix} \kappa_1 \\ \kappa_2 \\ \kappa_3 \end{bmatrix} = \frac{1}{\sqrt{2}} \begin{bmatrix} S_{hv} + S_{vh} \\ 2S_{hv} \\ S_{hh} - S_{vv} \end{bmatrix} \quad \text{Eq. 10}$$

The [T3] Coherency matrix (Eq. 11) is defined as:

$$[T_3] = \begin{bmatrix} T_{11} & T_{12} & T_{13} \\ T_{12} & T_{22} & T_{23} \\ T_{13} & T_{23} & T_{33} \end{bmatrix} \quad \text{Eq. 11}$$

A series of matrix operations (Lee et al., 2011) for the projection of κ_p on T (Eq. 12) yields:

$$[T] = \frac{1}{2} \begin{bmatrix} \langle |S_{HH} + S_{VV}|^2 \rangle & \langle (S_{HH} + S_{VV})(S_{HH} - S_{VV})^* \rangle & 2\langle (S_{HH} + S_{VV}) S_{HV}^* \rangle \\ \langle (S_{HH} - S_{VV})(S_{HH} + S_{VV})^* \rangle & \langle |S_{HH} - S_{VV}|^2 \rangle & 2\langle (S_{HH} - S_{VV}) S_{HV}^* \rangle \\ 2\langle S_{HV}(S_{HH} + S_{VV})^* \rangle & 2\langle S_{HV}(S_{HH} - S_{VV})^* \rangle & 4\langle |S_{HV}|^2 \rangle \end{bmatrix} \quad \text{Eq. 12}$$

where * denotes conjugation and <> denotes averaging. All nine elements of the [T3] Coherency matrix are computed for each pixel of the image. The PauliRGB decomposition utilizes the diagonal elements of the matrix as the red ($T22$), green ($T33$), and blue ($T11$) (Eq. 13, Eq. 14, Eq. 15) by convention and is defined as:

$$T_{11} = |S_{HH} + S_{VV}|^2 \quad \text{Eq. 13}$$

$$T_{22} = |S_{HH} - S_{VV}|^2 \quad \text{Eq. 14}$$

$$T_{33=} 2|S_{HV}|^2 \quad \text{Eq. 15}$$

PauliRGB backscattering matrix target decompositions results in a color-coding of the polarimetric channels of HH-VV, HV, and HH+VV, respectively. These polarimetric channels correspond to the backscattering mechanisms associated with double bounce scattering reflected from objects, volume scattering from object geometry, and single bounce scattering from the surface.

The Van Zyl decomposition is a type of ICTD and is characterized by single (surface) bounce, double bounce, and volume scattering mechanisms. The Van Zyl algorithm is a vectorized form of the Sinclair matrix used for PauliRGB decomposition and is considered an eigenvalue method. The Van Zyl decomposition utilizes a 3x3 Covariance [C3] matrix. A covariance matrix correlates each of the polarization channels and is based on the decomposition of the [T3] Coherency matrix.

The [C3] covariance matrix (Eq. 16, Eq. 17) is defined as:

$$[C_3] = \begin{bmatrix} C_{11} & C_{12} & C_{13} \\ C_{12} & C_{22} & C_{23} \\ C_{13} & C_{23} & C_{33} \end{bmatrix} \quad \text{Eq. 16}$$

where:

$$[C_3] = \begin{bmatrix} S_{HH} \\ \sqrt{2}S_{HV} \\ S_{VV} \end{bmatrix} \begin{bmatrix} S_{HH} & \sqrt{2}S_{HV} & S_{VV} \end{bmatrix}^* = \begin{bmatrix} S_{HH}S_{HH}^* & \sqrt{2}S_{HH}S_{HV}^* & S_{HH}S_{VV}^* \\ \sqrt{2}S_{HV}S_{HH}^* & 2S_{HV}S_{HV}^* & \sqrt{2}S_{HV}S_{VV}^* \\ S_{VV}S_{HH}^* & \sqrt{2}S_{VV}S_{HV}^* & S_{VV}S_{VV}^* \end{bmatrix} \quad \text{Eq. 17}$$

and where the asterisk represents the complex conjugate. The diagonal of the matrix (Eq. 18, Eq. 19, Eq. 20) yields:

$$C_{11} = |S_{HH}|^2 \quad \text{Eq.18}$$

$$C_{22} = |S_{HV}|^2 \quad \text{Eq.19}$$

$$C_{33} = |S_{VV}|^2 \quad \text{Eq.20}$$

The resulting Van Zyl image is classified based on these parameters. The surface scatterer (C_{11}), the dihedral scatterer (C_{22}), and the diffuse scattering mechanism (C_{33}). This method finds the single, dominant scatterer for each pixel rather than the total power of the three scatterings mechanisms.

Electrons and the magnetic field traveling through the ionosphere potentially experience Faraday rotation of the electromagnetic waveform due to atmospheric density. Radar systems that send and receive through the ionosphere at L band wavelengths or longer can experience distortion of the transmitted and received signals. This distortion is exaggerated at periods of high solar activity and at tropical latitudes.

The SAR data used for this research was acquired during a period of low solar activity but the location of the study area is at low latitude within the tropics. The calibration algorithms adopted by the European Space Agency (ESA) correct for the Faraday effect, therefore signal distortion within the linearly polarized data should be negligible. Circular polarizations are not affected by Faraday rotation due to the curvilinear nature of the waveform, thus the analysis of the circular polarization was deemed worthy of investigation.

A synthetic circular polarization was constructed using ESA's SNAP radar processing platform. The data was processed according to the right and left circular geometries and a scattering matrix was generated. The previously described RTC process

was employed to generate the final circular polarimetric product using the right circular vertical, right circular horizontal, and left horizontal horizontal (RCV/RCH/LHH) combination.

APPENDIX C.

LINEAMENT EXTRACTION RESULTS

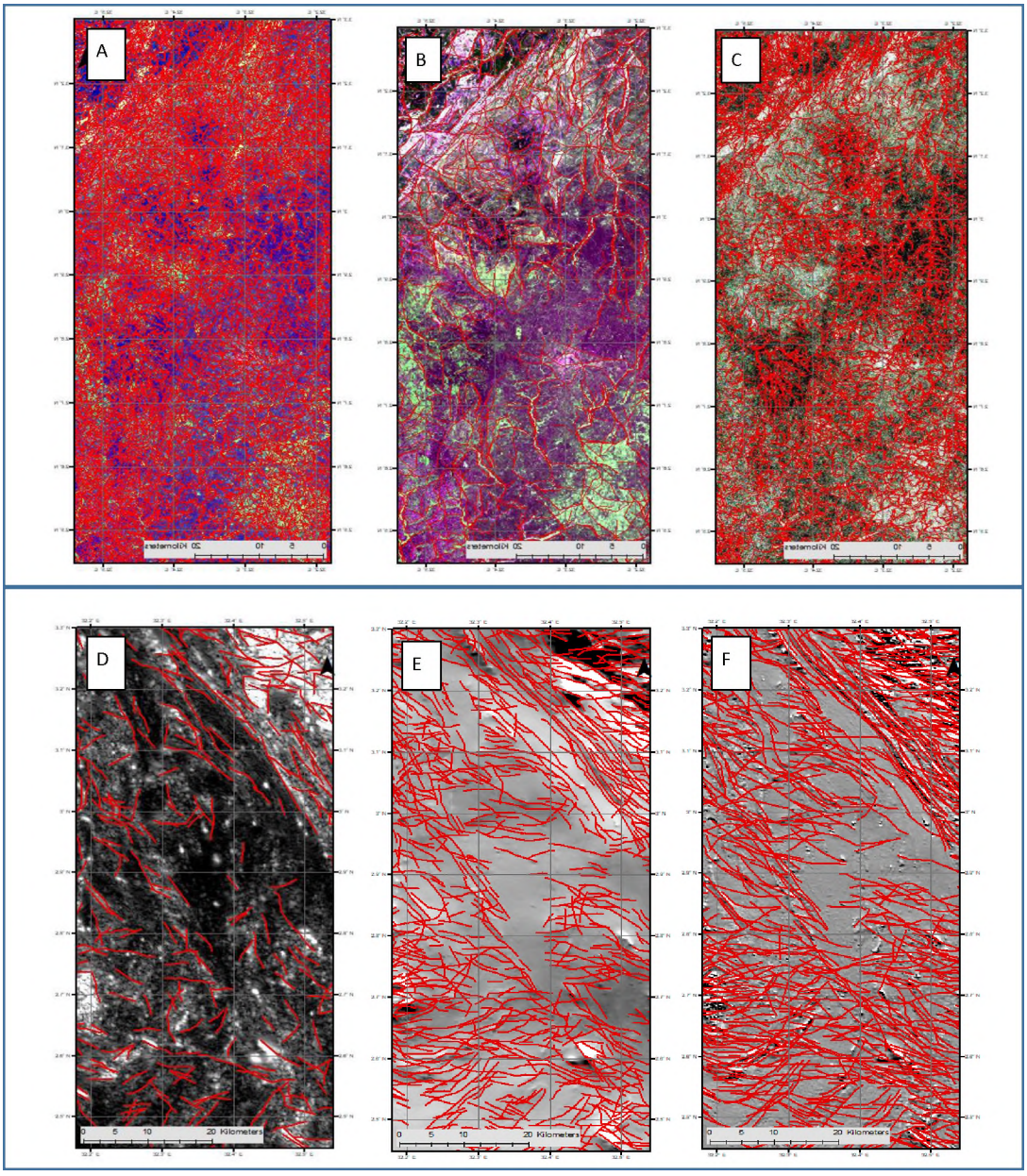

Figure C1. Lineaments extracted from SAR and magnetic datasets. A) PauliRGB. B) Van Zyl. C) Circular. D) Analytic Signal. E) Horizontal Gradient. F) First Vertical Derivative.

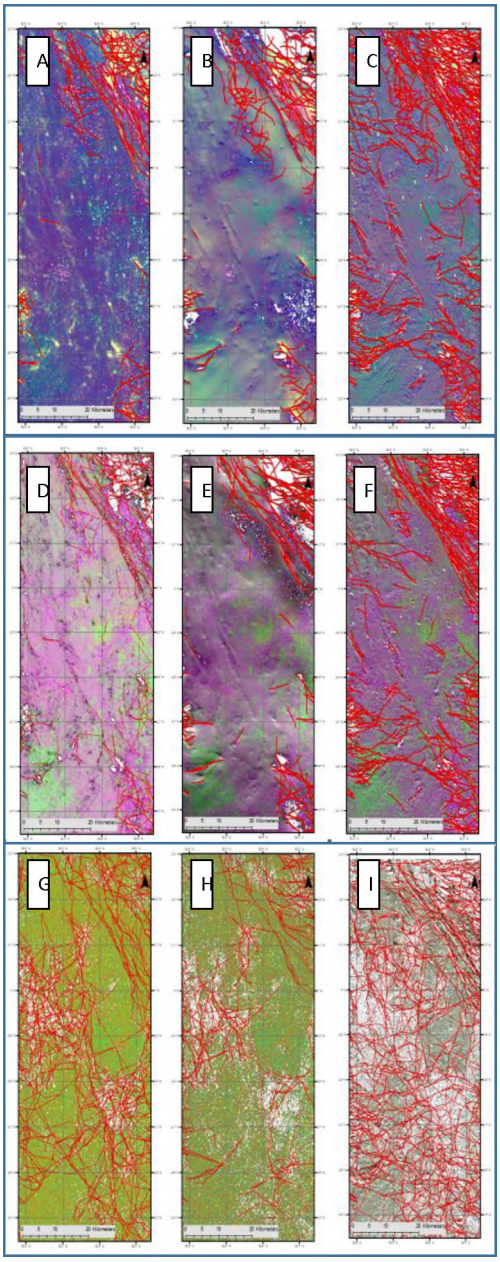

Figure C2. Lineaments extracted from SAR and magnetic fused datasets. A) PauliRGB/Analytic Signal. B) PauliRGB/Horizontal Gradient. C) PauliRGB/First Vertical Derivative. D)Van Zyl/Analytic Signal. E) Van Zyl/Horizontal Derivative. F) Van Zyl/First Vertical Derivative. G) Circular/Analytic Signal. H) Circular/Horizontal Gradient. I) Circular/First Vertical Derivative.

APPENDIX D.

VARIATIONS OF AHP MODEL

Table D1: First variation of pairwaise comparison of groundwater potentiality map.

Pairwise Comparison							
	Lineament Density	Drainage Density	Slope	Precipitation	Land Use / Land Cover	Soil	Lithology
Lineament Density	1	3	5	5	7	7	9
Drainage Density	1/3	1	1	3	5	7	7
Slope	1/5	1	1	3	5	5	5
Precipitation	1/5	1/3	1/3	1	3	3	5
Land Use / Land Cover	1/7	1/5	1/5	1/3	1	1	3
Soil	1/7	1/7	1/5	1/3	1	1	3
Lithology	1/9	1/7	1/5	1/5	1/3	1/3	1
Total	2.13	5.82	7.93	12.87	22.33	24.33	33.00

Table D2. First variation of final weights of groundwater potentiality map.

Final Weights								
	Lineament Density	Drainage Density	Slope	Precipitation	Land Use / Land Cover	Soil	Lithology	Weight
Lineament Density	0.47	0.52	0.63	0.39	0.31	0.29	0.27	0.41
Drainage Density	0.16	0.17	0.13	0.23	0.22	0.29	0.21	0.20
Slope	0.09	0.17	0.13	0.23	0.22	0.21	0.15	0.17
Precipitation	0.09	0.06	0.04	0.08	0.13	0.12	0.15	0.10
Land Use / Land Cover	0.07	0.03	0.03	0.03	0.04	0.04	0.09	0.05
Soil	0.07	0.02	0.03	0.03	0.04	0.04	0.09	0.05
Lithology	0.05	0.02	0.03	0.02	0.01	0.01	0.03	0.03

Table D3. First variation of factors of groundwater potentiality map.

Factor	Class	Value	Rating	Weight	Effectiveness
	Very Low	130-140	10		4
	Low	140-155	30		11
	Moderate	155-165	50		19
	High	165-172	70		26
Precipitation	Very High	172-183	90	38%	34
	Very Low	0 - 13.5	10		2
	Low	13.6 - 27	30		6
	Moderate	27.1 - 40.6	50		10
	High	40.7 - 54.1	70		15
Drainage Density	Very High	54.2 - 67.6	90	21%	19
	Very Low	0 - 1.7	10		2
	Low	1.8 - 3.4	30		6
	Moderate	3.5 - 5	50		9
	High	5.1 - 6.7	70		13
Lineament Density	Very High	6.8 - 8.4	90	19%	17
	Very Low	> 35	10		1
	Low	15 - 35	30		3
	Moderate	5 - 15	50		5
	High	2 - 5	70		7
Slope	Very High	0 - 2	90	10%	9
	Very Low	Trees	10		1
	Low	Shrubs	30		2
	Moderate	Crops	50		3
Land Use / Land	High	Grassland	70		4
Cover	Very High	Water bodies	90	5%	5
	Very Low	Luvisol, very poorly drained	10		0
	Low	Cambisol, very poorly drained	30		1
	Moderate	Ferralsols, very poorly drained	50		2
	High	Ustoll, poorly drained	70		3
Soil	Very High	Acrisols, poorly drained	90	5%	4
	Very Low	Granite	10		0
	Low	Granulite	30		1
	Moderate	Gneiss	50		1
	High	Cataclasite	70		2
Lithology	Very High	Sedimentary Material	90	3%	2

Table D4: Second variation of pairwise comparison of groundwater potentiality map.

Pairwise Comparison							
	Drainage Density	Lineament Density	Precipitation	Slope	Land Use / Land Cover	Soil	Lithology
Drainage Density	1	3	5	5	7	7	9
Lineament Density	1/3	1	1	3	5	7	7
Precipitation	1/5	1	1	3	5	5	5
Slope	1/5	1/3	1/3	1	3	3	5
Land Use / Land Cover	1/7	1/5	1/5	1/3	1	1	3
Soil	1/7	1/7	1/5	1/3	1	1	3
Lithology	1/9	1/7	1/5	1/5	1/3	1/3	1
Total	2.13	5.82	7.93	12.87	22.33	24.33	33.00

Table D5. Second variation of final weights of groundwater potentiality map.

Final Weights								
	Drainage Density	Lineament Density	Precipitation	Slope	Land Use / Land Cover	Soil	Lithology	Weight
Drainage Density	0.47	0.52	0.63	0.39	0.31	0.29	0.27	0.41
Lineament Density	0.16	0.17	0.13	0.23	0.22	0.29	0.21	0.20
Precipitation	0.09	0.17	0.13	0.23	0.22	0.21	0.15	0.17
Slope	0.09	0.06	0.04	0.08	0.13	0.12	0.15	0.10
Land Use / Land Cover	0.07	0.03	0.03	0.03	0.04	0.04	0.09	0.05
Soil	0.07	0.02	0.03	0.03	0.04	0.04	0.09	0.05
Lithology	0.05	0.02	0.03	0.02	0.01	0.01	0.03	0.03

Table D6. Second variation of factors of groundwater potentiality map.

Factor	Class	Value	Rating	Weight	Effectiveness
	Very Low	0 - 13.5	10		4
	Low	13.6 - 27	30		12
	Moderate	27.1 - 40.6	50		21
	High	40.7 - 54.1	70		29
Drainage Density	Very High	54.2 - 67.6	90	41%	37
	Very Low	0 - 1.7	10		2
	Low	1.8 - 3.4	30		6
	Moderate	3.5 - 5	50		10
	High	5.1 - 6.7	70		14
Lineament Density	Very High	6.8 - 8.4	90	20%	18
	Very Low	130-140	10		2
	Low	140-155	30		5
	Moderate	155-165	50		9
	High	165-172	70		12
Precipitation	Very High	172-183	90	17%	16
	Very Low	> 35	10		1
	Low	15 - 35	30		3
	Moderate	5 - 15	50		5
	High	2 - 5	70		7
Slope	Very High	0 - 2	90	10%	9
	Very Low	Trees	10		0
	Low	Shrubs	30		1
	Moderate	Crops	50		2
	High	Grassland	70		3
Land Use / Land Cover	Very High	Water bodies	90	5%	4
	Very Low	Luvisol, very poorly drained	10		0
	Low	Cambisol, very poorly drained	30		1
	Moderate	Ferralsols, very poorly drained	50		2
	High	Ustoll, poorly drained	70		3
Soil	Very High	Acrisols, poorly drained	90	5%	4
	Very Low	Granite	10		0
	Low	Granulite	30		1
	Moderate	Gneiss	50		1
	High	Cataclasite	70		2
Lithology	Very High	Sedimentary Material	90	3%	2

Table D7: Third variation of pairwise comparison of groundwater potentiality map.

Pairwise Comparison							
	Slope	Precipitation	Lineament Density	Drainage Density	Land Use / Land Cover	Soil	Lithology
Slope	1	3	5	5	7	7	9
Precipitation	1/3	1	1	3	5	7	7
Lineament Density	1/5	1	1	3	5	5	5
Drainage Density	1/5	1/3	1/3	1	3	3	5
Land Use / Land Cover	1/7	1/5	1/5	1/3	1	1	3
Soil	1/7	1/7	1/5	1/3	1	1	3
Lithology	1/9	1/7	1/5	1/5	1/3	1/3	1
Total	2.13	5.82	7.93	12.87	22.33	24.33	33.00

Table D8. Third variation of final weights of groundwater potentiality map.

Final Weights								
	Slope	Precipitation	Lineament Density	Drainage Density	Land Use / Land Cover	Soil	Lithology	Weight
Slope	0.47	0.52	0.63	0.39	0.31	0.29	0.27	0.41
Precipitation	0.16	0.17	0.13	0.23	0.22	0.29	0.21	0.20
Lineament Density	0.09	0.17	0.13	0.23	0.22	0.21	0.15	0.17
Drainage Density	0.09	0.06	0.04	0.08	0.13	0.12	0.15	0.10
Land Use / Land Cover	0.07	0.03	0.03	0.03	0.04	0.04	0.09	0.05
Soil	0.07	0.02	0.03	0.03	0.04	0.04	0.09	0.05
Lithology	0.05	0.02	0.03	0.02	0.01	0.01	0.03	0.03

Table D9. Third variation of factors of groundwater potentiality map.

Factor	Class	Value	Rating	Weight	Effectiveness
	Very Low	> 35	10		4
	Low	15 - 35	30		12
	Moderate	5 - 15	50		21
	High	2 - 5	70		29
Slope	Very High	0 - 2	90	41%	37
	Very Low	130-140	10		2
	Low	140-155	30		6
	Moderate	155-165	50		10
	High	165-172	70		14
Precipitation	Very High	172-183	90	20%	18
	Very Low	0 - 1 7	10		2
	Low	1 8 - 3 4	30		5
	Moderate	3 5 - 5	50		9
	High	5 1 - 6 7	70		12
Lineament Density	Very High	6 8 - 8 4	90	17%	16
	Very Low	0 - 13.5	10		1
	Low	13 6 - 27	30		3
	Moderate	27 1 - 40 6	50		5
	High	40 7 - 54 1	70		7
Drainage Density	Very High	54 2 - 67 6	90	10%	9
	Very Low	Trees	10		0
	Low	Shrubs	30		1
	Moderate	Crops	50		2
	High	Grassland	70		3
Land Use / Land Cover	Very High	Water bodies	90	5%	4
	Very Low	Luvisol, very poorly drained	10		0
	Low	Cambisol, very poorly drained	30		1
	Moderate	Ferralsols, very poorly drained	50		2
	High	Ustoll, poorly drained	70		3
Soil	Very High	Acrisols, poorly drained	90	5%	4
	Very Low	Granite	10		0
	Low	Granulite	30		1
	Moderate	Gneiss	50		1
	High	Cataclasite	70		2
Lithology	Very High	Sedimentary Material	90	3%	2

Table D10: Fourth variation of pairwise comparison of groundwater potentiality map.

Pairwise Comparison							
	Precipitation	Slope	Drainage Density	Lineament Density	Land Use / Land Cover	Soil	Lithology
Precipitation	1	3	5	5	7	7	9
Slope	1/3	1	1	3	5	7	7
Drainage Density	1/5	1	1	3	5	5	5
Lineament Density	1/5	1/3	1/3	1	3	3	5
Land Use / Land Cover	1/7	1/5	1/5	1/3	1	1	3
Soil	1/7	1/7	1/5	1/3	1	1	3
Lithology	1/9	1/7	1/5	1/5	1/3	1/3	1
Total	2.13	5.82	7.93	12.87	22.33	24.33	33.00

Table D11. Fourth variation of final weights of groundwater potentiality map.

Final Weights								
	Precipitation	Slope	Drainage Density	Lineament Density	Land Use / Land Cover	Soil	Lithology	Weight
Precipitation	0.47	0.52	0.63	0.39	0.31	0.29	0.27	0.41
Slope	0.16	0.17	0.13	0.23	0.22	0.29	0.21	0.20
Drainage Density	0.09	0.17	0.13	0.23	0.22	0.21	0.15	0.17
Lineament Density	0.09	0.06	0.04	0.08	0.13	0.12	0.15	0.10
Land Use / Land Cover	0.07	0.03	0.03	0.03	0.04	0.04	0.09	0.05
Soil	0.07	0.02	0.03	0.03	0.04	0.04	0.09	0.05
Lithology	0.05	0.02	0.03	0.02	0.01	0.01	0.03	0.03

Table D12. Fourth variation of factors of groundwater potentiality map.

Factor	Class	Value	Rating	Weight	Effectiveness
Precipitation	Very Low	130-140	10	41%	4
	Low	140-155	30		12
	Moderate	155-165	50		21
	High	165-172	70		29
	Very High	172-183	90		37
Slope	Very Low	> 35	10	20%	2
	Low	15 - 35	30		6
	Moderate	5 - 15	50		10
	High	2 - 5	70		14
	Very High	0 - 2	90		18
Drainage Density	Very Low	0 - 13 5	10	17%	2
	Low	13 6 - 27	30		5
	Moderate	27 1 - 40 6	50		9
	High	40 7 - 54 1	70		12
	Very High	54 2 - 67 6	90		16
Lineament Density	Very Low	0 - 1 7	10	10%	1
	Low	1 8 - 3 4	30		3
	Moderate	3 5 - 5	50		5
	High	5 1 - 6 7	70		7
	Very High	6 8 - 8 4	90		9
Land Use / Land Cover	Very Low	Trees	10	5%	0
	Low	Shrubs	30		1
	Moderate	Crops	50		2
	High	Grassland	70		3
	Very High	Water bodies	90		4
Soil	Very Low	Luvisol, very poorly drained	10	5%	0
	Low	Cambisol, very poorly drained	30		1
	Moderate	Ferralsols, very poorly drained	50		2
	High	Ustoll, poorly drained	70		3
	Very High	Acrisols, poorly drained	90		4
Lithology	Very Low	Granite	10	3%	0
	Low	Granulite	30		1
	Moderate	Gneiss	50		1
	High	Cataclasite	70		2
	Very High	Sedimentary Material	90		2

BIBLIOGRAPHY

Abdelkareem, M., Ghoneim, E., El-Baz, F., Askalany, M., 2012. New insight on paleoriver development in the Nile basin of the eastern Sahara. J. African Earth Sci. 62, 35–40. https://doi.org/10.1016/j.jafrearsci.2011.09.001

AbuBakr, M., Ghoneim, E., El-Baz, F., Zeneldin, M., Zeid, S., 2013. Use of radar data to unveil the paleolakes and the ancestral course of Wadi El-Arish, Sinai Peninsula, Egypt. Geomorphology 194, 34–45. https://doi.org/10.1016/j.geomorph.2013.04.005

Adeyinka, M., Idowu, A., Alaba, M., Adedapo, M., 2016. Interpretation of high resolution aeromagnetic data for lineaments study and occurrence of Banded Iron Formation in Ogbomoso area , Southwestern Nigeria. J. African Earth Sci. 114, 43–53. https://doi.org/10.1016/j.jafrearsci.2015.10.015

Ahmad, I., Verma, M.K., 2018. Application of Analytic Hierarchy Process in Water Resources Planning : A GIS Based Approach in the Identification of Suitable Site for Water Storage. Water Resour. Manag. 5093–5114.

Al-badani, M.A., Al-wathaf, Y.M., 2018. Using the aeromagnetic data for mapping the basement depth and contact locations , at southern part of Tihamah region , western Yemen. Egypt. J. Pet. 27, 485–495. https://doi.org/10.1016/j.ejpe.2017.07.015

Alexandr, F., 2017. Automated lineament analysis to assess geodynamic activity areas. Procedia Comput. Sci. 121, 699–706. https://doi.org/10.1016/j.procs.2017.11.091

Amro, I., Mateos, J., Vega, M., Molina, R., Katsaggelos, A.K., 2011. A survey of classical methods and new trends in pansharpening of multispectral images. J. Adv. Signal Process. 1–22.

Arii, M., Zyl, J.J. Van, Kim, Y., Member, S., 2011. Adaptive Model-Based Decomposition of Polarimetric SAR Covariance Matrices. IEEE Trans. Geosci. Remote Sens. 49, 1104–1113. https://doi.org/10.1109/TGRS.2010.2076285

Awad, S., Araffa, S., Helaly, A.S., Khozium, A., Lala, A.M.S., Soliman, S.A., Hassan, N.M., Awad, S., Araffa, S., Helaly, A.S., Khozium, A., Amir, M.S., Awad, S., Araffa, S., Helaly, A.S., Khozium, A., 2019. Delineating groundwater and subsurface structures by using 2D resistivity , gravity and 3D magnetic data interpretation around Cairo NRIAG J. Astron. Geophys. 4, 134–146. https://doi.org/10.1016/j.nrjag.2015.06.004

Awawdeh, M., Obeidat, M., Al-Mohammad, M., Al-Qudah, K., Jaradat, R., 2014. Integrated GIS and remote sensing for mapping groundwater potentiality in the Tulul al Ashaqif, Northeast Jordan. Arab. J. Geosci. 7, 2377–2392.

Azizur, M., Rusteberg, B., Salah, M., Lutz, A., 2013. An integrated study of spatial multicriteria analysis and mathematical modelling for managed aquifer recharge site suitability mapping and site ranking at Northern Gaza coastal aquifer. J. Environ. Manage. 124, 25–39. https://doi.org/10.1016/j.jenvman.2013.03.023

Bauman, P.D., Woods, L., Miazga, C., Layton, M., 2018. Community Groundwater Supply Development in Acholiland, Northern Uganda.

Belfiore, O.R., Meneghini, C., Parente, C., Santamaria, R., 2016. Application of different pan-sharpening methods on Worldview-3 images. ARPN J. Eng. Appl. Sci. 11, 490–496.

BGS, 2017. Hydrogeology of Uganda. Earthwise Africa Groundw. Atlas.

Blom, R.G., Crippen, R.E., Elachi, C., 1984. Detection of subsurface features in Seasat radar images of Means Valley, Mojave Desert, California. Geology 12, 346–349. https://doi.org/10.1130/0091-7613(1984)12<346:DOSFIS>2.0.CO;2

Brunner, P., Hendricks Franssen, H.J., Kgotlhang, L., Bauer-Gottwein, P., Kinzelbach, W., 2007. How can remote sensing contribute in groundwater modeling? Hydrogeol. J. 15, 5–18. https://doi.org/10.1007/s10040-006-0127-z

Chabot, D., Dillon, C., Shemrock, A., Weissflog, N., Sager, E.P.S., 2018. An Object-Based Image Analysis Workflow for Monitoring Shallow-Water Aquatic Vegetation in Multispectral Drone Imagery. Int. J. Geo-Information. https://doi.org/10.3390/ijgi7080294

Ciampalini, A., Raspini, F., Frodella, W., Bardi, F., Bianchini, S., Moretti, S., 2016. The effectiveness of high-resolution LiDAR data combined with PSInSAR data in landslide study. Landslides 399–410. https://doi.org/10.1007/s10346-015-0663-5

Demek, J., 1972. Manual of detailed geomorphological mapping. Academia, Prague.

Devi, M.B., Devanathan, R., 2019. Pansharpening of Remote Sensing Data of Earth Satellite Images. Procedia 6, 353–363.

Dhany, A., Muttil, N., Gokhan, A., Perera, B.J.C., 2017. Using the Analytic Hierarchy Process to identify parameter weights for developing a water quality index. Ecol. Indic. 75, 220–233. https://doi.org/10.1016/j.ecolind.2016.12.043

Dubey, B., Kartikeyan, B., Subbiah, M.M., 2018. Rational Polynomial Coefficients Modeling and Bias Correction by Using Iterative Polynomial Augmentation. J. Indian Soc. Remote Sens. 0123456789. https://doi.org/10.1007/s12524-018-0883

Durbach, I., Lahdelma, R., Salminen, P., 2014. The analytic hierarchy process with stochastic judgements. Eur. J. Oper. Res. 238, 552–559. https://doi.org/10.1016/j.ejor.2014.03.045

Elbeih, S.F., 2014. An overview of integrated remote sensing and GIS for groundwater mapping in Egypt. Ain Shams Eng. J. 6, 1–15. https://doi.org/10.1016/j.asej.2014.08.008

Escobar, D., Ayuga, F., Arnold, D., Wermuth, M., Ferna, J., 2017. ScienceDirect Sentinel-1A – First precise orbit determination results. Adv. Sp. Res. 60, 879–892. https://doi.org/10.1016/j.asr.2017.05.034

FAO, 2017. Mineral soils conditioned by a Wet (Sub) Tropical Climate [WWW Document]. URL http://www.fao.org/docrep/003/y1899e/y1899e08a.htm (accessed 1.1.17).

FAO, 1997. Soil Map of the World. Rome.

Farahbakhsh, E., Chandra, R., Olierook, H.K.H., Scalzo, R., Clark, C., Reddy, S.M., Müller, R.D., Farahbakhsh, E., Chandra, R., Olierook, H.K.H., Scalzo, R., Clark, C., Reddy, S.M., Müller, R.D., 2020. Computer vision-based framework for extracting tectonic lineaments from optical remote sensing data. Int. J. Remote Sens. 41, 1760–1787. https://doi.org/10.1080/01431161.2019.1674462

Fenta, A.A., Kifle, A., Gebreyohannes, T., Hailu, G., 2014. Spatial analysis of groundwater potential using remote sensing and GIS-based multi-criteria evaluation in Raya Valley, northern Ethiopia . Hydrogeol. J. 23, 195–206. https://doi.org/10.1007/s10040-014-1198-x

Frost, V.S., Member, S., Stiles, J.A., Member, S., 1982. A Model for Radar Images and Its Application to Adaptive Digital Filtering of Multiplicative Noise. IEEE Trans. Pattern Anal. Mach. Intell. 8, 231–239.

Gaber, A., Koch, M., Griesh, M.H., Sato, M., 2011. SAR remote sensing of buried faults: Implications for groundwater exploration in the western desert of Egypt. Sens. Imaging 12, 133–151. https://doi.org/10.1007/s11220-011-0066-1

Ghassemian, H., 2016. A review of remote sensing image fusion methods. Inf. Fusion 32, 75–89. https://doi.org/10.1016/j.inffus.2016.03.003

Ghayoumian, J., Saravi, M.M., 2007. Application of GIS techniques to determine areas most suitable for artificial groundwater recharge in a coastal aquifer in southern Iran 30, 364–374. https://doi.org/10.1016/j.jseaes.2006.11.002

Gil, J.J., 2014. Interpretation of the coherency matrix for three-dimensional polarization states. Phys. Rev. A 90.

Glenn, N.F., Streutker, D.R., Chadwick, D.J., Thackray, G.D., Dorsch, S.J., 2006. Analysis of LiDAR-derived topographic information for characterizing and differentiating landslide morphology and activity. Geomorphology 73, 131–148. https://doi.org/10.1016/j.geomorph.2005.07.006

Gomes, L., Rocha, D.M., César, A., Pires, B., Carmelo, A.C., Oswaldo, J., Filho, D.A., 2014. Geophysical characterization of the Azimuth 125 ◦ lineament with aeromagnetic data : Contributions to the geology of central Brazil. Precambrian Res. 249, 273–287. https://doi.org/10.1016/j.precamres.2014.05.005

GWB, 2018. Community Groundwater Supply Development in Acholiland , Northern Uganda. Calgary, AB.

Hall, J., 1986. Geophysical Lineaments and Deep Continental Structure. Philos. Trans. R. Soc. London 317, 33–44.

Hall, M., Diggens, J., 2011. The East African Rift System - A view from space. Geo Expro Mag. Vol 8., 96.

Hengl, T., Jesus, J.M. De, Heuvelink, G.B.M., Ruiperez, M., Kilibarda, M., Blagoti, A., Shangguan, W., Wright, M.N., Geng, X., Bauer-marschallinger, B., Guevara, M.A., Vargas, R., Macmillan, R.A., Batjes, N.H., Leenaars, J.G.B., Ribeiro, E., Wheeler, I., Mantel, S., Kempen, B., 2017. SoilGrids250m : Global gridded soil information based on machine learning. PLoS One 1–41. https://doi.org/10.1371/journal.pone.0169748

Henrique, P., Santos, D., Miranda, S., Ornaghi, D., Anna, S., Henrique, C., Oliveira, D., Duarte, H., 2019. The analytic hierarchy process supporting decision making for sustainable development : An overview of applications. J. Clean. Prod. 212, 119–138. https://doi.org/10.1016/j.jclepro.2018.11.270

Katumwehe, A.B., Abdelsalam, M.G., Atekwana, E.A., Laó-Dávila, D.A., 2016. Extent, kinematics and tectonic origin of the Precambrian Aswa Shear Zone in eastern Africa. Gondwana Res. 34, 241–253. https://doi.org/10.1016/j.gr.2015.03.007

Kim, Y., van Zyl, J.J., 2009. A Time-Series Approach to Estimate Soil Moisture Using Polarimetric Radar Data. Geosci. Remote Sensing, IEEE Trans. 47, 2519–2527. https://doi.org/10.1109/TGRS.2009.2014944

Kupidura, P., 2016. Comparison of filters dedicated to speckle suppression in SAR Images. Int. Arch. Photogramm. Remote Sens. Spat. Inf. Sci. XLI, 12–19. https://doi.org/10.5194/isprsarchives-XLI-B7-269-2016

Lasaponara, R., Masini, N., 2013. Satellite synthetic aperture radar in archaeology and cultural landscape: An overview. Archaeol. Prospect. 20, 71–78. https://doi.org/10.1002/arp.1452

Laurencelle, J., Logan, T., Gens, R., 2015. ASF Radiometrically Terrain Corrected ALOS PALSAR products Product guide (No. 1.2). ASF Engineering.

Lee, J., Fellow, L., Ainsworth, T.L., Member, S., 2011. The Effect of Orientation Angle Compensation on Coherency Matrix and Polarimetric Target Decompositions. IEEE Trans. Geosci. Remote Sens. 49, 53–64. https://doi.org/10.1109/TGRS.2010.2048333

Lee, S., Kim, Y.S., Oh, H.J., 2012. Application of a weights-of-evidence method and GIS to regional groundwater productivity potential mapping. J. Environ. Manage. 96, 91–105. https://doi.org/10.1016/j.jenvman.2011.09.016

Li, X., 2001. Tutorial Ellipsoid , geoid , gravity , geodesy , and geophysics 66, 1660–1668.

Luo, Q., Hu, M., Zhao, Z., Li, J., Zeng, Z., 2020. Design and experiments of X-type artificial control targets for a UAV-LiDAR system. Int. J. Remote Sens. 41, 3307–3321. https://doi.org/10.1080/01431161.2019.1701210

Macdonald, A.M., Davies, J., 2000a. A brief review of groundwater for rural water supply in sub-Saharan. Br. Geol. Surv. Tech. Rep. WC/00/33 13. https://doi.org/WC/00/33

Macdonald, A.M., Davies, J., 2000b. A brief review of groundwater for rural water supply in sub-Saharan Africa. Br. Geol. Surv. Tech. Rep. WC/00/33 13. https://doi.org/WC/00/33

Mahyoub, S., Fadil, A., Mansour, E.M., Rhinane, H., Al-nahmi, F., 2019. Fusing of optical and synthetic aperture radar (SAR) remote sensing data: a systematic literature review (SLR). Int. Arch. Photogramm. Remote Sens. Spat. Inf. Sci. XLII, 10–11.

Meyer, F.J., Nicoll, J.B., 2008. Prediction , Detection , and Correction of Faraday Rotation in Full-Polarimetric L-Band SAR Data. IEEE Trans. Geosci. Remote Sens. 46, 3076–3086. https://doi.org/10.1109/TGRS.2008.2003002

Milas, A.S., Warner, T.A., Younan, N.H., Balenovic, I., Larson, M.D., Simic, A., Warner, T.A., Younan, N.H., Balenovic, I., 2019. Preface for the Special Issue of IJRS Drones section in conjunction with the 6th UAS4Enviro conference Preface for the Special Issue of IJRS Drones section in. Int. J. Remote Sens. 40, 9065–9069. https://doi.org/10.1080/01431161.2019.1658409

Mutiti, S., Levy, J., Mutiti, C., Gaturu, N.S., 2010. Assessing ground water development potential using Landsat imagery. Ground Water 48, 295–305. https://doi.org/10.1111/j.1745-6584.2008.00524.x

Noureldin, A., Karamat, T.B., Georgy, J., 2013. Fundamentals of inertial navigation, satellite-based positioning and their integration, Fundamentals of Inertial Navigation, Satellite-Based Positioning and their Integration. https://doi.org/10.1007/978-3-642-30466-8

Olierook, H.K.H., Scalzo, R., Kohn, D., Chandra, R., Farahbakhsh, E., Houseman, G., Clark, C., Reddy, S.M., Müller, R.D., 2019. Bayesian geological and geophysical data fusion for the construction and uncertainty quantification of 3D geological models. Solid Earth Discuss. 1–34.

Oyawale, A.A., Adeoti, F.O., Ajayi, T.R., Omitogun, A.A., 2020. Applications of remote sensing and geographic information system (GIS) in regional lineament mapping and structural analysis in Ikare Area , Southwestern Nigeria. J. Geol. Min. Res. 12, 13–24. https://doi.org/10.5897/JGMR2019.0310

Pan, Y., Ren, C., Liang, Y., Zhang, Z., Shi, Y., 2020. Inversion of surface vegetation water content based on GNSS - IR and MODIS data fusion. Satell. Navig. 1–15. https://doi.org/10.1186/s43020-020-00021-z

Pavez, A., Remy, D., Bonvalot, S., Diament, M., Gabalda, G., Froger, J., 2006. Insight into ground deformations at Lascar volcano (Chile) from SAR interferometry , photogrammetry and GPS data : Implications on volcano dynamics and future space monitoring. Remote Sens. Environ. 100, 307–320. https://doi.org/10.1016/j.rse.2005.10.013

Pavlic, G., Singhroy, V., Duk-Rodkin, A., Alasset, P., 2008. Satellite data fusion techniques for terrain and surficial geological mapping, in: IEEE IGARSS. pp. 314–317. https://doi.org/10.1109/IGARSS.2008.4779346

Rahmati, O., Haghizadeh, A., Stefanidis, S., 2016. Assessing the Accuracy of GIS-Based Analytical Hierarchy Process for Watershed Prioritization ; Gorganrood River 1131–1150. https://doi.org/10.1007/s11269-015-1215-4

Rahnama, M., Gloaguen, R., 2014. TecLines: A MATLAB-Based Toolbox for Tectonic Lineament Analysis from Satellite Images and DEMs, Part 1: Line Segment Detection and Extraction. Remote Sens. 5938–5958. https://doi.org/10.3390/rs6075938

Republic of Uganda, 2019. Airborne Geophysical Digital Data Dissemination Policy.

Reynolds, J.M., 1997. An Introduction to Applied and Environmental Geophysics. John Wiley & Sons Ltd.

Robins, N.S., Davies, J., Farr, J.L., Calow, R.C., 2006. The changing role of hydrogeology in semi-arid southern and eastern Africa. Hydrogeol. J. 14, 1483–1492. https://doi.org/10.1007/s10040-006-0056-x

Rott, H., 1984. The Analysis of Backscattering Properties from SAR Data of Mountain Regions. IEEE J. Ocean. Eng. 9, 347–355. https://doi.org/10.1109/JOE.1984.1145655

Russo, T.A., Fisher, A.T., Lockwood, B.S., 2015. Assessment of Managed Aquifer Recharge Site Suitability Using a GIS and Modeling 53, 389–400. https://doi.org/10.1111/gwat.12213

Saalmann, K., Mänttäri, I., Nyakecho, C., Isabirye, E., 2016. Age, tectonic evolution and origin of the Aswa Shear Zone in Uganda: Activation of an oblique ramp during convergence in the East African Orogen. J. African Earth Sci. 117, 303–330. https://doi.org/10.1016/j.jafrearsci.2016.02.002

Saaty, T.L., 1994. How To Make A Decision : The Analytic Hierarchy Process 75–105.

Salem, A., Fairhead, J., Ravat, D., Smith, R., 2007. Tilt-depth method : A simple depth estimation method using first-order magnetic derivatives. Lead. Edge 3–6.

Sandoval, J.A., Tiburan, C.L., 2019. Identification of potential artificial groundwater recharge sites in Mount Makiling Forest Reserve , Philippines using GIS and Analytical Hierarchy Process. Appl. Geogr. 105, 73–85. https://doi.org/10.1016/j.apgeog.2019.01.010

Senanayake, I.P., Dissanayake, D.M.D.O.K., Mayadunna, B.B., Weerasekera, W.L., 2016. An approach to delineate groundwater recharge potential sites in Ambalantota, Sri Lanka using GIS techniques. Geosci. Front. 7, 115–124. https://doi.org/10.1016/j.gsf.2015.03.002

Sener, E., Davraz, A., 2013. Assessment of groundwater vulnerability based on a modified DRASTIC model , GIS and an analytic hierarchy process (AHP) method: the case of Egirdir Lake basin (Isparta , Turkey). Hydrogeol. J. 701–714. https://doi.org/10.1007/s10040-012-0947-y

Shahdoosti, H.R., Ghassemian, H., 2016. Combining the spectral PCA and spatial PCA fusion methods by an optimal filter. Inf. Fusion 27, 150–160. https://doi.org/10.1016/j.inffus.2015.06.006

Sloots, R., 2010. Ministry of Water and Environment Assessment of Groundwater Investigations and Borehole Drilling Capacity in Uganda.

Small, D., 2011. Flattening Gamma : Radiometric Terrain Correction for SAR Imagery. IEEE Trans. Geosci. Remote Sens. 49, 3081–3093.

Srivastava, H.S., Patel, P., Navalgund, R.R., 2006. How far SAR has fulfilled its expectation for soil moisture retrieval. Microw. Remote Sens. Atmos. Environ. 6410, 641001. https://doi.org/10.1117/12.693946

Strozzi, T., Delaloye, R., Kääb, A., Ambrosi, C., Perruchoud, E., 2010. Combined observations of rock mass movements using satellite SAR interferometry , differential GPS , airborne digital photogrammetry , and airborne photography interpretation. J. Geophys. Res. 115, 1–12. https://doi.org/10.1029/2009JF001311

Tagnon, B.O., 2016. Statistical and Geostatistical Analysis of Lineaments Network Mapped in The Precambrian Basement : Case of Divo-Oume Region (Southern Cote d ' Ivoire). Eur. Sci. J. 12, 299–318. https://doi.org/10.19044/esj.2016.v12n33p299

Thannoun, R.G., 2013. Automatic Extraction and Geospatial Analysis of Lineaments and their Tectonic Significance in some areas of Northern Iraq using Remote Sensing Techniques and GIS. Int. J. Enhanc. Reseaarch Sci. Technol. Eng. 2, 1–11.

Tsiko, R.G., Haile, T.S., 2011. Integrating Geographical Information Systems, Fuzzy Logic and Analytical Hierarchy Process in Modelling Optimum Sites for Locating Water Reservoirs. A Case Study of the Debub District in Eritrea. Water 254–290. https://doi.org/10.3390/w3010254

Turkar, V., Bombay, I.I.T., 2011. Applying Coherent and Incoherent Target Decomposition Techniques to Polarimetric SAR Data 23–29.

UNDP, WHO, WFP, Uganda, R. of, Project, N.U.E.R., 2013. Rays of Hope in Lango Sub-Region, Northern Uganda.

Van Zyl, Jakob; Kim, Y., 2011. Synthetic Aperture Radar Polarimetry. John Wiley & Sons, Inc.

Vasuki, Y., Holden, E., Kovesi, P., Micklethwaite, S., 2014. Semi-automatic mapping of geological structures using UAV-based photogrammetric data : An image analysis approach. Comput. Geosci. 69, 22–32. https://doi.org/10.1016/j.cageo.2014.04.012

Vijayaraj, V., Younan, N.H., Hara, C.G.O., 2006. Concepts of Image Fusion in Remote Sensing Applications, in: 2006 IEEE International Symposium on Geoscience and Remote Sensing. pp. 3781–3784. https://doi.org/10.1109/IGARSS.2006.973

Wald, L., Ranchin, T., Mangolini, M., Wald, L., Ranchin, T., Mangolini, M., 2009. Fusion of satellite images of different spatial resolutions : Assessing the quality of resulting images To cite this version : HAL Id : hal-00365304.

Walker, P.J.P., 2013. Basis of an Australian Radar Soil Moisture Algorithm Theoretical Baseline Document (ATBD).

Wang, Xiaofei, Wang, Xiaoyi, 2020. Spatiotemporal Fusion of Remote Sensing Image Based on Deep Learning. J. Sensors 2020.

Xu, G., Xu, Y., 2016. GPS: Theory, algorithms and applications, third edition. GPS Theory, Algorithms Appl. Third Ed. 1–489. https://doi.org/10.1007/978-3-662-50367-6

Xu, W., Lan, Y., Li, Y., Luo, Y., He, Z., 2019. Classification method of cultivated land based on UAV visible light remote sensing. Int. J. Agric. Biol. Eng. 12, 103–109. https://doi.org/10.25165/j.ijabe.20191203.4754

Yeomans, C.M., Middleton, M., Shail, R.K., Grebby, S., Lusty, P.A.J., 2019. Integrated Object-Based Image Analysis for semi-automated geological lineament detection in southwest England. Comput. Geosci. 123, 137–148. https://doi.org/10.1016/j.cageo.2018.11.005

Zeng, T., Yin, W., Ding, Z., Long, T., 2016. Motion and Doppler Characteristics Analysis Based on Circular Motion Model in Geosynchronous SAR. IEEE J. Sel. Top. Appl. Earth Obs. Remote Sens. 9, 1132–1142. https://doi.org/10.1109/JSTARS.2015.2429915

Zhang, X., Tang, X., Gao, X., Zhao, H., 2018. Multitemporal Soil Moisture Retrieval over Bare Agricultural Areas by Means of Alpha Model with Multisensor SAR Data. Adv. Meteorol. 2018, 17.

Zhu, X.X., Member, S., Montazeri, S., Gisinger, C., Hanssen, R.F., Member, S., Bamler, R., 2016. Geodetic SAR Tomography. IEEE Trans. Geosci. Remote Sens. 54, 18–35. https://doi.org/10.1109/TGRS.2015.2448686

Zyl, J.J. Van, Arii, M., Kim, Y., Member, S., 2011. Model-Based Decomposition of Polarimetric SAR Covariance Matrices Constrained for Nonnegative Eigenvalues. IEEE Trans. Geosci. Remote Sens. 49, 3452–3459. https://doi.org/10.1109/TGRS.2011.2128325

VITA

Rachel Jones graduated with a Bachelor of Science in Geological Engineering from University of Missouri – Rolla in 2007. She attended the Humanitarian Academy at Harvard University where she received certificates in Humanitarian Response, Building a Better Response, and Unmanned Aerial Vehicle (UAV) and Remote Sensing (RS) for Humanitarian Missions in 2018. Her certificates earned in 2019 from the United Nations Department of Safety and Security (UNDSS) include Basic and Advanced Security in the Field, and CyberSecurity: Information Security Awareness. She received the 2020 United States Geospatial Intelligence Foundation (USGIF) Doctoral Scholarship for her doctoral research. Rachel received her Doctor of Philosophy in Geological Engineering from Missouri University of Science and Technology in July 2021.

Rachel co-founded several charitable corporations including Pregnancy Resource Center of Rolla in 2005, Free Women's Center of Pulaski County in 2010, and Our Lady of Mount Calvary Mission and Medical Clinic in Ghana Africa in 2014. She worked in counter human and counter wildlife trafficking efforts both stateside and overseas and founded the Emmaus Project for domestic counter human trafficking.

Rachel was a Visiting Scientist in the Oak Ridge Institute for Science and Education (ORISE) program at National Geospatial Intelligence Agency (NGA) where she was awaiting permanent placement in Geomatics.